E-ISSN 2980-3012

Physics and Astronomy Reports

VOLUME 2 • NUMBER 2 • DECEMBER 2024

İSTANBUL UNIVERSITY PRESS

Physics and Astronomy Reports
DECEMBER 2024,
VOLUME 2, NUMBER 2

Indexing and Abstracting

NASA/ADS
Gale Cengage

OWNER
Prof. Dr. Tansel AK
İstanbul University, Faculty of Science, İstanbul, Türkiye

RESPONSIBLE MANAGER
Prof. Dr. Elif AKALIN
İstanbul University, Faculty of Science,
Department of Physics, İstanbul, Türkiye

CORRESPONDENCE ADDRESS
İstanbul University Faculty of Science
PK 34134 Vezneciler, Fatih, İstanbul, Türkiye
Phone : +90 (212) 455 57 00
Fax : +90 (212) 512 21 40
E-mail: par@istanbul.edu.tr
https://iupress.istanbul.edu.tr/en/journal/par/home
https://dergipark.org.tr/en/pub/par

PUBLISHER
İstanbul University Press
İstanbul University Central Campus,
34452 Beyazit, Fatih, İstanbul, Türkiye
Phone: +90 (212) 440 00 00

The publication language of the journal is English.

This is a scholarly, international, peer-reviewed and open-access journal published biannually in June and December.

Publication Type: Periodical

Physics and Astronomy Reports
DECEMBER 2024,
VOLUME 2, NUMBER 2

Physics and Astronomy Reports
DECEMBER 2024,
VOLUME 2, NUMBER 2

İSTANBUL UNIVERSITY PRESS

CONTENTS

RESEARCH ARTICLES

İSTANBUL UNIVERSITY PRESS

Physics and Astronomy Reports
PAR 2024, 2 (2), 58–64
DOI: 10.26650/PAR.2024.00006

RESEARCH ARTICLE

Transformation Relations for UBV Photometric System of 1m Telescope at the TÜBİTAK National Observatory

T. Ak[1*], R. Canbay[2], and T. Yontan [1]

[1]İstanbul University, Faculty of Science, Department of Astronomy and Space Sciences, 34119, İstanbul, Türkiye
[2]İstanbul University, Institute of Graduate Studies in Science, Programme of Astronomy and Space Sciences, 34116, İstanbul, Türkiye

ABSTRACT

UBV CCD observations of standard stars selected from Landolt (2009, 2013) were performed using the 1-meter telescope (T100) of the TÜBİTAK National Observatory equipped with a CCD camera and Bessell *UBV* filters. Observations were conducted over an extended period, spanning from 2012 to 2024, covering a total of 50 photometric nights. Photometric measurements were used to find the standard transformation relations of the T100 photometric system. The atmospheric extinction coefficients, zero points and transformation coefficients of each night were determined. It was observed that the primary extinction coefficients decreased until the year 2019 and increased after that year. Strong seasonal variations in the extinction coefficients were not evident. Small differences in seasonal median values of them were used to attempt to find the atmospheric extinction sources. We found calculated minus catalogue values for each standard star, $\Delta(U\text{-}B)$, $\Delta(B\text{-}V)$, and ΔV. The means and standard deviations of these differences were estimated to be 1.4±76, 1.9±18, and 0.0±36 mmag, respectively. We found that our data well matched Landolt's standards for V and $B\text{-}V$, i.e. there are no systematic differences. However, there are systematic differences for $U\text{-}B$ between the two photometric systems, which is probably originated from the quantum efficiency differences of the detectors used in the photometric systems, although the median differences are relatively small ($|\Delta(U\text{-}B)|$<50 mmag) for stars with -0.5<$(U\text{-}B)$<1.6 and 0.2<$(B\text{-}V)$<1.8. We conclude that the transformation relations found in this study can be used for standardised photometry with the T100 photometric system.

Keywords: Techniques: CCD photometry; stars: imaging; standard star

1. INTRODUCTION

The instrumental magnitude of a celestial object measured during an astronomical observation depends not only on the object's flux and atmospheric extinction but also on the spectral response and transmission properties of the telescope-filter-detector combination. In some cases, instrumental magnitudes must be transformed into a standard photometric system by observing standard stars. The 'Johnson-Kron-Cousins' $UBVR_CI_C$ system is the most widely used broad-band photometric system. The $UBV(RI)$ photometric system was designed by Johnson & Morgan (1953) taking Yerkes Atlas system (MK) of spectral classification as standard. In this photometric system, the colour indices of the bright star Vega with spectral type A0 was defined as the zero point of all colour indices. Due to advancements in detector technologies, accurate photometry of faint stars became possible in the 1970s and 1990s, and the Kron-Cousins R_CI_C filters were replaced with RI filters of Johnson and Morgan.

There are two main sets of standard stars used for broad-mations are generally linear as combined spectral responses of filter and detector are very similar (see, Sung & Bessell 2000).

Detailed information of photometric observing systems, including atmospheric extinction coefficients and transformation relations, is crucial for standardized photometry. In a series of *UBV* photometric observations of open stellar clusters between the years 2012 and 2024, we have also observed Landolt's selected standard star fields for each observing night with Bessell *UBV* filters attached to an SI 1100S CCD camera and 1-meter telescope of the TÜBİTAK National Observatory. Atmospheric extinction coefficients and transformation equations to standard photometric systems were calculated for each photometric night. Although the observations have not been done specifically for monitoring the extinction and transformation coefficients of this photometric system, we could obtain them as a side-product of our observations. In this study, we investigate the variation of atmospheric extinction coefficients for the last 12 years and introduce a reliable set of *UBV* transformation relations for the photometric observing system of the 1-meter telescope (T100) at the TÜBİTAK National Observatory.

Corresponding Author: T. Ak **E-mail:** tanselak@istanbul.edu.tr
Submitted: 25.10.2024 • **Accepted:** 04.12.2024

2. OBSERVATIONS AND DATA REDUCTION

All the observations have been performed with the 1-meter telescope (T100) of TÜBİTAK National Observatory. The T100 telescope has a Ritchey-Chretien optical system with an $f/10$ focal ratio which provides a wide field of view using appropriate 3-element field lenses[1]. T100 is equipped with an SI 1100 CCD camera and Bessell UBV filters. Specifications of the camera are given in Table 1[1]. The camera has a Fairchild 486 Back Illuminated and UV-enhanced chip, which covers a field of view of $21'.5 \times 21'.5$. Quantum efficiency (QE) of the chip is shown in Figure 1[2]. QE of the chip across the U passband is very good, i.e. its QE is ~65% at λ=300 nm and ~92% at λ=400 nm. Transmittance curves of the Bessell UBV filters are presented in Figure 2[3]. Note that the B filter has a very weak visual leak centered at ~560.5 nm with a maximum transmittance of ~1.6%. Since the transmittance of Bessell U filter starts at ~315 nm and peaks at ~370 nm, QE curve of the chip covers this filter with acceptable sensitivity. QE of the chip is also high for the Bessell B and V filters. It should also be noted that all the observations were done with the 2×2 binning mode of the camera to save the data downloading time and observe fainter stars with a high S/N ratio.

Stellar fields including standard stars selected from Landolt (2009, 2013) have been observed with Bessell UBV filters during 50 nights from 18 July 2012 to 29 September 2024. The fields with red and blue standards were preferred to find the colour dependence of atmospheric extinction. Each field was observed at least three times using Bessell UBV filters at the same airmass in order to estimate averages of stellar magnitudes. Image Reduction and Analysis Facility (IRAF[4]) routines were utilized for pre-reduction processes, bias subtraction and flat fielding the images. We did not perform dark frame subtraction since the camera's dark level is negligible. The instrumental magnitudes of the standard stars were measured utilizing IRAF software packages with aperture photometry.

Table 1. Specifications of the SI 1100S camera attached to the T100 telescope of TÜBİTAK National Observatory.

Camera	Spectral Instruments 1100S Cryo, UV, AR, BI
Chip	Fairchild 486 Back Illuminated
Read-out channels	4 channels
Pixel Number	4096 × 4037
Pixel Size	15 × 15 micron
Chip Size	61.44 × 61.44 mm
Gain	0.57 e^-/ADU (@ 100 kHz)
Noise	4.11 e^- (@ 100 kHz)
Bias level	~500 ADU
Dark Current	0.0001 e^-/pixel/sec
Well Depth	142900 e^-
Dynamic Range	16 bit
Chip Size	61.44 × 61.44 mm
Shutter	Bonn 80, Slit Type
Exposure Range	1 msec to 3600 sec
Cooling Method	Cryo-tiger
Operating Temp.	-100 °C
PC Interface	Gigabit F/O kart (PCI)
Transfer Time	48 sec (1×1 binning), 13 sec (2×2 binning)
Pixel Scale	$0''.31$ pixel^{-1}
Field of View	$21'.5 \times 21'.5$
Software	Maxim DL 5.12
Filter Wheel	2 wheels with 8 holes (76×76 mm each)
Filters	Asahi Conventional Bessell $UBVR_CI_C$

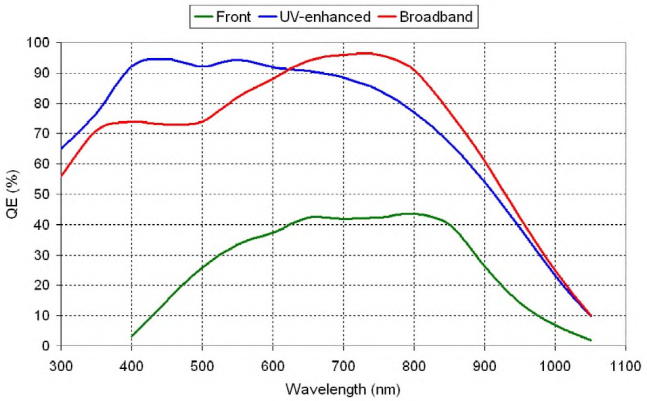

Figure 1. Quantum efficiency (QE) of the Fairchild 486 Back Illuminated chip attached to SI 1100S CCD camera. The UV-enhanced version (solid blue line) of the chip is used in our observations.

3. RESULTS

3.1. Extinction coefficients and zero points

Atmospheric extinction is caused primarily by Rayleigh scattering and absorption from gas molecules, dust particles and aerosols in the atmosphere. The amount of extinction depends primarily on airmass but also varies with wavelength and color. These extinction dependencies are corrected by using a primary (or first) extinction coefficient, which depends on airmass, and a secondary extinction coefficient which depends also on colour. In addition, transformation coefficients are needed to transform the extra-atmospheric magnitudes to the standard photometric system. For V, $B-V$, and $U-B$, we derived coefficients of the form were given by Janes et al. (2013)

$$v = V + \alpha_{bv}(B-V) + k_v X + C_{bv}$$
$$b = V + \alpha_b(B-V) + k_b X + k_b^{'} X(B-V) + C_b$$
$$u = V + (B-V) + \alpha_{ub}(U-B) + k_u X + k_u^{'} X(U-B) + C_{ub}$$

where U, B, and V are the magnitudes in the standard photometric system. Parameters u, b, and v denote the instrumental magnitudes. X is the airmass. Parameters k and $k^{'}$ represent primary and secondary extinction coefficients. α and C are

[1] https://tug.tubitak.gov.tr/en
[2] http://linmax.sao.arizona.edu/FLWO/48/CCD486DataSheetRevB.pdf
[3] https://www.asahi-spectra.com/
[4] IRAF is distributed by the National Optical Astronomy Observatories

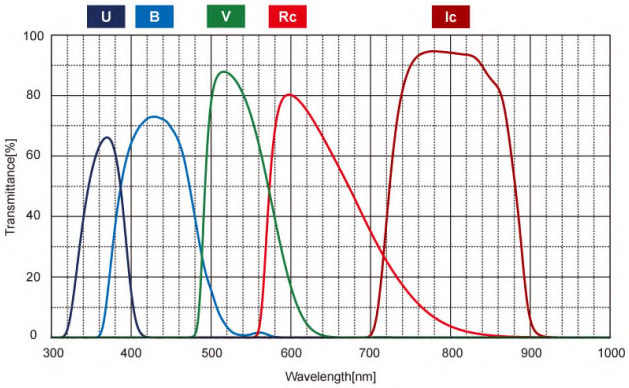

Figure 2. Transmittance curves of the conventional Bessell *UBV* filters of Asahi.

transformation coefficients to the standard photometric system and zero points, respectively. Multiple linear regression fits were applied to the transformation equations given above to estimate the photometric extinction and transformation coefficients with zero points for the observing nights. We determined atmospheric extinction and transformation coefficients under photometric conditions. Since we observed a considerable number of standard stars at different airmasses, we could obtain precise coefficients. The number of usable data points, the atmospheric extinction coefficients and zero points are given in Table 2.

The extinction coefficients in Table 2 span a 12-year observing period, although no observations were conducted in 2015 and 2017. The extinction coefficients in Table 2 cover a 12-year observing time, although no observations were conducted in 2015 and 2017. Median values of k_u, k_b, and k_v were calculated as 0.481 ± 0.097, 0.303 ± 0.086, and 0.174 ± 0.050, respectively. Median secondary extinction coefficients $k_u^{'}$ and $k_b^{'}$ were found to be -0.048 ± 0.164 and -0.034 ± 0.072. Error-values are standard deviations of the coefficients. Primary and secondary extinction coefficients can vary during the years depending on the atmospheric conditions of the observatory. Figure 3 exhibits such a slight variation of k_u, k_b, and k_v, where the increase after the year 2019 is prominent for V and B bands. These increases in extinction coefficients suggest that the photometric conditions at the observatory have gradually deteriorated since 2019. We could not detect considerable systematic increase or decrease in secondary extinction coefficients $k_u^{'}$ and $k_b^{'}$.

Seasonal variations in primary extinction coefficients can help select appropriate observing nights for research projects. Unfortunately, it is not possible to find reliable median values of extinction coefficients obtained between December and February, since we have standard star observations for only two nights in this interval during the observing period of 12 years. Mean values of extinction coefficients of these two winter nights are k_u=0.432±0.031, k_b=0.255±0.031, and k_v=0.149±0.009, where errors are mean values of individual errors. Similarly, we could observe standard stars only one night between March and May during 12 years of observing period. The remaining observations were performed summer (June-August) and autumn (September-November) seasons. Median values of extinction coefficients are k_u=0.477±0.089, k_b=0.322±0.077, and k_v=0.191±0.051 for summer season, while k_u=0.502±0.113, k_b=0.279±0.098, and k_v=0.157±0.047 for autumn season. There appears to be no significant seasonal difference in extinction coefficients between summer and autumn, as their median values are very similar within the margins of error. Based on the seasonal extinction coefficients and the number of usable nights, it is evident that winter and spring are not favorable seasons for photometric observations at the TÜBİTAK National Observatory.

It is known that instrumental parameters and atmospheric conditions affect the photometric zero point. The value of the photometric zero point depends on the size and condition (primarily mirror reflectivity) of the telescope and the quantum efficiency of the detector. Atmospheric conditions, such as water vapour content and height of the ozone layer, also affect the photometric zero points. The photometric zero points C_b, C_{bv} and C_{ub} measured during our observations are listed in Table 2. Variations of zero points are shown in Figure 4. As can be seen in Figure 4, variation of the zero points with time clearly exhibits the condition of the telescopic reflectivity. Beginning with the year 2012, reflectivity decreases (zero points become fainter) with time. Cleaning of the main mirror in August 2022 can be seen in Figure 4 as a sudden brightening of zero points.

3.2. Transformation coefficients

Transformation coefficients found from the standard star observations made during 50 nights between the years 2012 and 2024 are given in Table 3. Median values of the transformation coefficients are α_b=0.958 ± 0.100, α_{bv}=0.070 ± 0.013, and α_{ub}=0.886 ± 0.228, where errors are standard deviations of the individual values. We calculated possible maximum values by adding standard deviations to the median transformation coefficients. Using these maximum values, the resulting magnitudes differ by at most 25-30 mmag for a red star ($B - V = 1.9$ mag) compared to those calculated with median coefficients, assuming extinction coefficients and zero points remain constant.

3.3. Sources of extinction

Small seasonal differences in median extinction coefficients may result from extinction sources in the atmosphere. Atmospheric extinction is mainly a result of scattered light from molecules and small particles. The scattering efficiency depends on wavelength. The relation between the atmospheric extinction coefficients and wavelength can be expressed as $k_\lambda = \beta/\lambda^n$, where k_λ, β and λ are the extinction coefficient, an appropriate constant and the mean wavelength of filter (Golay 1974). If extinction is due to the Rayleigh scattering, then n=4.

Table 2. The atmospheric extinction coefficients and zero points obtained each observing night. Numbers in parentheses denote the number of usable data points. Median values are given in the last line, where errors are standard deviations of the individual values.

Date	k_u	k_b	k_v	$k_{u'}$	$k_{b'}$	C_b	C_{bv}	C_{ub}
2012.07.18	0.597±0.032(38)	0.392±0.022(52)	0.247±0.005(52)	-0.058±0.032	-0.030±0.019	0.771±0.050	0.799±0.010	3.111±0.054
2012.07.19	0.472±0.031(82)	0.326±0.024(85)	0.189±0.024(85)	-0.019±0.032	-0.057±0.025	0.745±0.036	0.799±0.017	3.143±0.046
2012.07.20	0.559±0.033(39)	0.392±0.011(30)	0.235±0.002(41)	-0.002±0.035	-0.037±0.011	0.786±0.017	0.838±0.005	3.190±0.054
2012.08.16	0.677±0.030(63)	0.525±0.050(58)	0.242±0.007(73)	-0.023±0.067	-0.246±0.079	0.786±0.017	0.779±0.016	3.041±0.043
2012.08.17	0.365±0.025(50)	0.270±0.041(57)	0.166±0.004(66)	+0.216±0.041	+0.002±0.051	0.890±0.054	0.879±0.015	3.453±0.034
2013.08.08	0.397±0.014(51)	0.240±0.014(72)	0.118±0.003(58)	-0.007±0.018	-0.041±0.015	0.481±0.021	0.538±0.005	2.893±0.020
2013.08.09	0.347±0.016(99)	0.206±0.014(136)	0.098±0.005(124)	-0.066±0.018	-0.032±0.014	0.552±0.022	0.591±0.009	2.991±0.024
2013.08.10	0.439±0.025(79)	0.328±0.042(109)	0.149±0.006(116)	-0.126±0.024	-0.097±0.038	0.431±0.060	0.559±0.015	2.908±0.037
2014.08.27	0.585±0.080(41)	0.363±0.076(75)	0.273±0.010(80)	-0.017±0.149	+0.002±0.097	1.124±0.109	1.102±0.032	3.492±0.111
2014.09.24	0.330±0.071(86)	0.263±0.070(90)	0.130±0.010(102)	-0.038±0.136	-0.065±0.084	0.944±0.104	1.006±0.030	3.487±0.102
2016.08.07	0.585±0.097(74)	0.345±0.053(74)	0.176±0.026(73)	-0.357±0.110	-0.096±0.056	1.238±0.078	1.346±0.035	3.542±0.133
2016.08.08	0.411±0.066(69)	0.243±0.064(73)	0.147±0.020(72)	-0.132±0.073	-0.017±0.068	1.342±0.091	1.366±0.030	3.778±0.096
2016.09.28	0.311±0.059(95)	0.214±0.064(96)	0.106±0.024(96)	-0.025±0.107	-0.054±0.069	1.340±0.090	1.381±0.034	3.824±0.082
2016.10.08	0.308±0.061(80)	0.151±0.041(81)	0.104±0.018(89)	+0.091±0.110	-0.003±0.048	1.444±0.063	1.391±0.027	3.807±0.089
2018.07.17	0.578±0.128(34)	0.351±0.090(41)	0.140±0.041(49)	-0.139±0.146	-0.108±0.084	1.944±0.128	2.083±0.060	4.216±0.186
2018.08.13	0.403±0.164(27)	0.198±0.085(31)	0.172±0.048(30)	+0.072±0.176	+0.061±0.090	1.490±0.126	1.449±0.074	3.778±0.241
2018.08.14	0.266±0.121(61)	0.195±0.056(55)	0.103±0.023(54)	+0.266±0.121	-0.034±0.056	1.476±0.081	1.540±0.036	3.960±0.170
2018.10.06	0.580±0.062(44)	0.262±0.047(41)	0.148±0.019(44)	-0.075±0.079	-0.030±0.057	1.391±0.071	1.475±0.031	3.538±0.097
2018.11.05	0.502±0.078(43)	0.232±0.046(46)	0.128±0.020(51)	-0.117±0.095	-0.037±0.050	1.488±0.070	1.550±0.031	3.724±0.121
2018.11.06	0.521±0.062(44)	0.226±0.046(45)	0.124±0.018(54)	-0.122±0.069	-0.021±0.052	1.512±0.068	1.570±0.028	3.718±0.093
2019.07.30	0.498±0.092(45)	0.293±0.079(50)	0.208±0.026(49)	-0.068±0.108	+0.026±0.082	1.799±0.116	1.782±0.037	4.162±0.116
2019.09.29	0.471±0.074(57)	0.298±0.061(72)	0.175±0.021(73)	+0.101±0.114	-0.004±0.072	1.783±0.091	1.834±0.032	4.176±0.110
2019.09.30	0.413±0.069(66)	0.285±0.061(78)	0.182±0.022(84)	+0.014±0.094	+0.029±0.069	1.850±0.092	1.853±0.033	4.338±0.102
2020.07.21	0.533±0.124(53)	0.307±0.052(52)	0.119±0.018(47)	-0.322±0.098	-0.106±0.040	2.089±0.079	2.202±0.025	4.421±0.182
2020.07.22	0.465±0.130(43)	0.431±0.081(45)	0.157±0.032(52)	-0.221±0.133	-0.237±0.085	1.904±0.124	2.151±0.048	4.470±0.191
2020.07.23	0.493±0.116(42)	0.272±0.058(45)	0.135±0.022(52)	-0.272±0.107	-0.097±0.050	2.130±0.088	2.174±0.033	4.491±0.169
2021.07.06	0.469±0.155(30)	0.273±0.085(30)	0.193±0.035(39)	-0.200±0.117	+0.003±0.070	2.754±0.111	2.640±0.044	5.178±0.198
2021.07.07	0.370±0.083(50)	0.319±0.064(56)	0.230±0.025(58)	-0.093±0.086	+0.053±0.063	2.733±0.111	2.624±0.033	5.318±0.108
2021.10.08	0.393±0.027(65)	0.218±0.018(82)	0.154±0.007(78)	+0.055±0.046	+0.009±0.063	2.796±0.029	2.673±0.012	5.216±0.042
2021.10.09	0.399±0.029(67)	0.244±0.020(76)	0.139±0.007(74)	-0.005±0.047	-0.004±0.022	2.757±0.031	2.699±0.012	5.195±0.044
2021.10.11	0.607±0.056(58)	0.395±0.064(70)	0.211±0.019(65)	+0.414±0.072	-0.080±0.083	2.684±0.079	2.710±0.025	5.090±0.071
2022.06.23	0.712±0.069(33)	0.560±0.093(34)	0.305±0.026(35)	-0.472±0.128	-0.204±0.124	2.948±0.123	3.014±0.032	5.428±0.092
2022.08.04	0.566±0.154(72)	0.354±0.048(67)	0.231±0.016(60)	+0.326±0.165	-0.058±0.051	3.123±0.064	3.018±0.023	5.500±0.709
2022.08.31	0.470±0.067(71)	0.263±0.045(70)	0.182±0.014(65)	-0.005±0.056	-0.025±0.044	0.558±0.058	0.605±0.019	2.916±0.084
2022.09.01	0.641±0.123(72)	0.486±0.124(74)	0.173±0.014(67)	-0.153±0.164	-0.263±0.151	0.342±0.160	0.622±0.018	2.757±0.159
2022.09.21	0.553±0.060(81)	0.330±0.045(85)	0.177±0.015(92)	-0.078±0.071	-0.050±0.048	0.561±0.058	0.658±0.020	2.924±0.020
2022.09.22	0.536±0.092(70)	0.318±0.052(79)	0.133±0.018(90)	-0.354±0.136	-0.125±0.061	0.579±0.068	0.710±0.023	2.942±0.116
2022.10.26	0.454±0.048(95)	0.343±0.039(102)	0.157±0.015(113)	-0.224±0.061	-0.110±0.038	0.576±0.048	0.718±0.018	3.035±0.059
2022.10.27	0.410±0.044(97)	0.255±0.030(99)	0.167±0.014(104)	-0.068±0.059	+0.005±0.034	0.670±0.040	0.695±0.018	3.101±0.057
2022.12.21	0.482±0.025(86)	0.235±0.024(79)	0.170±0.008(84)	-0.087±0.038	+0.002±0.028	0.780±0.033	0.729±0.013	3.121±0.036
2023.01.19	0.383±0.037(87)	0.275±0.039(85)	0.128±0.010(83)	-0.024±0.045	-0.068±0.043	0.729±0.050	0.779±0.013	3.266±0.048
2023.08.16	0.468±0.054(99)	0.413±0.043(95)	0.270±0.019(97)	+0.087±0.064	-0.100±0.050	0.853±0.054	0.950±0.023	3.442±0.067
2023.08.22	0.474±0.057(103)	0.312±0.046(111)	0.214±0.020(115)	+0.015±0.073	+0.019±0.050	0.970±0.056	0.970±0.024	3.414±0.070
2024.04.28	0.545±0.062(83)	0.445±0.069(84)	0.230±0.021(87)	-0.175±0.092	-0.156±0.082	1.049±0.088	1.187±0.027	3.582±0.076
2024.06.10	0.530±0.051(73)	0.334±0.054(80)	0.205±0.016(81)	-0.133±0.080	-0.024±0.060	1.218±0.072	1.263±0.022	3.608±0.065
2024.06.11	0.503±0.058(67)	0.418±0.062(64)	0.277±0.018(72)	+0.028±0.075	-0.025±0.067	1.178±0.082	1.232±0.024	3.707±0.073
2024.07.09	0.481±0.061(52)	0.290±0.060(68)	0.208±0.021(72)	-0.177±0.152	+0.026±0.078	1.409±0.082	1.351±0.028	3.867±0.078
2024.08.01	0.561±0.059(76)	0.385±0.063(74)	0.204±0.020(77)	-0.006±0.073	-0.081±0.064	1.310±0.077	1.368±0.025	3.767±0.076
2024.08.09	0.515±0.046(74)	0.330±0.049(80)	0.195±0.015(79)	+0.073±0.061	-0.034±0.052	1.428±0.064	1.407±0.021	3.897±0.062
2024.09.29	0.522±0.038(100)	0.279±0.043(99)	0.177±0.016(102)	+0.061±0.055	-0.017±0.052	0.926±0.055	0.976±0.023	3.236±0.050
Median	**0.481 ± 0.097**	**0.303 ± 0.086**	**0.174 ± 0.050**	**−0.048 ± 0.164**	**−0.034 ± 0.072**	**1.274 ± 0.751**	**1.384 ± 0.713**	**3.658 ± 0.755**

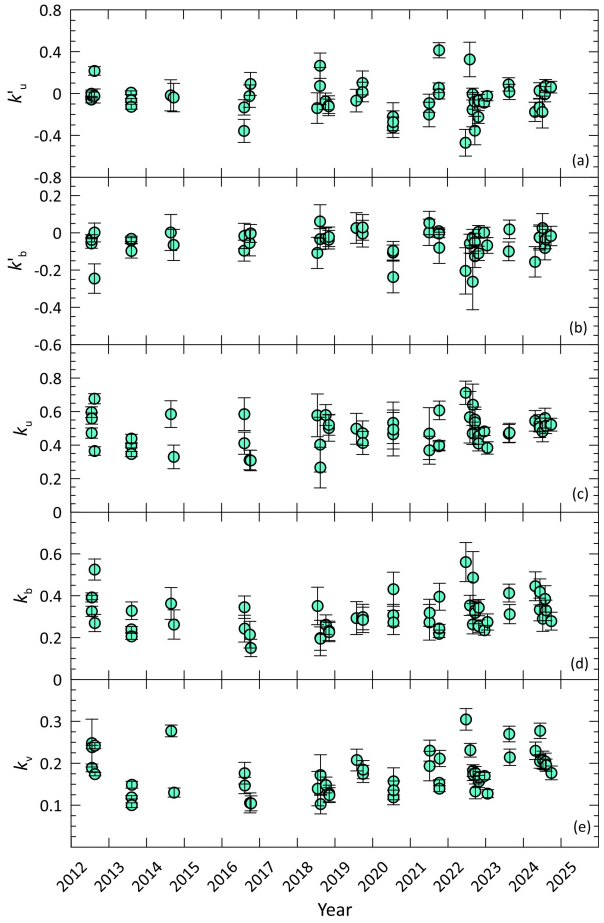

Figure 3. Variation of the primary and secondary extinction coefficients from 2012 to 2024.

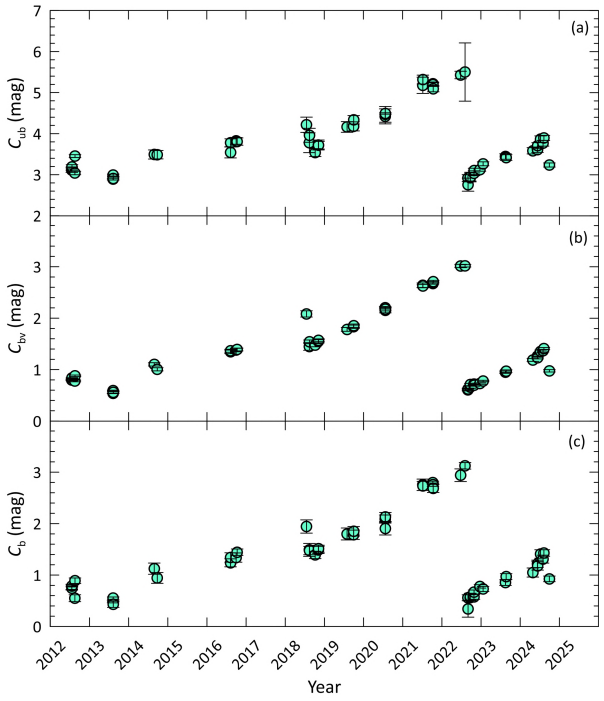

Figure 4. Variation of zero points from 2012 to 2024.

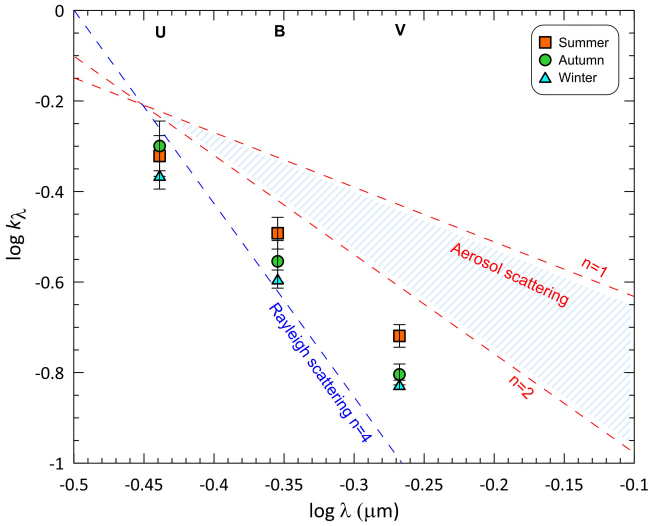

Figure 5. Variation of seasonal median values of extinction coefficients with wavelength. The shaded part represents the area affected by scattering due to aerosols and dust, while the line with n=4 represents the pure Rayleigh scattering.

When extinction is caused by aerosol and dust, then n is between 1 and 2. Seasonal averages are shown in Figure 5, where extinction coefficient variation with wavelength are also drawn for n=1, n=2, and n=4. Figure 5 shows that extinction during winter and autumn is almost entirely due to Rayleigh scattering. For the summer season, the source of extinction is mainly Rayleigh scattering although aerosol scattering has some effect.

3.4. Comparison with Landolt's catalogue

In order to find differences between the T100 and Landolt's photometric systems, we estimated differences of standard star' V magnitudes and $U-B$ and $B-V$ colour indices calculated from our transformation equations and the ones taken from Landolt's catalogues (Landolt 2009, 2013) for 34 nights between 2018 and 2024. Since there are 2188, 2421, and 2324 standard star observations for $U-B$, $B-V$, and V in these nights, respectively, we calculated median values of the differences for 0.1 mag intervals of $U-B$ and $B-V$ colour indices. The distribution of the median values with respect to the corresponding color indices is shown in Figure 6. Here Δ indicates the calculated value minus the catalogue value. Means and standard deviations of $\Delta(U-B)$, $\Delta(B-V)$, and ΔV were estimated to be 1.4±76, 1.9±18, and 0.0±36 mmag, respectively.

Figure 6 reveals that there are systematic differences between the T100's and Landolt's photometric systems for the U-band. Differences between the two systems in $U-B$ follow a sinusoidal-like curve against $U-B$ and $B-V$. However, the median differences are relatively small ($|\Delta(U-B)| \leq 0.05$) for stars with $-0.5 < U-B$ (mag) < 1.6 and $0.2 < B-V$ (mag) < 1.8, although it is considerably high for bluer and redder stars. This difference probably originates from the quantum efficiency

Table 3. The transformation coefficients calculated for each observing night. Median values are given in the last line, where errors are standard deviations of the individual values.

Date	α_b	α_{bv}	α_{ub}
2012.07.18	0.930±0.043	0.056±0.006	0.926±0.054
2012.07.19	0.992±0.038	0.077±0.011	0.861±0.050
2012.07.20	0.936±0.018	0.051±0.003	0.813±0.056
2012.08.16	1.253±0.105	0.084±0.011	0.836±0.093
2012.08.17	0.919±0.066	0.081±0.011	0.537±0.055
2013.08.08	0.972±0.024	0.070±0.003	0.840±0.027
2013.08.09	0.959±0.023	0.068±0.006	0.951±0.028
2013.08.10	1.045±0.055	0.069±0.010	1.038±0.037
2014.08.27	0.869±0.137	0.041±0.022	0.853±0.221
2014.09.24	1.004±0.124	0.086±0.020	0.929±0.196
2016.08.07	1.031±0.086	0.057±0.009	1.378±0.166
2016.08.08	0.920±0.095	0.056±0.007	0.613±0.105
2016.09.28	0.968±0.099	0.058±0.010	0.849±0.146
2016.10.08	0.900±0.073	0.068±0.008	0.754±0.158
2018.07.17	1.046±0.122	0.049±0.014	1.023±0.218
2018.08.13	0.805±0.135	0.045±0.017	0.730±0.266
2018.08.14	0.967±0.079	0.072±0.008	0.444±0.172
2018.10.06	0.978±0.084	0.101±0.011	0.988±0.120
2018.11.05	0.968±0.076	0.078±0.008	0.977±0.142
2018.11.06	0.932±0.077	0.073±0.007	0.986±0.102
2019.07.30	0.866±0.127	0.073±0.011	0.953±0.161
2019.09.29	0.900±0.107	0.062±0.008	0.684±0.166
2019.09.30	0.852±0.105	0.066±0.008	0.801±0.137
2020.07.21	1.057±0.064	0.071±0.009	1.304±0.157
2020.07.22	1.245±0.132	0.073±0.014	1.203±0.203
2020.07.23	1.044±0.081	0.066±0.010	1.221±0.161
2021.07.06	0.874±0.099	0.060±0.014	1.043±0.163
2021.07.07	0.810±0.090	0.063±0.013	0.882±0.115
2021.10.08	0.893±0.030	0.088±0.007	0.776±0.066
2021.10.09	0.920±0.035	0.078±0.006	0.891±0.071
2021.10.11	0.988±0.101	0.053±0.010	0.282±0.094
2022.06.23	1.165±0.163	0.082±0.013	1.426±0.166
2022.08.04	0.961±0.070	0.074±0.010	0.565±0.900
2022.08.31	0.956±0.059	0.065±0.008	0.842±0.074
2022.09.01	1.222±0.194	0.084±0.008	0.999±0.213
2022.09.21	0.968±0.063	0.074±0.008	0.945±0.096
2022.09.22	1.092±0.084	0.091±0.010	1.422±0.179
2022.10.26	1.049±0.049	0.071±0.007	1.169±0.084
2022.10.27	0.920±0.046	0.081±0.008	0.972±0.085
2022.12.21	0.888±0.039	0.079±0.008	1.010±0.058
2023.01.19	0.958±0.058	0.065±0.008	0.855±0.064
2023.08.16	1.054±0.067	0.050±0.023	0.715±0.082
2023.08.22	0.890±0.064	0.076±0.009	0.840±0.093
2024.04.28	1.075±0.106	0.046±0.013	1.038±0.116
2024.06.10	0.928±0.082	0.060±0.012	1.027±0.106
2024.06.11	0.926±0.093	0.067±0.012	0.797±0.096
2024.07.09	0.861±0.112	0.071±0.012	0.956±0.175
2024.08.01	1.001±0.081	0.071±0.010	0.835±0.094
2024.08.09	0.947±0.069	0.082±0.010	0.681±0.083
2024.09.29	0.926±0.068	0.062±0.011	0.738±0.073
Median	**0.958 ± 0.100**	**0.070 ± 0.013**	**0.886 ± 0.228**

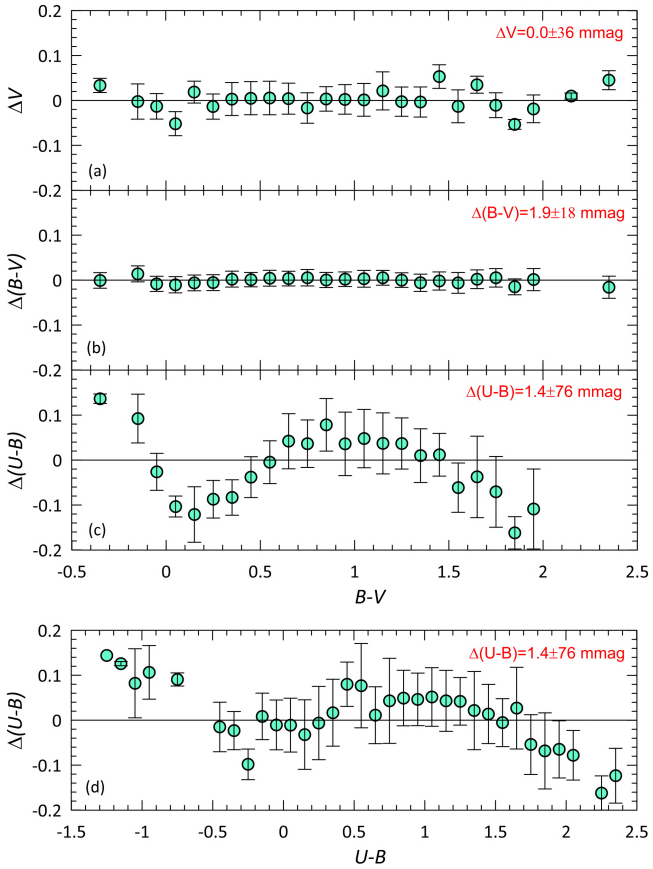

Figure 6. Median $\Delta(U-B)$, $\Delta(B-V)$, and ΔV values againts colour indices. Δ means calculated minus catalogue (Landolt 2009, 2013) value. Median values were calculated for 0.1 mag intervals of related colour index. Means and standard deviations of $\Delta(U-B)$, $\Delta(B-V)$, and ΔV are given in panels.

of detectors used in the two photometric systems. As for the differences of $\Delta(B-V)$ and ΔV, Figure 6 shows that transformation equations found for the T100 photometric system work well. The median values of $|\Delta(B-V)|$ are smaller than 15 mmag for stars with $-0.4 < B-V\ (\mathrm{mag}) < 2.4$, while almost all median values of $|\Delta V|$ are smaller than 20 mmag for stars with $-0.2 < B-V\ (\mathrm{mag}) < 1.8$. Thus, we conclude that the T100's photometric system well matches that of Landolt's photometric systems for $B-V$ and V.

4. SUMMARY

We observed many standard stars selected from Landolt (2009, 2013) with the Bessell UBV filters during 50 nights from the year 2012 to 2024 with the 1-meter telescope (T100) of the TÜBİTAK National Observatory to perform photometric analysis of open clusters. As a byproduct, we derived precise transformation relations for the T100 photometric system.

1. Primary and secondary atmospheric extinction coefficients were determined for nights with photometric conditions. Median values of primary extinction coefficients were found to

be 0.481 ± 0.097, 0.303 ± 0.086, and 0.174 ± 0.050 for U, B, and V filters, respectively. Median secondary extinction coefficients k'_u and k'_b were calculated as -0.048 ± 0.164 and -0.034 ± 0.072, respectively. We found that primary extinction coefficients do not show a strong seasonal variation. We conclude that the median values of extinction coefficients estimated for summer and autumn are very similar within errors. Seasonal values of the coefficients and number of usable nights show that the winter and spring can not be favourite seasons for photometric observations at the TÜBİTAK National Observatory.

2. Our observations span a 12-year period form 2012 to 2024, excluding the years 2015 and 2017, allowing us to determine the variation in extinction coefficients over this time. We found that primary extinction coefficients decreased from the year 2012 to 2019, while they increased from 2019 to 2024, indicating deterioration of photometric conditions starting from the year 2019. No systematic variation in the secondary extinction coefficients could be identified.

3. The values of photometric zero points for B, $B-V$, and $U-B$ gradually become fainter during years, as expected. In addition, we found a "jump" of zero points to brighter magnitudes in August 2022, corresponding to the cleaning of the main mirror of the telescope.

4. We investigated the characteristics of atmospheric extinction based on scattering mechanisms. It is found that Rayleigh scattering is the main reason for atmospheric extinction in autumn and winter seasons, while aerosol scattering has some effect on the extinction in summer.

5. It is found that there are systematic differences for the U-band between the T100' and Landolt's photometric systems, although the median differences are relatively small for stars with $-0.5 < U-B$ (mag) < 1.6 and $0.2 < B-V$ (mag) < 1.8. This difference probably originates from the quantum efficiency of detectors used in the two photometric systems. We conclude that transformation equations found for the T100' photometric system work well for V and $B-V$ as the median values of $|\Delta(B-V)|$ and $|\Delta V|$ are small for a wide range of $B-V$ colour index. As a result, we also conclude that the T100's photometric system acceptably well matches that of Landolt's photometric systems for $U-B$, $B-V$, and V.

6. As a general result, we finally conclude that the transformation relations found in this study can be used for standardized photometry with T100's photometric system.

Peer Review: Externally peer-reviewed.

Author Contribution: Conception/Design of study - T.A., R.C., T.Y.; Data Acquisition - T.A., R.C., T.Y.; Data Analysis/Interpretation - T.A., R.C., T.Y.; Drafting Manuscript - T.A., R.C., T.Y.; Critical Revision of Manuscript - T.A., R.C., T.Y.; Final Approval and Accountability - T.A., R.C., T.Y.

Conflict of Interest: Authors declared no conflict of interest.

Financial Disclosure: This study has been supported in part by the Scientific and Technological Research Council (TÜBİTAK) 113F270.

Acknowledgements: We thank to TÜBİTAK National Observatory for partial support in using the T100 telescope with project numbers 15AT100-738 and 18CT100-1396. We also thank to the on-duty observers and members of the technical staff at the TÜBİTAK National Observatory for their support before and during the observations.

LIST OF AUTHOR ORCIDS

T. Ak https://orcid.org/0000-0002-0688-1983
R. Canbay https://orcid.org/0000-0003-2575-9892
T. Yontan https://orcid.org/0000-0002-5657-6194

REFERENCES

Golay M., 1974, Introduction to astronomical photometry, doi:10.1007/978-94-010-2169-2.

Janes K., Barnes S. A., Meibom S., Hoq S., 2013, AJ, 145, 7

Johnson H. L., Morgan W. W., 1953, ApJ, 117, 313

Kilkenny D., van Wyk F., Roberts G., Marang F., Cooper D., 1998, MNRAS, 294, 93

Landolt A. U., 2009, AJ, 137, 4186

Landolt A. U., 2013, AJ, 146, 131

Menzies J. W., Cousins A. W. J., Banfield R. M., Laing J. D., 1989, South African Astronomical Observatory Circular, 13, 1

Menzies J. W., Marang F., Laing J. D., Coulson I. M., Engelbrecht C. A., 1991, MNRAS, 248, 642

Sung H., Bessell M. S., 2000, Publ. Astron. Soc. Australia, 17, 244

İSTANBUL UNIVERSITY PRESS

Physics and Astronomy Reports
PAR 2024, 2 (2), 65–82
DOI: 10.26650/PAR.2024.00007

RESEARCH ARTICLE

An Updated Line List for Spectroscopic Investigation of G Stars - II: Refined Solar Abundances via Extended Wavelength Coverage to 10,000 Å

T. Şahin[1*,2], F. Güney[2], S.A. Şentürk[2], N. Çınar[2], and M. Marışmak[2]

[1] Akdeniz University, Faculty of Science, Department of Space Sciences and Technologies 07058, Antalya, Türkiye
[2] Institute of Graduate Studies in Science, Akdeniz University, Türkiye

ABSTRACT

This study introduces a line list for the abundance analysis of F-and G-type stars across the 4 080–9 675 Å wavelength range. A systematic search employing lower excitation potentials, accurate $\log gf$ values, and an updated multiplet table led to the identification of 592 lines across 33 species (25 elements), including C, O, Mg (ionized), Al, P, S, Cu, Zr (neutral), and La. To determine the uncertainties in $\log gf$ values, we assessed solar abundance using a very high-resolution ($R \approx 1\,000\,000$) disk-integrated solar spectrum. These lines were confirmed to be blend-free in the solar spectrum. The line list was further validated by analyzing the metal-poor star HD 218209 (G6V), which is notable for its well-documented and reliable abundance in literature. The abundances were obtained using the equivalent width (EW) method and further refined by applying the spectrum synthesis method. A comparative analysis with the *Gaia*-ESO line list v.6, provided by the *Gaia*-ESO collaboration, revealed additional neutral and ionized Fe lines. This extensively refined line list will facilitate precise stellar parameter determinations and accurate abundance analyses of spectra within the PolarBASE spectral library.

Keywords: Line: identification; Sun: abundances; Sun: fundamental parameters; Stars: individual (HD 218209)

1. INTRODUCTION

Advancements in spectroscopic methodologies for G-type stars have enabled more precise elemental abundance measurements. High-resolution spectroscopic techniques enable researchers to analyze stellar spectra in detail, providing insights into their atmospheric compositions and the underlying nucleosynthesis processes (Sharma et al. 2018; Trevisan et al. 2021). Analysis of G-dwarfs revealed discrepancies between the observed and predicted abundance patterns, challenging existing galactic chemical evolution models (Woolf & West 2012). These findings highlights the importance of combining improved modelling techniques with high-resolution spectroscopic data.

G-type stars, including the Sun, serve as fundamental benchmarks for understanding the stellar evolution and galactic chemical history (Bensby et al. 2003; Heiter et al. 2015). Their relatively long lifetimes allow them to retain the chemical signatures of the molecular clouds from which they form (Bensby et al. 2003; Heiter et al. 2015; Aoki et al. 2022). Solar photospheric abundances, derived from spectroscopic observations, provide a reference point for abundance determination in metal-poor stars and are essential for understanding the processes that govern stellar and galactic evolution (Lodders 2003; Pagel & Patchett 1975). Recent studies have significantly advanced our understanding of solar abundance by incorporating various physical processes, such as gravitational settling, convective overshooting, solar wind mass loss, pre-main-sequence disk accretion, opacity, and helium abundance in the solar corona (Wang & Zhao 2013; Zhang et al. 2019; Karathanou et al. 2020; Asplund et al. 2021; Salmon et al. 2021).

Migration complicates the interpretation of their origins because it can result in metal-poor stars being found in regions where they are not typically expected (Haywood 2008). Zhang et al. (2019) explored the implications of convective overshoot, solar-wind mass loss, and pre-main-sequence disk accretion on solar models. Their findings indicate that incorporating additional physical processes significantly improves the alignment between solar models and helioseismic constraints, effectively addressing the solar abundance problem. Karathanou et al. (2020) demonstrated how updated abundances can influence the internal solar structure via critical solar quantities such as temperature and pressure.

Asplund et al. (2021) presented the updated solar photospheric and proto-solar abundances of 83 elements. Their work highlighted the so-called solar modelling problem, which refers to the persistent discrepancies between helioseismic observations and solar interior models constructed with low metallicity. This suggests that there may be shortcomings in the computed opacities or the treatment of mixing processes below the con-

Corresponding Author: Timur Şahin **E-mail:** timursahin@akdeniz.edu.tr
Submitted: 05.11.2024 • **Accepted:** 27.12.2024

vection zone in the existing models. The updated abundances are essential for refining our understanding of the solar structure and evolution, as they provide a more accurate baseline for the solar modelling problem.

Moreover, the variability in helium abundance in the solar corona, as discussed by Ofman et al. (2024), also plays a role in understanding solar atmospheric processes. This variability is crucial for interpreting solar observations and for understanding the dynamics of the solar atmosphere. This study presents a three-dimensional model that illustrates the influence of solar activity and coronal heating processes on helium abundance.

These updates are essential for addressing the solar modelling problem and refining our understanding of the solar structure and evolution. Addressing this complex problem requires precise atmospheric modeling supported by comprehensive and accurate line lists.

The author's research team has been actively studying G-type stars, particularly those in solar neighborhoods. In our previous work (Şahin et al. 2023, hereafter Paper I), we presented a line list covering the 4 080-6 780 Å wavelength range designed for the spectroscopic analysis of more than 90 G-type metal-poor stars residing within the solar neighborhood. Previous studies by the research team, such as Marışmak et al. (2024) and Şentürk et al. (2024), also utilized the line list presented in Paper I. For instance, Marışmak et al. (2024) employed this line list to analyze two metal-poor high-proper motion stars, HD 8724 and HD 195633, whereas Şentürk et al. (2024) used it for spectroscopic analysis of a solar analogue star in the optical region.

Building on this foundation, we now extend the wavelength coverage of the line list to 10 000 Å, enabling a more comprehensive spectroscopic analysis of G-type stars, particularly in the near-infrared region. Şentürk et al. (2024) presented a line list covering the 10 000-25 000 Å range, which will be valuable for future spectroscopic studies of G-type stars, including solar analogue and solar twin stars in the H- and K-bands.

The remainder of this paper is organized as follows. Section 2 provides the observational data. Section 3 explains the methodology, including line identification and measurement procedures, the determination of model parameters, and the techniques for chemical abundance analysis of both HD 218209 and the Sun. Section 4 presents the line list, including details on line identification, measurement, and the atomic data used in the analysis. Finally, Section 5 summarizes our findings and discusses their implications.

2. OBSERVATIONS

This study analyzes high-resolution spectra of the Sun and HD 218209 to develop and validate a line list. Compared with Paper I, this study significantly expands the scope of spectral analyses by extending the analysis to the near-infrared region. For HD 218209, a high-resolution ($R \approx 76\,000$) and high signal-to-noise ratio ($S/N = 156$) PolarBASE[1] (Petit et al. 2014) Narval[2] spectrum (HJD 2456232.48238; exposure time of 400 s) obtained from the PolarBASE archive. The characteristics of the HD 218209's spectrum and KPNO solar spectrum are displayed in Figure 1.

The spectrum was continuum-normalized and corrected for radial velocity ($V_{\rm Rad}$) before line measurements. The Python interface and synthetic Narval solar spectra, which include atomic transitions in the range of 3 700–10 048 Å were used for RV correction ($V_{\rm Rad} = 16.03$ km s^{-1}), and the renormalization process was performed using the LIME code developed in the IDL environment (Şahin 2017). Lines with equivalent widths (EW) below 5 mÅ or above 200 mÅ were excluded from the analysis.

The solar spectrum serves as a fundamental reference for stellar astrophysics and analysis of physical processes in stars (Molaro & Monai 2012). In this study, high-resolution ($R \approx 700\,000$) Kitt Peak Fourier Transform Spectrometer (FTS) data (disk-integrated) obtained by Kurucz et al. (1984), previously utilized by Şahin et al. (2023), and a very high-resolution ($R \approx 1\,000\,000$) disk-integrated Göttingen (IAG)[3] solar flux atlas[4] obtained by Baker et al. (2020) with Vacuum Vertical Telescope (VVT) were used. However, it should be noted that an alternative link[5] was also provided by Baker et al. (2020). Differences[6] were observed between the two spectra (see Appendix for Figure A1). The KPNO solar spectrum was used for analyses in the 4 000-5 000 Å range, while the telluric-free IAG solar spectrum (BTFS) was preferred for the 5000-10000 Å range. Hence, both solar spectra have enabled line identification and other classical spectral analysis methods over the entire 4 000-10 000 Å wavelength range. Although the KPNO spectrum is reliable, it contains telluric lines within the ELODIE wavelength range; in particular, around 6 000 Å. In the longer wavelength regions, telluric bands caused by H_2O and molecular O_2 are prominent (see Figure 2 for details). In the KPNO solar spectrum, transitions outside the regions dominated by telluric lines were considered for the line list created in Paper I of the series, which covered 4 000-6 800 Å range. The 5 000-6 800 Å wavelength region is common between the KPNO and IAG (BTFS) solar spectra. We compared the equivalent widths (EW) of the lines in this region and found that the EW measurements of the two spectra were in good agreement [EW(KPNO) = (0.956±0.011)× EW(IAG)+(2.353±0.839)].

3. THE ABUNDANCE ANALYSIS

The elemental abundances were determined using the local thermodynamic equilibrium (LTE) line analysis code, MOOG

[1] http://polarbase.irap.omp.eu
[2] Narval spectropolarimeter is adapted to the 2m Bernard Lyot telescope and provides high-resolution spectral and polarimetric data.
[3] IAG: Institute for Astrophysics, Göttingen.
[4] BTFS; https://zenodo.org/records/3598136
[5] zenodo; https://web.sas.upenn.edu/ashbaker/solar-atlas/
[6] Ashley Baker; private communication

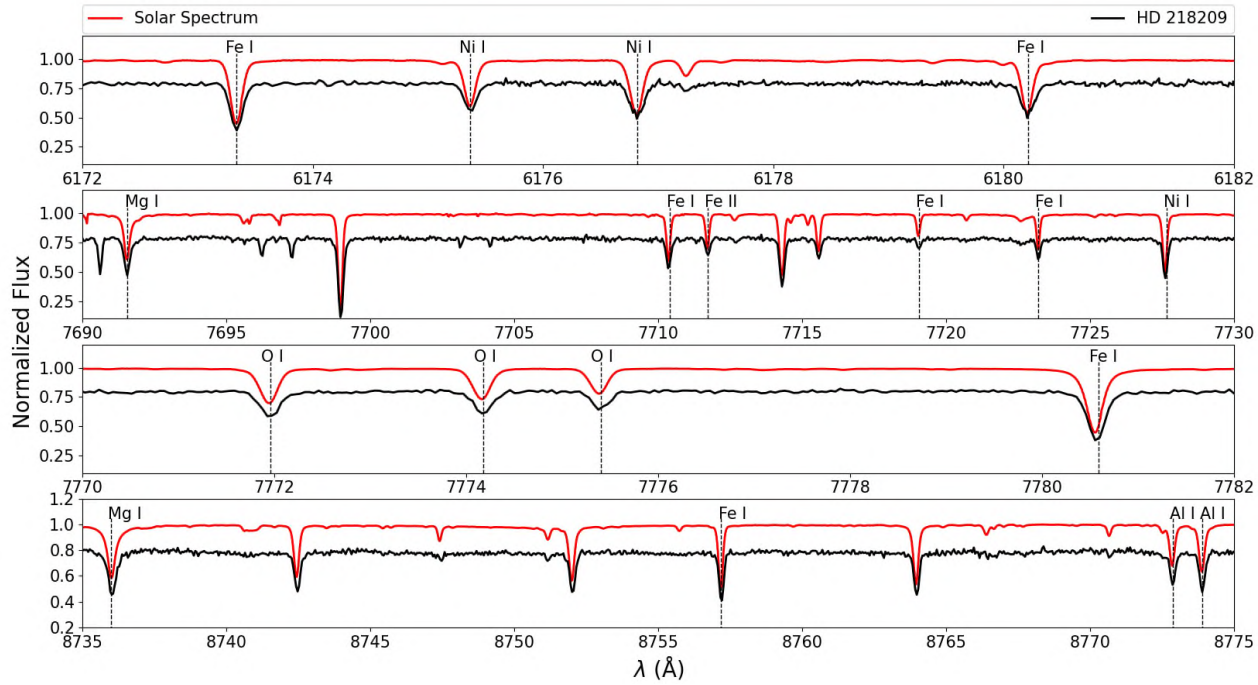

Figure 1. A small region of the KPNO solar spectrum and the PolarBASE spectrum of HD 218209. Identified lines are also indicated.

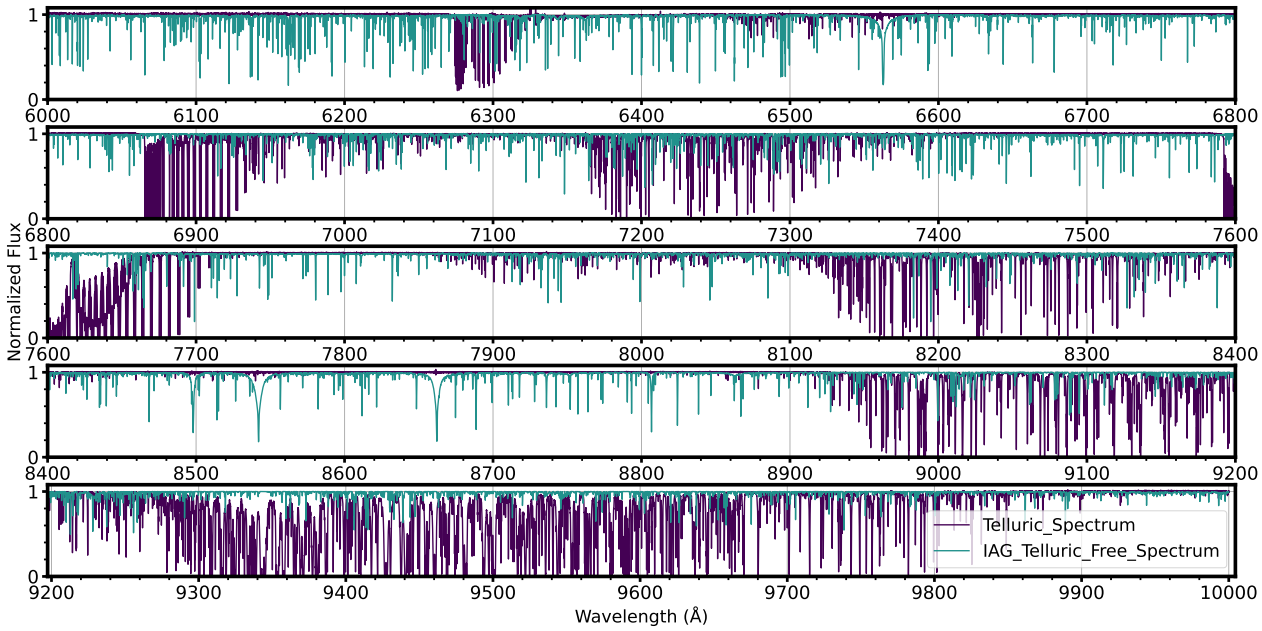

Figure 2. The telluric corrected Göttingen (IAG) Solar Spectrum (BTFS). Telluric spectrum (from https://zenodo.org/records/3598136) was also included to indicate the positions of the telluric lines. The telluric model shown is typical of the conditions at Göttingen (precipitable water vapour of ≈10 mm), where the VVT telescope resides.

(Sneden 1973)[7]. Model atmospheres were generated using ATLAS9 code (Castelli & Kurucz 2003) with the LTE (ODFNEW) approach. Detailed descriptions of the abundance analysis procedure have been provided by Şahin & Lambert (2009), Şahin et al. (2011), Şahin et al. (2016), Şahin & Bilir (2020), and Şahin et al. (2023). The atmospheric parameters of the model, such as the effective temperature ($T_{\rm eff}$), surface gravity ($\log g$), metallicity ([Fe/H]), and microturbulent velocity (ξ), were determined using neutral (Fe I) and ionized (Fe II) iron lines in an iterative process. The $T_{\rm eff}$ determination employed the excitation balance method (sensitive to neutral spectral lines with a

[7] The source code for MOOG can be accessed at http://www.as.utexas.edu/chris/moog.html

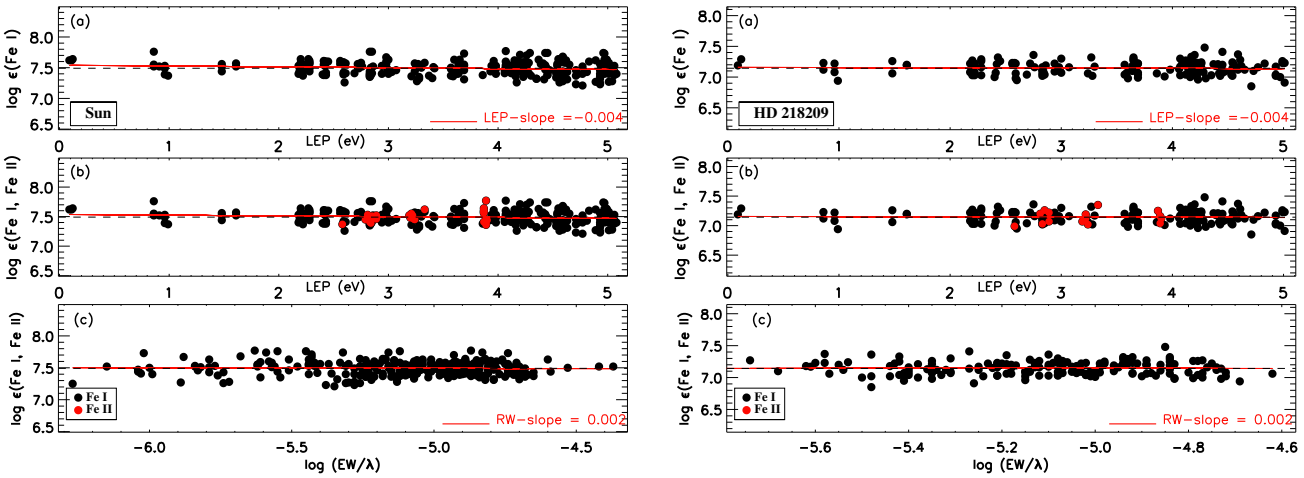

Figure 3. An example for the determination of the atmospheric parameters $T_{\rm eff}$ and ξ using abundance (log ϵ) as a function of both lower LEP (panels a and b) and reduced EW (panels c) for the Sun and HD 218209. In all panels, the solid red line represents the least-squares fit to the data.

broad range of excitation potentials) for Fe I. ξ represents the small-scale gas motion within the stellar atmosphere. ξ was determined by ensuring that the abundance of Fe atoms (Fe I) remained independent of the reduced equivalent width (EW/λ) under the assumption of LTE. These two conditions were simultaneously applied to a set of Fe I lines (see Figure 3, upper and middle panels). In addition, ξ is determined using a dispersion test for a given model atmosphere (Figure A2). This involved computing the dispersion in abundance (Fe, Ti, Cr) over the range of 0.0 to 3.0 km s^{-1}. By combining both methods, the measurement uncertainty for ξ was estimated as 0.5 km s^{-1} (Figure A2). In the same figure, an example Kiel diagram is included.

Surface gravity (log g) was determined by analyzing Fe abundances calculated with MOOG, ensuring ionization equilibrium where Fe I and Fe II lines yield the same abundance. Notably, in the solar spectrum, ionization equilibrium is achieved between the neutral and ionized atoms of Mg, Sc, Ti, Cr, and Zr. Similarly, in the spectrum of HD 218209, in addition to Fe, ionization equilibrium is reached for Ti and Cr. Finally, the metallicity ([Fe/H]) was refined through an iterative process to achieve convergence between the derived Fe abundance and the initial abundance adopted for the model atmosphere construction. Convergence was achieved by adjusting $T_{\rm eff}$, log g, and ξ of the model. Figure 3 illustrates a summary of the relationship between the physical parameters used to determine the stellar model parameters using the classical spectroscopic method (i.e., ionization and excitation equilibria of the Fe lines) for the Sun (left panel) and HD 218209 (right panel).

The uncertainty in the derived $T_{\rm eff}$ originates from the error associated with the slope of the relationship between the Fe I abundance and the LEPs of the lines. Additionally, a 1σ difference in abundance ([X/H]) between the Fe I and Fe II lines corresponds to a change in 0.19 dex in log g. Table 1 summarizes the resulting model parameters for HD 218209 and the Sun. The uncertainties in the atomic data (log gf values) were

Table 1. Model atmosphere parameters for HD 218209, and the Sun.

Star	$T_{\rm eff}$ (K)	log g (cgs)	[Fe/H] (dex)	ξ (km s^{-1})
HD 218209	5600^{+177}_{-177}	$4.50^{+0.24}_{-0.24}$	$-0.36^{+0.13}_{-0.13}$	$0.44^{+0.50}_{-0.50}$
Sun †	5770^{+130}_{-130}	$4.40^{+0.19}_{-0.19}$	$0.00^{+0.09}_{-0.09}$	$0.66^{+0.50}_{-0.50}$
Sun *	5790^{+45}_{-45}	$4.40^{+0.09}_{-0.09}$	$0.00^{+0.04}_{-0.04}$	$0.66^{+0.50}_{-0.50}$

(†): This study (TS), the solar spectrum was provided by Baker et al. (2020).
(*): The atmospheric parameters from Şahin et al. (2023). The solar spectrum was obtained from Kurucz et al. (1984).

assessed by deriving solar abundances from the stellar spectral lines. The solar model derived from our analysis yielded the following atmospheric parameters: $T_{\rm eff}$ = 5770 K, log g = 4.40 cgs, [Fe/H] = 0.00 dex, and ξ = 0.66 km s^{-1}. These values are in good agreement with the standard solar models. The abundances obtained for the solar photosphere as a result of solar analysis were calculated using these model parameters (Table 1). In Table 1, the solar abundances reported by Asplund et al. (2009, 2021) are also included. In Table 2, we provide a summary of element abundances based on the model parameters in LTE. log ϵ is the logarithm of abundance. The errors reported in log ϵ abundances are represented by 1σ line-to-line scatter in abundance. [X/H] is the logarithmic abundance ratio of hydrogen to the corresponding solar values and [X/Fe] is the logarithmic abundance considering the abundance of Fe I. The error in [X/Fe] is the square root of the sum of the quadratures of the errors in [X/H] and [Fe/H]. Table 2 presents the abundances obtained using PolarBase spectrum of the star as a function of the [X/Fe] ratio.

An analysis of the chemical abundances of 33 species belonging to 27 elements, as presented in Table 2, was consistent

Table 2. The abundances of the observed species for Sun and HD 218209. The solar abundances obtained in this study and those reported by Asplund et al. (2009, ASP09) and Asplund et al. (2021, ASP21) are also provided. Abundances in bold are those calculated via the spectrum synthesis method.

	HD 218209						Sun								
Species	$[X/Fe]^{\dagger}$	σ	n	$\log\epsilon_{\odot}(X^{\dagger})$	σ	n	$\log\epsilon_{\odot}(X^{*})$	σ	n	$\log\epsilon_{\odot}(X_{\rm ASP09})$	σ	$\Delta\log\epsilon_{\odot}(X_1)$	$\log\epsilon_{\odot}(X_{\rm ASP21})$	σ	$\Delta\log\epsilon_{\odot}(X_2)$
	(dex)			(dex)			(dex)			(dex)		(dex)	(dex)		(dex)
C I	**0.14**	**0.22**	**2**	**8.48**	**0.11**	**2**	–	–	–	8.43	0.05	0.05	8.46	0.04	0.02
O I	**0.28**	**0.15**	**3**	**8.81**	**0.03**	**3**	–	–	–	8.69	0.05	0.12	8.69	0.04	0.12
Na I	-0.03	0.20	4	6.22	0.12	4	6.16	0.07	2	6.24	0.04	-0.02	6.22	0.03	0.00
Mg I	**0.24**	**0.16**	**5**	**7.62**	**0.03**	**5**	7.60	0.08	2	7.60	0.04	0.02	7.55	0.03	0.07
Mg II	–	–	–	**7.63**	**0.00**	**1**	–	–	–	7.60	0.04	0.03	7.55	0.03	0.08
Al I	**0.13**	**0.16**	**8**	**6.43**	**0.03**	**8**	–	–	–	6.45	0.03	-0.02	6.43	0.03	0.00
Si I	0.13	0.18	16	7.50	0.09	21	7.50	0.07	12	7.51	0.03	-0.01	7.51	0.03	-0.01
P I	–	–	–	**5.51**	**0.06**	**3**	–	–	–	5.41	0.03	0.10	5.41	0.03	0.10
S I	–	–	–	**7.15**	**0.00**	**2**	–	–	–	7.12	0.03	0.03	7.12	0.03	0.03
Ca I	0.15	0.20	15	6.29	0.09	21	6.34	0.08	18	6.34	0.04	-0.05	6.30	0.03	-0.01
Sc I	–	–	–	**3.13**	**0.00**	**1**	3.12	0.00	1	3.15	0.04	-0.02	3.14	0.04	-0.01
Sc II	0.06	0.14	2	3.14	0.02	12	3.23	0.08	7	3.15	0.04	-0.01	3.14	0.04	0.00
Ti I	0.21	0.21	44	4.93	0.09	63	4.96	0.09	43	4.95	0.05	-0.02	4.97	0.05	-0.04
Ti II	0.20	0.21	7	5.01	0.11	11	4.99	0.08	12	4.95	0.05	0.06	4.97	0.05	0.04
V I	**0.01**	**0.15**	**3**	**3.90**	**0.03**	**5**	3.99	0.05	5	3.93	0.08	-0.03	3.90	0.08	0.00
Cr I	-0.02	0.19	17	5.68	0.09	29	5.71	0.07	19	5.64	0.04	0.04	5.62	0.04	0.06
Cr II	0.01	0.20	3	5.64	0.11	4	5.64	0.14	3	5.64	0.04	0.00	5.62	0.04	0.02
Mn I	**-0.27**	**0.18**	**14**	**5.45**	**0.08**	**14**	5.62	0.13	13	5.43	0.05	0.02	5.42	0.06	0.03
Fe I	0.01	0.21	152	7.50	0.11	252	7.54	0.09	132	7.50	0.04	0.00	7.46	0.04	0.04
Fe II	0.00	0.20	17	7.50	0.09	32	7.51	0.04	17	7.50	0.04	0.00	7.46	0.04	0.04
Co I	**-0.10**	**0.17**	**6**	**4.95**	**0.06**	**8**	–	–	–	4.99	0.07	-0.04	4.94	0.05	0.01
Ni I	-0.02	0.20	45	6.25	0.10	66	6.28	0.09	54	6.22	0.04	0.03	6.20	0.04	0.05
Cu I	**-0.13**	**0.20**	**3**	**4.20**	**0.06**	**4**	–	–	–	4.19	0.04	0.01	4.18	0.05	0.02
Zn I	**0.20**	**0.15**	**2**	**4.63**	**0.02**	**2**	4.68	0.03	2	4.56	0.05	0.07	4.56	0.05	0.07
Sr I	**-0.18**	**0.14**	**1**	**2.84**	**0.00**	**1**	2.91	0.00	1	2.87	0.07	-0.03	2.83	0.06	0.01
Y II	**-0.14**	**0.15**	**2**	**2.28**	**0.02**	**2**	2.29	0.05	2	2.21	0.05	0.07	2.21	0.05	0.07
Zr I	–	–	–	2.53	0.00	1	–	–	–	2.58	0.04	-0.05	2.59	0.04	-0.06
Zr II	0.04	0.14	1	2.61	0.02	2	2.68	0.00	1	2.58	0.04	0.03	2.59	0.04	0.02
Ba II	**0.04**	**0.14**	**2**	**2.32**	**0.02**	**2**	2.24	0.06	4	2.18	0.09	0.14	2.27	0.05	0.05
La II	**0.03**	**0.16**	**2**	**1.14**	**0.05**	**3**	–	–	–	1.10	0.04	0.04	1.11	0.04	0.03
Ce II	**0.26**	**0.15**	**1**	**1.60**	**0.04**	**3**	1.64	0.02	2	1.58	0.04	0.02	1.58	0.04	0.02
Nd I	**0.08**	**0.15**	**1**	**1.36**	**0.03**	**3**	1.42	0.05	3	1.42	0.04	-0.06	1.42	0.04	-0.06
Sm II	**0.14**	**0.14**	**1**	**0.95**	**0.02**	**2**	0.96	0.00	1	0.96	0.04	-0.01	0.95	0.04	0.00

(†): This study, (*): Şahin et al. (2023), $\Delta\log\epsilon_{\odot}(X_1) = \log\epsilon_{\odot}(X^{\dagger}) - \log\epsilon_{\odot}(X_{\rm ASP09})$, $\Delta\log\epsilon_{\odot}(X_2) = \log\epsilon_{\odot}(X^{\dagger}) - \log\epsilon_{\odot}(X_{\rm ASP21})$

with the solar chemical abundances established by Asplund et al. (2009, 2021). The abundances of C, O, Mg, Al, P, S, Sc, Ti, V, Mn, Co, Cu, Zn, Sr, Y, Zr, Ba, La, Ce, Nd, and Sm reported in Table 2 were determined using both the equivalent width (EW) method and spectrum synthesis techniques. The synthetic spectra calculated for some sample lines (C I 9 111 Å, O I 7 772 Å, Mg I 5 711 Å, and Cu I 5 105 Å), whose elemental abundances were checked using the spectrum synthesis technique, are shown in Figure 4. On the other hand, when compared to the solar abundances reported by Asplund et al. (2009), the scatter among the elements ranges from -0.07 dex for Na to 0.16 dex for O. For the remaining 31 species, the average scatter in abundance ($\log\epsilon_{\odot}(X_{\rm ASP09})$) is 0.02±0.04 dex. Asplund et al. (2021) presented a revised solar chemical composition, with notable changes observed in the abundance of elements such as Ba, Mg, Co, Sr, Fe, and Ca. For instance, the abundance value obtained for Ba is 0.11 dex higher than that reported by Asplund et al. (2009) but shows better agreement with the values presented by Asplund et al. (2021). Similarly, a lower scatter was observed for Na compared to the results of Asplund et al. (2009).

The results can be affected by various systematic uncertainties, including those related to the correction of non-LTE effects on the formation of convection and atomic transitions. To investigate the potential convective effect, two different mixing length parameters (α) were calculated in this study using equations based on 2D hydrodynamic models from Ludwig et al. (1999) and 3D hydrodynamic models from Magic et al. (2015).

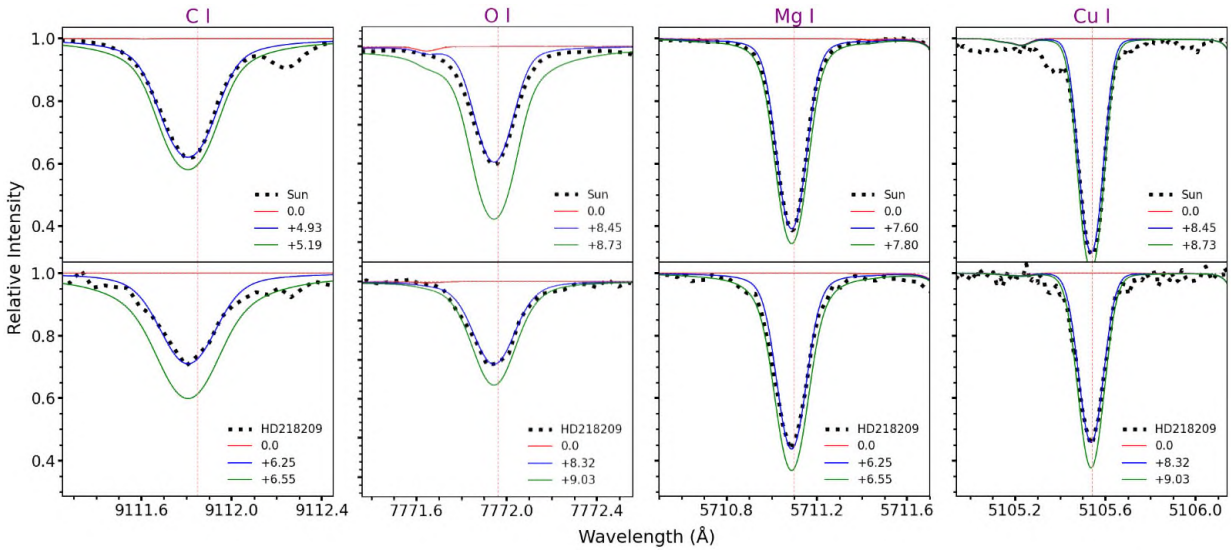

Figure 4. The figure presents observed (filled circles) and computed (full blue line) line profiles for C I 9 111 Å, O I 7 772 Å, Mg I 5 711 Å, and Cu I 5 105 Å in both the Sun (upper panels) and HD 218209 (bottom panels). The computed profiles represent the synthetic spectra derived from three logarithmic abundances. The red lines depict the spectra computed without considering the contributions from ionized metal lines.

The formula by Magic et al. (2015) yielded an α value of 1.99, whereas the formula by Ludwig et al. (1999) yielded an α value of 1.60. Two different ATLAS9 models were constructed for the two mixing-length parameters. The synthetic spectra calculated using these models were compared to the observed spectrum of HD 218209. Although no significant difference was observed, the synthetic spectrum derived from the mixing length parameter obtained by Magic et al. (2015) was found to be in slightly better agreement with the observed spectrum.

Given that the Fe I and Fe II abundances were used to constrain the model atmospheric parameters in this study, we must consider the non-LTE effects on Fe. These effects were found to be negligible (0.00 dex) for both solar and stellar Fe II lines (Bergemann et al. 2012a; Lind et al. 2012; Bensby et al. 2014). For Fe I lines with low excitation potentials (<8 eV) and metallicities [Fe/H] > -3.0 dex, the non-LTE deviations were minimal according to K (Lind et al. 2012). The non-LTE corrections (Bergemann et al. 2012b) for 66 Fe I lines in the IAG solar spectrum and 56 Fe I lines in HD 218209 were found to be 0.01 dex. Similar trends were observed for the other elements in both the Sun and Star. For example, the non-LTE corrections (Sun/Star) for Si I (-0.01/0.00), Ca I (-0.01/-0.01), Ti I (0.10/0.13), Ti II (-0.01/0.00), Cr I (0.05/0.08), Mn I (0.05/0.12), and Co I (0.11/0.15) were generally small, with the largest corrections found for Ti and Co

3.1. Notes on the errors for model atmospheric parameters of the Sun

The solar spectrum is used as a standard reference spectrum for the spectroscopic analysis of F-G-K-type stars, in both the optical and NIR regions (Şahin & Bilir 2020; Şahin et al. 2023; Şentürk et al. 2024). This is mainly due to the well-characterized atmosphere of the Sun and extensive observational data in the optical and IR regions. Many published NIR line lists include lines with poorly defined or calibrated oscillator strengths, often relying on theoretical calculations (e.g., Ryde et al. 2009). In particular, a recent spectroscopic study of a solar analogue star, HD 76151, in the Y, J, H, and K bands by Şentürk et al. (2024) provides a detailed review of the line libraries published in the infrared region over the last 40 years in terms of $\log gf$ values and atomic data.

In the first paper of the series (Şahin et al. 2023), the effective temperature obtained from the solar atmosphere analysis differed by 20 K from the effective temperature value obtained in this study. This difference is consistent with the error values. Similarly, a significant difference in Paper I is the increase in the reported errors for $T_{\rm eff}$, $\log g$ because of the increase in the error for metallicity ($\Delta\sigma$[Fe/H] = 0.05 dex). For $T_{\rm eff}$, $\Delta\sigma T_{\rm eff}$ = 85 K and for $\log g$, $\Delta\sigma \log g$ = 0.10 cgs. In this study, we obtained an additional 187 atomic transitions in the near-IR region. In addition, two different solar spectra were preferred for the solar abundance analysis. The KPNO solar spectrum is in the 4 000-5 000 Å region and the IAG solar spectrum is in the 5 000-10 000 Å region.

The following subsections provide details of the line list and atomic data.

4. LINE LIST: IDENTIFICATION, LINE MEASUREMENT, AND ATOMIC DATA

Initially, the centers of the lines exhibiting Gaussian profiles appropriate for equivalent width analysis within the range of 4 000-10 000 Å were identified in the KPNO (Kurucz et al. 1984) and IAG solar spectra (Baker et al. 2020, BTFS). The established line centers for the selected isolated lines were compared with the wavelengths identified in the laboratory envi-

ronment within the Revised Multiplet Table (RMT) (Moore et al. 1966). Subsequently, a multiplet (cf. Moore 1954) analysis technique was applied. The relative intensities of the lines within a multiplet are generally insensitive to variations in the excitation conditions in most spectroscopic sources. A standard approach involves verifying the presence of multiple members with expected relative intensities. Subsequent analyses focused on identifying lines that exhibited similar excitation and laboratory strengths.

The common wavelength range of the first article of the series and this study was 4 024-6 772 Å. In this range, 54 atomic transitions from 19 species of 17 elements were added to the first report on this series. The distributions of these transitions are Na I (one line), Al I (two lines), Si I (two lines), Ca I (two lines), Sc II (five lines), Ti I (four lines), V I (one line), Cr II (one line), Mn I (one line), Fe I (17 lines), Fe II (six lines), Co I (two lines), Cu I (two lines), Zr I (one line), Zr II (one line), La II (three lines), Ce II (one line), Nd II (one line) and Sm II (one line). In the region 6 772[8]-9 944 Å, 189 atomic transitions from 27 species of 23 elements were added to the line list. The distributions of these transitions are C I (two lines), O I (three lines), Na I (two lines), Mg I (three lines), Mg II (one line), AI I (eight lines), Si I (nine lines), P I (three lines), S I (two lines), Ca I (six lines), Sc II (five lines), Ti I (20 lines), V I (one line), Cr I (10 lines), Cr II (one line), Mn I (one line), Fe I (123 lines), Fe II (15 lines), Co I (three lines), Ni I (13 lines), Cu I (four lines), Zr I (one line), Zr II (one line), La II (three lines), Ce II (one line), Nd I (two lines), and Sm II (one line). In total, 13 atomic transitions from seven species of seven elements were included in the first article of the series but were not included in this study. The statistics of these transitions are as follows: Ca I (three lines), Ti II (one line), Fe I (three lines), Co I (two lines), Ni I (one line), Zr II (one line), and Nd II (two lines). Lower-level excitation potential (L.E.P) values for the new line list were obtained from the MOORE catalogue (Moore et al. 1966).

Accurate determination of elemental abundances in stars requires precise knowledge of the atomic transition probability, quantified by the $\log gf$ value. This study utilized a comprehensive compilation of $\log gf$ values from recent literature, including Biemont & Godefroid (1980); Biemont et al. (1981), Hannaford et al. (1982), Klose et al. (2002), Takeda et al. (2003), Fuhr & Wiese (2006), Kelleher & Podobedova (2008), Lawler et al. (2009), Den Hartog et al. (2011), Shi et al. (2011), Hansen et al. (2013), Lawler et al. (2006, 2013, 2015, 2017, 2019), Pehlivan Rhodin et al. (2017), and Den Hartog et al. (2021). For transitions not documented in these sources, data from the NIST[9] and VALD[10] atomic line databases were used. When multiple sources were available, the $\log gf$ value that yielded the most consistent abundance with solar abundance values reported by Asplund et al. (2009, 2021) was prioritized. References for the adopted $\log gf$ values and corresponding RMT numbers for each line are tabulated in Tables A1, A2, A3, A4, and A5.

Table 3. Comparison of $\log gf$ values for common lines in GESv6. The number of common lines (n) was also reported. The mean of the $\log gf$ differences ($\Delta \log gf$) for each element is also reported.

Element	n	$\Delta \log(gf)$ (dex)	σ (dex)	Element	n	$\Delta \log(gf)$ (dex)	σ (dex)
C I	2	-0.02	0.02	Mn I	12	0.68	0.83
O I	3	0.00	0.00	Fe I	236	0.00	0.16
Na I	4	0.01	0.02	Fe II	28	0.00	0.07
Mg I	5	0.32	0.54	Co I	7	1.33	1.03
Mg II	1	-0.01	0.00	Ni I	66	-0.04	0.10
Al I	8	0.29	0.58	Cu I	4	0.27	0.26
Si I	19	-0.01	0.11	Zn I	2	-0.03	0.02
S I	2	-0.29	0.24	Sr I	1	0.00	0.00
Ca I	20	0.00	0.04	Y II	2	-0.07	0.05
Sc II	12	0.02	0.06	Zr I	1	0.00	0.00
Ti I	56	0.00	0.03	Ba II	2	-0.02	0.01
Ti II	11	0.04	0.11	La II	2	-0.01	0.01
V I	5	0.71	0.61	Ce II	2	0.00	0.00
Cr I	26	0.07	0.49	Nd II	2	0.00	0.00
Cr II	4	0.12	0.20	Sm II	2	0.00	0.00

$\Delta \log(gf) = \log(gf)_{\text{This Study}} - \log(gf)_{\text{GESv6}}$

Further verification of the $\log gf$ values was performed by comparing the $\log gf$ values used in this study with those in the *Gaia*-ESO line list v.6 provided by GES collaboration (Heiter et al. 2021). Note that the gf values for the chosen lines of Fe I and Fe II in this study were obtained from Fuhr & Wiese (2006). The GES line list contains the recommended lines and atomic data (i.e., gf values corrected for the hyperfine structure) for the analysis of FGK stars. Notably, several lines in the spectra of FGK stars have not yet been identified (Heiter et al. 2015).

The GES line list (v.6) comprises 141 233 lines spanning a 4 200-9 200Å. A total of 561 lines were analyzed in this study, of which 548 were common to the GES line list. These 592 atomic transitions involve 30 species from 26 elements. A total of 40 atomic transitions were included in this study's line list in the regions outside the GES line list boundaries (lower limit: 4 021-4 200 Å and upper limit: 9 200-9 944 Å). In the spectral region overlapping with the GES line list (4 200-9 200 Å), additional Fe I (8958.88 Å), and Fe II (6806.85 Å, 6810.28 Å, 6820.43 Å) atomic transitions were found compared to the GES line list. Of the 55 lines identified in this study within the same wavelength range, 51 were found in the GES line list. This wavelength range aligns with the PolarBASE spectrum of HD 218209 used in this analysis.

For the 236 common Fe I lines in the GES line list, the difference in the $\log gf$ value was 0.00 ± 0.16 dex. For the 28 Fe II lines, the difference in the $\log gf$ values was 0.00 ± 0.07 dex. A detailed comparison of the $\log gf$ values was performed for

[8] Upper wavelength limit from Şahin et al. (2023) is 6 780 Å.
[9] http://physics.nist.gov/PhysRefData/ASD
[10] https://vald.astro.uu.se/

the 548 lines common to both line lists, as listed in Table 3 which summarises the mean difference in log gf values and the corresponding standard deviations for each element with at least two common lines. The results show overall good agreement between the two line lists, though significant differences were observed for certain elements, such as Co and Mn. These discrepancies can be attributed to various factors including differences in the atomic data used to construct the line lists, uncertainties in the line identification process, and the presence of non-LTE effects.

Figure 5 presents the numerical statistics for the final line list generated in this study are shown in Figure 5. The same figure shows the number of lines in the spectral region of 50 Å each.

5. CONCLUSION

This study presents an expanded line list covering the wavelength range of 4 080–10 000 Å for abundance analyses of F- and G-type stars. Although Paper I reported 363 atomic transitions, only 592 lines were reported in this study. The line list was compared with the existing *Gaia*-ESO v6 line list (Table 3), and a 93% overlap was found, with 548 of the 592 line matches.

Utilizing high-resolution solar spectra from IAG (5 000-10 000 Å, R ≈1 000 000) and KPNO (4 000-6 780 Å, R≈700 000), 592 spectral lines belonging to 33 chemical species were identified and included in the abundance analysis. Compared to the previous paper in this series, not only has the wavelength range extended, but elements such as C, O, Al, P, S, Co, Cu, Zr, and La have also been added to the list.

Additionally, the abundances of C, O, Mg, Al, P, S, Sc, V, Mn, Co, Cu, Zn, Sr, Y, Zr, Ba, La, Ce, Nd, and Sm were determined using the synthesis method. To calculate the reported abundances, it was assumed that the solar spectrum was disk-integrated[11].

A comparison of the elemental abundances ([X/Fe]) reported in this study for HD 218209 with those presented by (Şahin et al. 2023) reveals several differences. No significant differences were observed for Cr II, Ti I, V I, Sr I, and Zr II ($\Delta \log_\epsilon = 0.00$ dex). Elements exhibiting a difference of -0.01 dex include Fe I, Ni I, Cr I, Ca I, and Nd II. A difference of 0.06 dex was observed for Ce II, Ba II, and Sc II. Other notable differences include -0.02 dex for Na I and Ti II, 0.01 dex for Si I, 0.07 dex for Y II, 0.05 dex for Mn I, 0.02 dex for Zn I, 0.09 dex for Co I, and 0.04 dex for Mg I.

In this study, we employed both equivalent width (EW) measurements and spectrum synthesis techniques to determine the elemental abundances in the solar and HD 218209 spectra. The resulting abundances were compared to those reported by Asplund et al. (2009) and Asplund et al. (2021) as well as other solar abundance values found in the literature (Table A6). Our results are in excellent agreement with those of the previous studies. Notably, the revision of Ba abundance in Asplund et al. (2021) significantly reduced the discrepancy between the two studies.

Having accurately determined the solar abundances using a constructed line list, we applied a similar methodology to the star, HD 218209. Table A7 presents a comparison of the effective temperature, surface gravity, metallicity, and derived chemical abundances of this star. A thorough examination of the available abundance data for HD 218209 revealed a scarcity of literature regarding the abundance of several elements (C, O, Cr, Co, Cu, Zn, Sr, Y, Zr, Ba, La, Ce, Nd, and Sm). This highlights the significant contributions of our study to this field. A detailed element-by-element literature analysis is provided in Appendix A1.

Peer Review: Externally peer-reviewed.

Author Contribution: Conception/Design of study - T.Ş.; Data Acquisition - T.Ş., F.G., M.M., S.A.Ş; Data Analysis/Interpretation - T.Ş., F.G., S.A.Ş., M.M., N.Ç.; Drafting Manuscript - T.Ş.; Critical Revision of Manuscript - T.Ş.; Final Approval and Accountability - T.Ş., F.G., S.A.Ş., M.M., N.Ç.; Technical or Material - T.Ş., M.M., F.G.; Support Supervision - T.Ş.

Conflict of Interest: Authors declared no conflict of interest.

Financial Disclosure: This study was supported by the Scientific and Technological Research Council of Turkey (TUBITAK) under Grant Number 121F265. The authors thank TUBITAK for their support.

Acknowledgements: This study used NASA's Astrophysics Data System and the SIMBAD database operated at CDS, Strasbourg, France. The nonpublic data underlying this article will be made available upon reasonable request from the authors.

Software: LIME (Şahin 2017), SPECTRE (Sneden 1973), MOOG (Sneden 1973)

LIST OF AUTHOR ORCIDS

T. Şahin https://orcid.org/0000-0002-0296-233X
F. Güney https://orcid.org/0000-0003-3884-974X
S.A. Şentürk https://orcid.org/0000-0003-3863-6525
N. Çınar https://orcid.org/0000-0002-5155-9280
M. Marışmak https://orcid.org/0000-0002-9397-2778

REFERENCES

Abia C., Rebolo R., Beckman J. E., Crivellari L., 1988, A&A, 206, 100

Aoki W., Matsuno T., Parthasarathy M., 2022, PASJ, 74, 1368

Asplund M., Grevesse N., Sauval A. J., Scott P., 2009, ARA&A, 47, 481

Asplund M., Amarsi A. M., Grevesse N., 2021, A&A, 653, A141

[11] At this point, the flux/int switch in the abfind and synth drivers of the MOOG code, which we used to determine model atmosphere parameters and abundance calculations under LTE conditions, was set to zero.

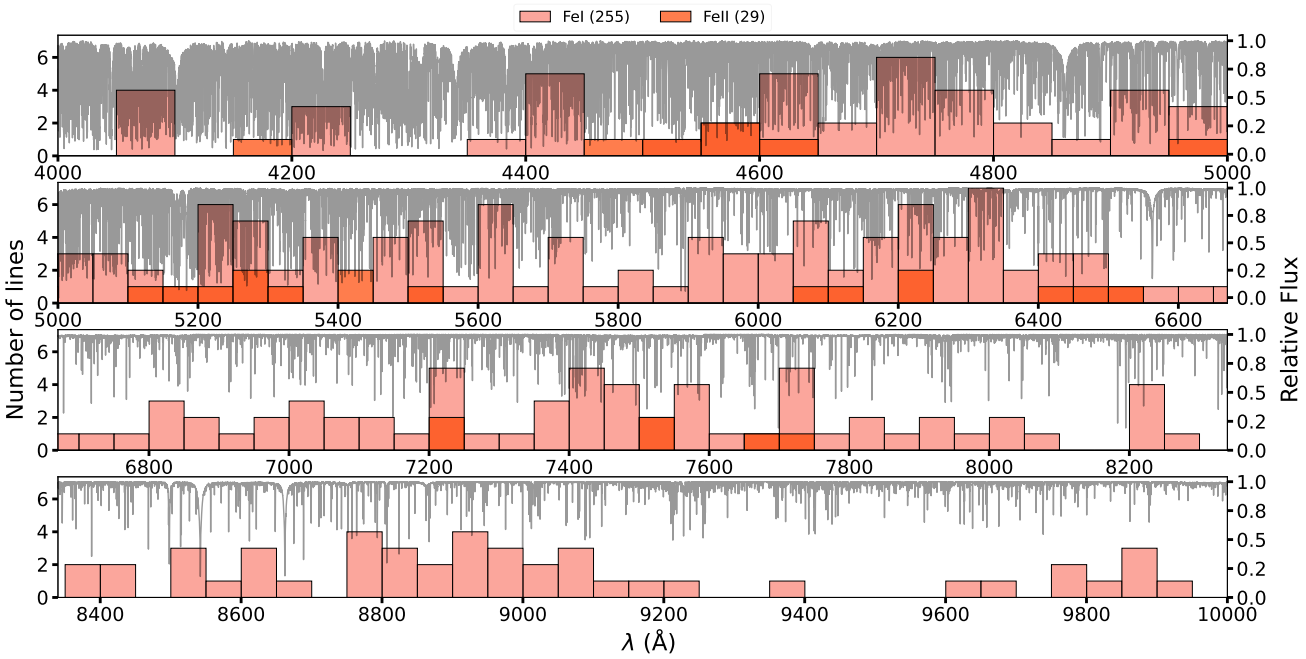

Figure 5. The figure displays the telluric-free Solar spectrum obtained from Baker et al. (2020), along with the number of identified lines within each 50 Å region of the spectrum. The 4 000 - 5 000 Å spectral range is based on solar data from Kurucz et al. (1984), while the 5 000 - 10 000 Å range utilizes the telluric-free Solar spectrum (BTFS) provided by Baker et al. (2020).

Baker A. D., Blake C. H., Reiners A., 2020, ApJS, 247, 24

Bensby T., Feltzing S., Lundström I., 2003, A&A, 410, 527

Bensby T., Feltzing S., Oey M. S., 2014, A&A, 562, A71

Bergemann M., Lind K., Collet R., Magic Z., Asplund M., 2012a, MNRAS, 427, 27

Bergemann M., Kudritzki R.-P., Plez B., Davies B., Lind K., Gazak Z., 2012b, ApJ, 751, 156

Biemont E., Godefroid M., 1980, A&A, 84, 361

Biemont E., Grevesse N., Hannaford P., Lowe R. M., 1981, ApJ, 248, 867

Biemont E., Hibbert A., Godefroid M., Vaeck N., 1993, ApJ, 412, 431

Caffau E., Steffen M., Sbordone L., Ludwig H. G., Bonifacio P., 2007, A&A, 473, L9

Caffau E., Ludwig H. G., Steffen M., Ayres T. R., Bonifacio P., Cayrel R., Freytag B., Plez B., 2008, A&A, 488, 1031

Caffau E., Maiorca E., Bonifacio P., Faraggiana R., Steffen M., Ludwig H. G., Kamp I., Busso M., 2009, A&A, 498, 877

Caffau E., Ludwig H. G., Bonifacio P., Faraggiana R., Steffen M., Freytag B., Kamp I., Ayres T. R., 2010, A&A, 514, A92

Caffau E., Ludwig H. G., Steffen M., Freytag B., Bonifacio P., 2011, Sol. Phys., 268, 255

Caffau E., et al., 2019, A&A, 622, A68

Castelli F., Kurucz R. L., 2003, in Piskunov N., Weiss W. W., Gray D. F., eds, IAU Symposium Vol. 210, Modelling of Stellar Atmospheres. p. A20 (arXiv:astro-ph/0405087), doi:10.48550/arXiv.astro-ph/0405087

Den Hartog E. A., Lawler J. E., Sobeck J. S., Sneden C., Cowan J. J., 2011, ApJS, 194, 35

Den Hartog E. A., Lawler J. E., Sneden C., Cowan J. J., Roederer I. U., Sobeck J., 2021, ApJS, 255, 27

Fuhr J. R., Wiese W. L., 2006, Journal of Physical and Chemical Reference Data, 35, 1669

Gehren T., Liang Y. C., Shi J. R., Zhang H. W., Zhao G., 2004, A&A, 413, 1045

Grevesse N., Asplund M., Sauval A. J., 2007, Space Sci. Rev., 130, 105

Hannaford P., Lowe R. M., Grevesse N., Biemont E., Whaling W., 1982, ApJ, 261, 736

Hansen C. J., Bergemann M., Cescutti G., François P., Arcones A., Karakas A. I., Lind K., Chiappini C., 2013, A&A, 551, A57

Haywood M., 2008, A&A, 482, 673

Heiter U., et al., 2015, Phys. Scr., 90, 054010

Heiter U., et al., 2021, A&A, 645, A106

Holweger H., 2001, in Wimmer-Schweingruber R. F., ed., American Institute of Physics Conference Series Vol. 598, Joint SOHO/ACE workshop "Solar and Galactic Composition". AIP, pp 23–30 (arXiv:astro-ph/0107426), doi:10.1063/1.1433974

Karathanou K., Kemmler L., Lazaratos M., Siemers M., Bondar A.-N., 2020, Biophysical Journal, 118, 179a

Kelleher D. E., Podobedova L. I., 2008, Journal of Physical and Chemical Reference Data, 37, 1285

Klose J. Z., Fuhr J. R., Wiese W. L., 2002, Journal of Physical and Chemical Reference Data, 31, 217

Kurucz R. L., Furenlid I., Brault J., Testerman L., 1984, Solar flux atlas from 296 to 1300 nm

Lambert D. L., 1978, MNRAS, 182, 249

Lawler J. E., Den Hartog E. A., Sneden C., Cowan J. J., 2006, ApJS, 162, 227

Lawler J. E., Sneden C., Cowan J. J., Ivans I. I., Den Hartog E. A., 2009, ApJS, 182, 51

Lawler J. E., Guzman A., Wood M. P., Sneden C., Cowan J. J., 2013, ApJS, 205, 11

Lawler J. E., Sneden C., Cowan J. J., 2015, ApJS, 220, 13

Lawler J. E., Sneden C., Nave G., Den Hartog E. A., Emrahoğlu N., Cowan J. J., 2017, ApJS, 228, 10

Lawler J. E., Hala Sneden C., Nave G., Wood M. P., Cowan J. J., 2019, ApJS, 241, 21

Lind K., Bergemann M., Asplund M., 2012, Monthly Notices of the Royal Astronomical Society, 427, 50

Lodders K., 2003, ApJ, 591, 1220

Lodders K., Palme H., Gail H. P., 2009, Landolt Börnstein, 4B, 712

Luck R. E., 2017, AJ, 153, 21

Ludwig H.-G., Freytag B., Steffen M., 1999, A&A, 346, 111

Magic Z., Weiss A., Asplund M., 2015, A&A, 573, A89

Marışmak M., Şahin T., Güney F., Plevne O., Bilir S., 2024, Astronomische Nachrichten, 345, e20240047

Mishenina T. V., Soubiran C., Kovtyukh V. V., Korotin S. A., 2004, A&A, 418, 551

Mishenina T. V., Gorbaneva T. I., Basak N. Y., Soubiran C., Kovtyukh V. V., 2011, Astronomy Reports, 55, 689

Mishenina T. V., Pignatari M., Korotin S. A., Soubiran C., Charbonnel C., Thielemann F. K., Gorbaneva T. I., Basak N. Y., 2013, A&A, 552, A128

Molaro P., Monai S., 2012, A&A, 544, A125

Moore C. E., 1954, Science, 119, 449

Moore C. E., Minnaert M. G. J., Houtgast J., 1966, The Solar Spectrum 2935 Å to 8770 Å: Second Revision of Rowland's Preliminary Table of Solar Spectrum Wavelengths. Vol. 61, National Bureau of Standards

Ofman L., Yogesh Giordano S., 2024, ApJ, 970, L16

Pagel B. E. J., Patchett B. E., 1975, MNRAS, 172, 13

Pehlivan Rhodin A., Hartman H., Nilsson H., Jönsson P., 2017, A&A, 598, A102

Petit P., Louge T., Théado S., Paletou F., Manset N., Morin J., Marsden S. C., Jeffers S. V., 2014, PASP, 126, 469

Rice M., Brewer J. M., 2020, ApJ, 898, 119

Ryde N., Edvardsson B., Gustafsson B., Eriksson K., Käufl H. U., Siebenmorgen R., Smette A., 2009, A&A, 496, 701

Şahin T., 2017, Turkish Journal of Physics, 41, 367

Şahin T., Bilir S., 2020, ApJ, 899, 41

Şahin T., Lambert D. L., 2009, MNRAS, 398, 1730

Şahin T., Lambert D. L., Klochkova V. G., Tavolganskaya N. S., 2011, MNRAS, 410, 612

Şahin T., Lambert D. L., Klochkova V. G., Panchuk V. E., 2016, MNRAS, 461, 4071

Şahin T., Marismak M., Cinar N., Bilir S., 2023, Physics and Astronomy Reports, 1, 54

Salmon S. J. A. J., Van Grootel V., Buldgen G., Dupret M. A., Eggenberger P., 2021, A&A, 646, A7

Şentürk S. A., Şahin T., Güney F., Bilir S., Marışmak M., 2024, ApJ, 976, 175

Sharma S., et al., 2018, MNRAS, 473, 2004

Shi J. R., Gehren T., Zhao G., 2011, A&A, 534, A103

Sneden C. A., 1973, PhD thesis, University of Texas, Austin

Takeda Y., 2023, Acta Astron., 73, 35

Takeda Y., Zhao G., Takada-Hidai M., Chen Y.-Q., Saito Y.-J., Zhang H.-W., 2003, Chinese J. Astron. Astrophys., 3, 316

Takeda Y., Kawanomoto S., Honda S., Ando H., Sakurai T., 2007, A&A, 468, 663

Trevisan M., Mamon G. A., Thuan T. X., Ferrari F., Pilyugin L. S., Ranjan A., 2021, MNRAS, 502, 4815

Valenti J. A., Fischer D. A., 2005, ApJS, 159, 141

Wang Y., Zhao G., 2013, ApJ, 769, 4

Woolf V. M., West A. A., 2012, MNRAS, 422, 1489

Zhang W. W., et al., 2019, in O'Dell S. L., Pareschi G., eds, Society of Photo-Optical Instrumentation Engineers (SPIE) Conference Series Vol. 11119, Optics for EUV, X-Ray, and Gamma-Ray Astronomy IX. p. 1111907, doi:10.1117/12.2530284

da Silva R., Milone A. d. C., Rocha-Pinto H. J., 2015, A&A, 580, A24

APPENDIX A: APPENDIX

A1. Literature Review for HD 218209

This section presents a comprehensive literature review of the elemental abundances of the star, focusing on studies conducted over the past four decades. Table A7 summarizes the literature values for each element and compares our results with those of previous studies.

Carbon abundance for star has been reported in the literature over the last decade by da Silva et al. (2015, DA15), Rice & Brewer (2020, RI20), and Takeda (2023, TA23). The carbon abundance ([C/Fe]=0.14 dex) reported in this study is in good agreement with that of Rice & Brewer (2020, RI20) ([C/Fe]=0.18 dex), differing by only 0.04 dex. The largest discrepancy is found for Takeda (2023, TA23), with a difference of 0.22 dex.

The literature values for [O/Fe] exhibited a scatter of approximately 0.3 dex. Our value (≈ 0.3 dex) agrees well with Mishenina et al. (2013, MI13) (Δ = 0.06 dex), but shows a larger discrepancy than Takeda (2023, TA23) (Δ = 0.20 dex) and Rice & Brewer (2020, RI20) (Δ = 0.14 dex).

The [Na/Fe] ratio of -0.03 dex shows good agreement with Mishenina et al. (2011, MI11) ($\Delta = -0.01$ dex), Rice & Brewer (2020, RI20) ($\Delta = -0.06$ dex), Luck (2017, LU17) ($\Delta = -0.09$ dex), and Valenti & Fischer (2005, VA05) ($\Delta = -0.13$ dex). However, a significant discrepancy ($\Delta = -0.26$ dex) was observed compared to in that Gehren et al. (2004, GE04).

Moving on to magnesium, our [Mg/Fe] value of 0.24 dex is consistent with the values reported in Mishenina et al. (2004, MI04), Mishenina et al. (2013, MI13) (Δ = 0.05 dex), da Silva et al. (2015, DA15) (Δ = 0.06 dex), Rice & Brewer (2020, RI20) (Δ = 0.07 dex), and Luck (2017, LU17) ($\Delta = -0.05$ dex). However, a significant discrepancy of -0.17 dex was observed compared to Gehren et al. (2004, GE04).

The reported [Al/Fe] ratio in this study is consistent with the values reported by Mishenina et al. (2011, MI11), da Silva et al. (2015, DA15), Luck (2017, LU17), and Rice & Brewer (2020, RI20), except for the abundance ratio reported by Abia et al. (1988, AB88), which shows a significant discrepancy ($\Delta = -0.32$ dex).

The literature values for [Si/Fe] exhibited a relatively homo-

geneous distribution. Our value of 0.13 dex agrees well with da Silva et al. (2015, DA15) and Luck (2017, LU17) (Δ = 0.02 dex). The largest discrepancy was observed in Takeda et al. (2007, TA07) (Δ = −0.13 dex).

Our [Ca/Fe] value of 0.15 dex is in good agreement with Rice & Brewer (2020, RI20) (Δ = 0.03 dex), da Silva et al. (2015, DA15) (Δ = 0.02 dex), and Luck (2017, LU17) (Δ = −0.04 dex). A significant discrepancy is observed with Mishenina et al. (2011, MI11) (Δ = 0.50 dex).

Our [Sc/Fe] value of 0.06 dex shows a discrepancy of 0.09 dex compared to Luck (2017, LU17).

Our [Ti/Fe] value of 0.21 dex agrees well with Luck (2017, LU17) and shows good agreement with da Silva et al. (2015, DA15) (Δ = 0.01 dex), Valenti & Fischer (2005, VA05) (Δ = −0.02 dex), and Rice & Brewer (2020, RI20) (Δ = −0.03 dex). A significant discrepancy is observed with Takeda et al. (2007, TA07) (Δ = 0.18 dex).

Our [V/Fe] value of -0.02 dex aligns well with the findings of Takeda et al. (2007, TA07) (Δ = 0.05 dex) but shows discrepancies of 0.19 dex, 0.18 dex, and 0.15 dex when compared to Rice & Brewer (2020, RI20), Luck (2017, LU17), and da Silva et al. (2015, DA15), respectively.

The [Cr/Fe] value determined in this study agrees well with previous findings, with discrepancies of approximately ±0.05 dex observed when compared to Rice & Brewer (2020, RI20) and Luck (2017, LU17).

Our [Mn/Fe] value of -0.27 dex precisely matches the value reported by Rice & Brewer (2020, RI20) and demonstrates good agreement with da Silva et al. (2015, DA15) (Δ = −0.09 dex) and Luck (2017, LU17) (Δ = −0.03 dex).

The [Co/Fe] value determined in this study exhibits discrepancies of -0.18 dex compared to Luck (2017, LU17) and -0.23 dex compared to Takeda et al. (2007, TA07).

The [Ni/Fe] value determined in this study aligns well with the literature values, with the exception of a significant discrepancy (Δ = −0.21 dex) observed in the work of Abia et al. (1988, AB88). The smallest discrepancy is found with Luck (2017, LU17) (Δ = −0.01 dex), followed by Rice & Brewer (2020, RI20) (Δ = −0.03 dex), Mishenina et al. (2013, MI13) and Mishenina et al. (2004, MI04) (Δ = −0.06 dex), and Takeda et al. (2007, TA07) (Δ = −0.02 dex).

The [Cu/Fe] value determined in this study shows discrepancies of -0.10 dex compared to Luck (2017, LU17), -0.06 dex compared to da Silva et al. (2015, DA15), and -0.11 dex compared to Mishenina et al. (2011, MI11).

The [Zn/Fe] value determined in this study is in good agreement with literature values, with a difference of 0.08 dex compared to Luck (2017, LU17) and 0.06 dex compared to Mishenina et al. (2013, MI13).

The [Sr/Fe] value of 0.10 dex determined in this study exhibits a discrepancy of -0.28 dex compared to Luck (2017, LU17).

The [Y/Fe] value determined in this study shows discrepancies of -0.16 dex compared to Rice & Brewer (2020, RI20), -0.22 dex compared to Luck (2017, LU17), and -0.10 dex compared to Mishenina et al. (2011, MI11).

The [Zr/Fe] value determined in this study agrees well with Mishenina et al. (2013, MI13) (Δ = 0.04 dex), but shows a discrepancy of -0.21 dex compared to Luck (2017, LU17).

The [Ba/Fe] value determined in this study precisely matches that reported by Luck (2017, LU17) ([Ba/Fe]=0.04 dex), while a difference of 0.03 dex is observed compared to Mishenina et al. (2013, MI13).

The [La/Fe] value determined in this study shows a discrepancy of -0.60 dex compared to Luck (2017, LU17), while a difference of -0.06 dex is observed compared to Mishenina et al. (2013, MI13).

The [Ce/Fe] value determined in this study shows a discrepancy of -0.02 dex compared to Luck (2017, LU17), while a difference of -0.28 dex is observed compared to Mishenina et al. (2013, MI13).

The difference in neodymium abundance compared to Luck (2017, LU17) is -0.24 dex, while the difference compared to Mishenina et al. (2013, MI13) is -0.07 dex.

The [Sm/Fe] value determined in this study shows a discrepancy of -0.12 dex compared to Luck (2017, LU17), while a difference of 0.01 dex is observed compared to Mishenina et al. (2013, MI13).

Table A1. Fe I and Fe II lines. The abundances were obtained for a model with $T_{\rm eff}$ = 5770 K, log g = 4.40 cgs, and ξ = 0.66 km s^{-1} for the solar spectrum. $T_{\rm eff}$ =5600 K, log g = 4.50 cgs, and ξ = 0.44 km s^{-1} for the HD 218209 spectrum.

				Sun		HD 218209								Sun		HD 218209				
Spec.	λ	LEP	log(gf)	EW	log ϵ(X)	EW	log ϵ(X)	RMT	Ref.	Spec.	λ	LEP	log(gf)	EW	log ϵ(X)	EW	log ϵ(X)	RMT	Ref.
	(Å)	(eV)	(dex)	(mÅ)	(dex)	(mÅ)	(dex)				(Å)	(eV)	(dex)	(mÅ)	(dex)	(mÅ)	(dex)		
Fe I	4080.22	3.28	-1.23	80.9	7.32	-	-	558	1	Fe I	5501.48	0.96	-3.05	115.3	7.50	104.5	7.08	15	1
Fe I	4082.11	3.42	-1.51	68.2	7.49	-	-	698	1	Fe I	5506.79	0.99	-2.80	123.2	7.37	111.4	6.94	15	1
Fe I	4088.56	3.64	-1.50	52.3	7.41	-	-	906	1	Fe I	5525.55	4.23	-1.08	53.0	7.35	39.4	6.96	1062	1
Fe I	4090.96	3.37	-1.73	55.8	7.37	-	-	695	1	Fe I	5543.94	4.22	-1.11	61.5	7.55	49.1	7.17	1062	1
Fe I	4204.00	2.84	-1.01	125.1	7.50	-	-	355	1	Fe I	5546.51	4.37	-1.28	50.8	7.63	35.9	7.21	1145	1
Fe I	4207.13	2.83	-1.41	82.5	7.39	77.3	7.12	352	1	Fe I	5560.22	4.43	-1.16	50.2	7.55	36.4	7.15	1164	1
Fe I	4220.35	3.07	-1.31	83.6	7.46	77.4	7.16	482	1	Fe I	5618.64	4.21	-1.28	50.0	7.47	36.1	7.06	1107	1
Fe I	4365.90	2.99	-2.25	51.4	7.48	40.7	7.09	415	1	Fe I	5624.03	4.39	-1.20	50.4	7.56	37.2	7.18	1160	1
Fe I	4432.58	3.57	-1.56	51.9	7.37	42.9	7.04	797	1	Fe I	5633.95	4.99	-0.32	65.3	7.57	53.3	7.23	1314	1
Fe I	4439.89	2.28	-3.00	52.1	7.56	36.7	7.03	116	1	Fe I	5636.71	3.64	-2.56	20.7	7.53	13.6	7.18	868	1
Fe I	4442.35	2.20	-1.25	187.7	7.52	-	-	68	1	Fe I	5638.27	4.22	-0.84	76.6	7.53	67.7	7.23	1087	1
Fe I	4447.14	2.20	-2.73	66.6	7.64	57.3	7.27	69	1	Fe I	5641.45	4.26	-1.15	66.7	7.70	49.0	7.24	1087	1
Fe I	4447.73	2.22	-1.34	171.0	7.52	-	-	68	1	Fe I	5662.52	4.18	-0.57	91.2	7.57	81.4	7.25	1087	1
Fe I	4502.60	3.57	-2.31	28.6	7.50	-	-	796	1	Fe I	5701.56	2.56	-2.22	84.8	7.61	72.7	7.21	209	1
Fe I	4556.93	3.25	-2.66	26.8	7.49	-	-	638	1	Fe I	5705.47	4.30	-1.36	37.8	7.37	25.4	6.98	1087	1
Fe I	4593.53	3.94	-2.03	28.3	7.53	-	-	971	1	Fe I	5717.84	4.28	-1.10	62.1	7.58	-	-	1107	1
Fe I	4602.01	1.61	-3.15	70.9	7.53	63.9	7.20	39	1	Fe I	5741.86	4.26	-1.67	32.6	7.52	-	-	1086	1
Fe I	4602.95	1.48	-2.22	118.8	7.44	110.7	7.06	39	1	Fe I	5778.46	2.59	-3.43	22.4	7.42	15.5	7.06	209	1
Fe I	4619.30	3.60	-1.08	83.9	7.43	68.9	6.98	821	1	Fe I	5806.73	4.61	-1.03	51.6	7.58	41.9	7.28	1180	1
Fe I	4630.13	2.28	-2.59	73.2	7.62	66.5	7.29	115	1	Fe I	5814.80	4.26	-1.94	22.0	7.53	12.2	7.10	1086	1
Fe I	4635.85	2.84	-2.36	54.1	7.50	42.5	7.08	349	1	Fe I	5881.28	4.59	-1.70	14.3	7.35	-	-	1178	1
Fe I	4661.54	4.54	-1.26	37.9	7.54	25.1	7.14	1207	1	Fe I	5905.67	4.63	-0.77	57.0	7.44	-	-	1181	1
Fe I	4678.85	3.60	-0.83	syn	7.54	syn	7.06	821	1	Fe I	5916.26	2.45	-2.99	54.4	7.60	45.2	7.26	170	1
Fe I	4704.95	3.69	-1.53	62.7	7.56	53.5	7.22	821	1	Fe I	5929.68	4.55	-1.38	39.5	7.65	24.8	7.21	1176	1
Fe I	4728.55	3.65	-1.17	81.3	7.63	-	-	822	1	Fe I	5934.67	3.93	-1.12	76.0	7.44	59.8	7.01	982	1
Fe I	4733.60	1.48	-2.99	83.9	7.58	77.8	7.26	38	1	Fe I	5952.73	3.98	-1.39	59.6	7.48	-	-	959	1
Fe I	4735.85	4.07	-1.32	64.1	7.77	-	-	1042	1	Fe I	5956.71	0.86	-4.61	50.9	7.55	44.4	7.23	14	1
Fe I	4741.53	2.83	-1.76	71.3	7.36	66.0	7.11	346	1	Fe I	5983.70	4.53	-0.49	67.1	7.35	57.5	7.04	1175	3
Fe I	4745.81	3.65	-1.27	73.9	7.59	68.3	7.32	821	1	Fe I	6003.03	3.86	-1.03	81.3	7.38	72.4	7.06	959	2
Fe I	4779.44	3.40	-2.02	40.7	7.34	-	-	720	1	Fe I	6005.53	2.58	-3.60	21.8	7.56	15.8	7.23	959	3
Fe I	4788.77	3.24	-1.76	65.4	7.58	-	-	588	1	Fe I	6027.06	4.07	-1.09	63.5	7.47	-	-	1018	1
Fe I	4793.96	3.03	-3.47	8.7	7.43	-	-	512	1	Fe I	6065.49	2.61	-1.53	117.0	7.41	-	-	207	1
Fe I	4794.36	2.41	-4.05	11.5	7.55	-	-	115	2	Fe I	6078.50	4.77	-0.32	75.9	7.53	62.3	7.16	1259	3
Fe I	4802.89	3.64	-1.51	59.7	7.49	47.6	7.10	888	1	Fe I	6079.02	4.65	-1.10	44.4	7.55	28.9	7.12	1176	1
Fe I	4839.55	3.27	-1.82	61.8	7.57	55.8	7.32	588	1	Fe I	6082.72	2.22	-3.57	34.3	7.48	24.1	7.08	64	1
Fe I	4875.88	3.33	-1.97	61.0	7.58	-	-	687	1	Fe I	6096.67	3.98	-1.88	36.9	7.53	24	7.12	959	1
Fe I	4917.23	4.19	-1.16	62.8	7.60	51.9	7.25	1066	1	Fe I	6127.91	4.14	-1.40	47.5	7.49	36.8	7.15	1017	1
Fe I	4918.02	4.23	-1.34	52.0	7.60	40.0	7.23	1070	1	Fe I	6137.70	2.59	-1.40	129.4	7.40	114.3	6.98	207	1
Fe I	4924.78	2.28	-2.11	92.6	7.50	85.5	7.16	114	1	Fe I	6157.73	4.07	-1.22	61.5	7.55	48.8	7.17	1015	1
Fe I	4939.69	0.86	-3.34	98.4	7.53	-	-	16	1	Fe I	6165.36	4.14	-1.47	43.9	7.48	30.5	7.07	1018	1
Fe I	4961.92	3.63	-2.25	26.2	7.40	-	-	845	1	Fe I	6173.34	2.22	-2.88	67.7	7.57	56.9	7.18	62	1
Fe I	4962.58	4.18	-1.18	53.2	7.48	37.8	7.03	66	1	Fe I	6180.21	2.73	-2.65	53.3	7.50	-	-	269	1
Fe I	4973.10	3.96	-0.92	87.3	7.61	-	-	173	1	Fe I	6200.32	2.61	-2.44	72.2	7.58	-	-	207	1
Fe I	5022.24	3.98	-0.56	97.1	7.40	-	-	965	1	Fe I	6213.44	2.22	-2.48	81.0	7.45	-	-	62	1
Fe I	5029.62	3.41	-2.00	48.6	7.52	-		718	1	Fe I	6219.29	2.20	-2.43	89.5	7.55	-	-	62	1
Fe I	5044.22	2.84	-2.02	71.9	7.39	64.7	7.06	318	1	Fe I	6232.65	3.65	-1.22	81.0	7.58	73.6	7.29	816	1
Fe I	5074.75	4.22	-0.23	113.7	7.43	97.1	7.02	1094	1	Fe I	6240.65	2.22	-3.17	47.6	7.38	38.7	7.03	64	1
Fe I	5083.35	0.96	-2.96	109.7	7.40	-	-	16	1	Fe I	6246.33	3.59	-0.88	111.4	7.36	106.6	7.07	816	1
Fe I	5088.16	4.15	-1.75	37.0	7.63	-	-	1066	1	Fe I	6252.56	2.40	-1.69	119.2	7.40	106.8	7.00	169	1
Fe I	5141.75	2.42	-2.24	86.1	7.61	75.6	7.21	114	1	Fe I	6265.14	2.18	-2.55	84.0	7.54	76.5	7.22	62	1
Fe I	5145.10	2.20	-3.08	53.8	7.50	42.4	7.09	66	1	Fe I	6270.23	2.86	-2.61	51.0	7.52	42.0	7.19	342	1
Fe I	5198.72	2.22	-2.13	95.1	7.46	-	-	66	1	Fe I	6297.80	2.22	-2.74	74.4	7.56	65.5	7.22	62	1
Fe I	5217.40	3.21	-1.16	108.7	7.37	-	-	66	1	Fe I	6301.51	3.65	-0.72	113.9	7.57	106.4	7.27	816	1
Fe I	5225.53	0.11	-4.79	73.7	7.63	-	-	1	1	Fe I	6315.81	4.07	-1.66	40.3	7.51	24.6	7.03	1014	1
Fe I	5228.38	4.22	-1.26	syn	7.79	syn	7.18	1091	1	Fe I	6322.69	2.59	-2.43	75.3	7.60	64.3	7.22	207	1
Fe I	5242.50	3.63	-0.97	85.3	7.48	75.2	7.13	843	1	Fe I	6330.86	4.71	-0.97	33.2	7.23	21.1	6.85	1254	1
Fe I	5243.78	4.26	-1.12	61.1	7.59	49	7.22	1089	1	Fe I	6335.34	2.20	-2.18	97.0	7.42	85.9	7.03	62	1
Fe I	5247.06	0.09	-4.95	68.1	7.63	57.5	7.19	1	1	Fe I	6336.83	3.69	-0.86	102.2	7.32	93.9	6.99	816	1
Fe I	5250.22	0.12	-4.94	68.2	7.65	60.5	7.29	66	1	Fe I	6344.15	2.43	-2.92	50.2	7.38	-	-	169	1
Fe I	5250.65	2.20	-2.18	101.5	7.59	92.4	7.22	66	1	Fe I	6392.53	2.27	-4.03	17.1	7.51	-	-	109	3
Fe I	5253.47	3.28	-1.57	75.4	7.36	66.9	7.02	553	1	Fe I	6393.61	2.43	-1.58	130.4	7.42	-	-	168	1
Fe I	5288.53	3.69	-1.51	57.3	7.47	44.8	7.07	929	1	Fe I	6408.03	3.69	-1.02	syn	7.65	syn	7.23	816	1
Fe I	5298.78	3.64	-2.02	42.2	7.55	-	-	875	1	Fe I	6419.96	4.73	-0.27	80.5	7.41	70.2	7.10	1258	1
Fe I	5307.37	1.61	-2.99	86.0	7.58	76.2	7.19	36	1	Fe I	6430.86	2.18	-2.01	109.5	7.41	101.8	7.08	62	1
Fe I	5322.05	2.28	-2.80	60.3	7.44	-	-	112	1	Fe I	6469.19	4.83	-0.81	55.0	7.61	40.5	7.22	1258	1
Fe I	5365.41	3.57	-1.22	76.9	7.49	69.8	7.2	786	1	Fe I	6481.88	2.28	-2.98	63.7	7.59	55.0	7.26	109	1
Fe I	5373.71	4.47	-0.84	61.6	7.47	48.1	7.09	1166	1	Fe I	6498.94	0.96	-4.69	44.7	7.54	37.9	7.22	13	1
Fe I	5379.58	3.69	-1.51	60.8	7.54	44.3	7.04	928	1	Fe I	6518.37	2.83	-2.46	56.0	7.44	49.1	7.16	342	1
Fe I	5398.29	4.44	-0.71	72.5	7.51	59.4	7.13	553	1	Fe I	6593.88	2.43	-2.42	85.0	7.61	79.0	7.32	168	1
Fe I	5461.54	4.43	-1.88	26.0	7.74	-	-	1145	1	Fe I	6609.12	2.56	-2.69	64.2	7.57	54.9	7.23	206	1
Fe I	5473.91	4.15	-0.79	76.9	7.45	-	-	1062	1	Fe I	6678.00	2.69	-1.42	122.8	7.41	111.7	7.04	268	1
Fe I	5483.11	4.15	-1.41	46.5	7.47	-	-	1061	1	Fe I	6703.58	2.76	-3.06	36.6	7.52	26.9	7.16	268	1
Fe I	5487.15	4.41	-1.51	35.6	7.57	24.4	7.21	1143	1	Fe I	6750.16	2.42	-2.62	73.1	7.54	-	-	111	1

Table A2. Fe I and Fe II lines. The abundances were obtained for a model with $T_{\rm eff}$ = 5770 K, log g = 4.40 cgs, and ξ =0.66 km s^{-1} for the solar spectrum. $T_{\rm eff}$ = 5600 K, log g = 4.50 cgs, and ξ = 0.44 km s^{-1} for the HD 218209 spectrum.

				Sun		HD 218209								Sun		HD 218209				
Spec.	λ	LEP	log(gf)	EW	log ϵ(X)	EW	log ϵ(X)	RMT	Ref.	Spec.	λ	LEP	log(gf)	EW	log ϵ(X)	EW	log ϵ(X)	RMT	Ref.
	(Å)	(eV)	(dex)	(mÅ)	(dex)	(mÅ)	(dex)				(Å)	(eV)	(dex)	(mÅ)	(dex)	(mÅ)	(dex)		
Fe I	6806.85	2.72	-3.21	34.0	7.57	25.2	7.22	268	1	Fe I	8526.68	4.89	-0.76	58.3	7.62	-	-	1270	1
Fe I	6810.28	4.59	-0.99	48.7	7.44	38.1	7.12	1197	1	Fe I	8582.27	2.98	-2.13	77.6	7.57	63.0	7.16	401	1
Fe I	6820.43	4.62	-1.29	39.7	7.63	24.6	7.18	1197	2	Fe I	8611.81	2.83	-1.85	98.5	7.41	83.9	7.02	339	1
Fe I	6862.48	4.54	-1.57	29.3	7.57	20.2	7.24	1191	3	Fe I	8613.93	4.97	-1.25	31.5	7.63	-	-	1272	3
Fe I	6898.31	4.20	-2.23	16.6	7.55	-	-	1078	3	Fe I	8616.27	4.89	-0.71	43.4	7.27	-	-	1266	3
Fe I	6916.70	4.14	-1.40	57.1	7.55	45.4	7.20	1052	1	Fe I	8699.43	4.93	-0.38	65.7	7.40	-	-	1267	1
Fe I	6977.44	4.57	-1.56	19.9	7.35	-	-	1225	3	Fe I	8757.19	2.83	-1.92	92.7	7.39	82.9	7.06	339	1
Fe I	6999.90	4.09	-1.51	54.0	7.56	43.4	7.23	1051	2	Fe I	8793.38	4.59	-0.09	107.9	7.45	98.3	7.16	1172	3
Fe I	7016.07	2.41	-3.21	50.8	7.62	-	-	109	3	Fe I	8796.42	4.93	-1.23	27.3	7.46	-	-	1266	3
Fe I	7022.98	4.17	-1.20	63.5	7.48	50.6	7.11	1051	1	Fe I	8798.05	4.96	-1.89	8.0	7.47	-	-	1286	3
Fe I	7038.25	4.20	-1.25	60.0	7.49	-	-	1051	1	Fe I	8834.04	4.20	-2.59	8.0	7.44	-	-	1050	3
Fe I	7071.88	4.59	-1.70	26.5	7.67	18.6	7.37	1194	3	Fe I	8838.43	2.85	-1.87	97.5	7.42	83.9	7.04	339	1
Fe I	7090.40	4.21	-1.16	64.5	7.49	50.0	7.10	1051	1	Fe I	8846.82	4.99	-0.78	48.5	7.52	39.3	7.26	1267	3
Fe I	7130.94	4.20	-0.80	87.3	7.46	73.0	7.08	1051	1	Fe I	8878.26	2.98	-3.83	11.7	7.67	-	-	401	3
Fe I	7132.99	4.06	-1.63	41.6	7.47	31.3	7.13	1002	1	Fe I	8887.10	4.93	-1.94	4.8	7.25	-	-	1265	3
Fe I	7180.02	1.48	-4.78	20.0	7.52	-	-	1	3	Fe I	8902.94	4.97	-2.11	8.6	7.73	-	-	1266	3
Fe I	7212.47	4.93	-0.83	30.4	7.23	-	-	1273	3	Fe I	8922.66	4.97	-1.70	12.9	7.53	-	-	1298	3
Fe I	7219.69	4.07	-1.69	45.0	7.61	35.6	7.30	1001	3	Fe I	8945.20	5.01	-0.22	72.2	7.40	49.6	6.91	1301	3
Fe I	7221.22	4.54	-1.18	40.5	7.44	26.1	7.02	1189	3	Fe I	8950.20	4.14	-2.43	13.1	7.46	-	-	1050	3
Fe I	7222.88	4.59	-2.04	15.2	7.68	-	-	1187	3	Fe I	8959.88	5.00	-1.84	8.9	7.50	-	-	1320	3
Fe I	7228.70	2.75	-3.38	27.2	7.58	23.7	7.36	2	3	Fe I	8975.41	2.98	-2.22	77.3	7.60	-	-	400	1
Fe I	7284.84	4.12	-1.57	41.6	7.46	27.8	7.04	1004	3	Fe I	8984.87	5.08	-0.92	32.5	7.40	-	-	1301	3
Fe I	7306.61	4.16	-1.44	42.0	7.37	30.3	7.00	1077	3	Fe I	9010.55	2.60	-2.95	44.1	7.27	35.2	6.95	202	1
Fe I	7351.16	4.97	-0.84	36.2	7.40	23.0	7.00	1275	3	Fe I	9030.67	2.83	-3.64	25.5	7.77	-	-	338	1
Fe I	7351.56	4.93	-0.64	45.5	7.36	34.3	7.04	1275	3	Fe I	9070.42	4.20	-2.05	33.7	7.71	-	-	1076	3
Fe I	7396.50	4.97	-1.64	12.6	7.53	-	-	1278	3	Fe I	9079.60	4.63	-0.81	54.1	7.31	-	-	1172	3
Fe I	7401.69	4.17	-1.35	40.9	7.26	-	-	1004	2	Fe I	9089.41	2.94	-1.68	99.8	7.41	88.9	7.09	400	1
Fe I	7411.18	4.26	-0.30	101.9	7.43	-	-	4	3	Fe I	9117.10	2.85	-3.46	32.3	7.76	-	-	338	3
Fe I	7418.67	4.12	-1.38	48.7	7.41	-	-	4	1	Fe I	9156.23	3.00	-3.67	9.3	7.40	-	-	400	3
Fe I	7443.03	4.17	-1.82	34.7	7.59	28.0	7.33	1309	1	Fe I	9210.03	2.83	-2.40	65.0	7.37	-	-	83	2
Fe I	7447.43	4.93	-0.85	34.1	7.32	24.8	7.02	1273	3	Fe I	9382.93	4.96	-1.59	24.3	7.74	-	-	1284	3
Fe I	7454.02	4.17	-2.41	12.0	7.51	-	-	5	3	Fe I	9602.07	4.99	-1.74	15.4	7.64	-	-	1283	3
Fe I	7473.56	4.59	-1.87	18.2	7.60	-	-	1188	3	Fe I	9653.14	4.71	-0.68	68.4	7.46	-	-	1247	3
Fe I	7491.68	4.28	-0.90	64.9	7.42	53.1	7.08	1077	3	Fe I	9753.13	4.77	-0.78	56.9	7.40	-	-	1247	3
Fe I	7498.56	4.12	-2.25	18.0	7.52	13.5	7.27	1001	3	Fe I	9786.62	4.59	-1.68	18.5	7.28	-	-	1171	3
Fe I	7511.05	4.16	0.09	151.6	7.46	141.1	7.14	1077	1	Fe I	9800.34	5.06	-0.45	59.7	7.38	-	-	1292	3
Fe I	7540.44	2.72	-3.85	11.5	7.51	-	-	266	3	Fe I	9861.79	5.04	-0.14	73.8	7.28	-	-	1296	1
Fe I	7551.10	5.06	-1.63	11.0	7.53	-	-	1303	3	Fe I	9881.51	4.56	-1.71	18.1	7.26	-	-	1209	3
Fe I	7568.93	4.26	-0.77	74.3	7.45	64.4	7.15	1077	3	Fe I	9889.08	5.01	-0.45	75.4	7.59	-	-	1296	1
Fe I	7583.80	3.00	-1.89	82.3	7.46	69.1	7.07	402	1	Fe I	9944.13	4.99	-1.34	30.8	7.63	-	-	1285	3
Fe I	7586.04	4.29	-0.47	112.3	7.74	106	7.48	1137	3	Fe II	4178.86	2.58	-2.51	83.8	7.38	67.3	6.99	28	1
Fe I	7620.54	4.71	-0.66	55.4	7.38	-	-	1250	3	Fe II	4491.40	2.84	-2.64	74.8	7.50	-	-	37	1
Fe I	7653.78	4.77	-0.89	34.4	7.21	-	-	1250	1	Fe II	4508.29	2.85	-2.44	85.5	7.52	73.7	7.26	38	1
Fe I	7710.39	4.20	-1.11	64.9	7.54	61.0	7.36	1077	1	Fe II	4576.34	2.84	-2.92	63.8	7.48	-	-	38	1
Fe I	7719.05	5.01	-1.15	28.3	7.55	19.2	7.23	1304	3	Fe II	4582.83	2.84	-3.06	55.9	7.40	-	-	37	1
Fe I	7723.20	2.27	-3.62	42.2	7.65	-	-	108	2	Fe II	4620.52	2.83	-3.19	52.0	7.41	37.1	7.03	38	1
Fe I	7745.48	5.06	-1.17	21.7	7.44	-	-	1305	3	Fe II	4993.36	2.79	-3.68	37.7	7.46	-	-	36	1
Fe I	7748.28	2.94	-1.75	100.6	7.54	91.9	7.22	402	1	Fe II	5132.67	2.81	-4.09	25.1	7.53	14.6	7.20	35	1
Fe I	7780.59	4.45	0.03	114.7	7.39	103.4	7.07	1154	3	Fe II	5197.58	3.23	-2.22	79.8	7.47	-	-	49	1
Fe I	7832.22	4.42	0.11	118.0	7.31	112.0	7.06	1154	3	Fe II	5234.63	3.22	-2.21	82.1	7.49	67.7	7.19	49	1
Fe I	7844.55	4.81	-1.70	12.8	7.43	-	-	1250	3	Fe II	5264.81	3.33	-3.13	45.8	7.63	33.9	7.35	48	1
Fe I	7879.75	5.01	-1.47	10.2	7.27	-	-	1306	3	Fe II	5284.11	2.89	-3.11	syn	7.5	syn	6.98	41	1
Fe I	7912.87	0.86	-4.84	48.3	7.56	36.0	7.12	12	1	Fe II	5325.56	3.21	-3.26	42.5	7.56	-	-	49	1
Fe I	7941.09	3.26	-2.29	41.7	7.28	-	-	623	1	Fe II	5414.07	3.22	-3.58	28.2	7.49	15.7	7.12	48	1
Fe I	7998.97	4.35	0.15	129.7	7.33	-	-	1136	3	Fe II	5425.26	3.20	-3.22	41.8	7.48	26.5	7.09	49	1
Fe I	8028.34	4.45	-0.69	68.2	7.39	64.0	7.20	1154	3	Fe II	5534.85	3.23	-2.75	57.4	7.46	39.3	7.02	55	1
Fe I	8047.60	0.86	-4.79	60.4	7.77	-	-	12	3	Fe II	6084.11	3.19	-3.88	20.3	7.52	8.9	7.07	46	1
Fe I	8096.87	4.06	-1.78	35.1	7.41	-	-	999	1	Fe II	6149.24	3.87	-2.84	35.9	7.57	23.2	7.25	74	1
Fe I	8204.10	0.91	-6.05	5.8	7.52	-	-	12	3	Fe II	6238.38	3.87	-2.75	42.1	7.64	-	-	74	1
Fe I	8207.77	4.43	-0.86	65.4	7.48	47.4	7.02	1136	3	Fe II	6247.56	3.89	-2.30	52.0	7.46	38.2	7.16	74	1
Fe I	8239.13	2.41	-3.18	44.9	7.38	36.4	7.07	108	3	Fe II	6432.68	2.89	-3.57	40.3	7.47	24.8	7.07	40	1
Fe I	8248.15	4.35	-0.89	60.5	7.32	50.7	7.03	1136	3	Fe II	6456.39	3.90	-2.05	62.1	7.45	46.6	7.12	74	1
Fe I	8293.53	3.30	-2.14	57.6	7.50	46.8	7.17	623	1	Fe II	6516.08	2.89	-3.31	53.4	7.53	40.0	7.22	40	1
Fe I	8360.82	4.45	-1.29	57.2	7.74	45.3	7.41	1153	3	Fe II	7222.39	3.87	-3.40	18.9	7.60	-	-	73	1
Fe I	8365.64	3.24	-1.91	69.0	7.45	55.4	7.06	623	1	Fe II	7224.51	3.87	-3.36	19.4	7.58	-	-	73	1
Fe I	8424.14	4.93	-1.16	33.4	7.56	20.7	7.17	1272	3	Fe II	7515.88	3.89	-3.39	13.1	7.38	-	-	73	1
Fe I	8439.60	4.53	-0.59	73.2	7.41	61.6	7.09	1172	3	Fe II	7533.42	3.89	-3.60	17.7	7.77	-	-	72	3
Fe I	8514.08	2.19	-2.23	116.1	7.46	102.4	7.07	60	1	Fe II	7655.47	3.87	-3.77	7.1	7.41	-	-	73	3
Fe I	8515.08	3.00	-2.07	83.0	7.64	71.4	7.30	401	2	Fe II	7711.71	3.89	-2.45	44.7	7.36	30.4	7.04	73	1

Table A3. The abundances were obtained for a model with $T_{\rm eff}$ = 5770 K, $\log g$ = 4.40 cgs, and ξ = 0.66 km s^{-1} for the solar spectrum. $T_{\rm eff}$ = 5600 K, $\log g$ = 4.50 cgs, and ξ = 0.44 km s^{-1} for the HD 218209 spectrum.

Spec.	λ	LEP	$\log(gf)$	Sun EW	Sun $\log\epsilon$(X)	HD 218209 EW	HD 218209 $\log\epsilon$(X)	RMT	Ref.	Spec.	λ	LEP	$\log(gf)$	Sun EW	Sun $\log\epsilon$(X)	HD 218209 EW	HD 218209 $\log\epsilon$(X)	RMT	Ref.
	(Å)	(eV)	(dex)	(mÅ)	(dex)	(mÅ)	(dex)				(Å)	(eV)	(dex)	(mÅ)	(dex)	(mÅ)	(dex)		
C I	8335.19	7.65	-0.44	syn	8.41	syn	8.16	10	2	Sc II	5526.82	1.77	-0.01	75.3	3.32	68.0	3.13	18	9
C I	9111.85	7.46	-0.34	syn	8.56	syn	8.34	3	4	Sc II	5640.99	1.5	-0.99	syn	3.12	syn	2.84	29	9
O I	7771.96	9.11	0.37	syn	8.83	syn	8.73	1	2	Sc II	5657.88	1.51	-0.54	67.1	3.39	57.4	3.14	29	9
O I	7774.18	9.11	0.22	syn	8.83	syn	8.74	1	2	Sc II	5667.15	1.50	-1.21	32.8	3.24	26.5	3.04	29	9
O I	7775.40	9.11	0.00	syn	8.77	syn	8.69	1	2	Sc II	5669.04	1.50	-1.10	34.2	3.16	28.1	2.97	29	9
Na I	5682.65	2.1	-0.7	syn	6.36	syn	5.87	6	2	Sc II	6245.63	1.50	-1.02	34.0	3.05	30.4	2.92	28	2
Na I	5688.22	2.10	-0.37	122.1	6.11	101.1	5.73	6	4	Sc II	6279.76	1.49	-1.33	28.6	3.22	21.0	2.97	28	3
Na I	6154.23	2.09	-1.55	36.9	6.27	22.9	5.89	5	2	Sc II	6300.70	1.50	-1.90	7.1	3.02	–	–	28	3
Na I	8183.26	2.09	0.22	201.9	6.13	183.1	5.79	4	3	Sc II	6320.85	1.49	-1.82	9.0	3.05	–	–	28	3
Mg I	4571.10	0.00	-5.40	syn	7.57	syn	7.58	1	5	Sc II	6604.60	1.35	-1.31	35.3	3.21	30.9	3.06	19	2
Mg I	5711.10	4.34	-1.74	syn	7.63	syn	7.55	8	5	Ti I	4060.27	1.05	-0.69	syn	4.85	syn	4.51	80	10
Mg I	7657.60	5.09	-1.27	syn	7.64	syn	7.45	22	2	Ti I	4186.13	1.5	-0.24	syn	4.89	syn	4.67	129	10
Mg I	7691.57	5.73	-0.78	syn	7.65	syn	7.40	29	2	Ti I	4287.41	0.84	-0.37	68.6	5.02	73.2	4.94	44	10
Mg I	8213.02	5.73	-0.51	syn	7.60	syn	7.47	28	2	Ti I	4453.32	1.43	-0.03	66.6	5.19	64.7	5.00	113	10
Mg II	7896.37	9.96	0.64	syn	7.63	syn	–	8	2	Ti I	4465.81	1.74	-0.13	39.2	4.89	33.9	4.62	146	10
Al I	6695.97	3.13	-1.57	syn	6.48	syn	6.17	5	2	Ti I	4512.74	0.84	-0.40	66.8	4.96	65.8	4.76	42	10
Al I	6698.63	3.13	-1.87	syn	6.44	syn	6.07	5	2	Ti I	4518.03	0.83	-0.25	73.5	4.96	74.6	4.80	42	10
Al I	7362.31	4.00	-0.79	syn	6.38	syn	6.17	11	6	Ti I	4534.79	0.84	0.35	96.4	4.84	100.8	4.65	42	10
Al I	7835.33	4.00	-0.69	syn	6.45	syn	6.19	10	6	Ti I	4548.77	0.83	-0.28	71.5	4.94	76.3	4.86	270	10
Al I	7836.15	4.00	-0.50	syn	6.46	syn	6.19	10	6	Ti I	4555.49	0.85	-0.40	64.1	4.89	66.3	4.78	266	10
Al I	8772.88	4.00	-0.35	syn	6.43	syn	6.28	9	6	Ti I	4617.28	1.75	0.44	62.6	4.89	60.5	4.70	145	10
Al I	8773.91	4.00	-0.16	syn	6.43	syn	6.28	9	6	Ti I	4623.1	1.74	0.16	syn	4.95	syn	4.58	145	10
Al I	8841.26	4.07	-1.50	syn	6.42	syn	6.16	15	2	Ti I	4639.36	1.74	-0.05	syn	4.94	syn	4.58	145	10
Si I	5645.62	4.93	-2.03	35.0	7.49	25.1	7.23	10	7	Ti I	4639.66	1.75	-0.14	syn	5	syn	4.59	145	10
Si I	5665.56	4.92	-1.99	39.7	7.53	28.6	7.25	10	7	Ti I	4656.47	0.00	-1.28	71.3	5.11	71.4	4.94	6	10
Si I	5684.49	4.95	-1.58	60.1	7.51	46.3	7.21	11	7	Ti I	4722.61	1.05	-1.47	19.3	5.03	–	–	75	10
Si I	5701.14	4.91	-2.05	38.5	7.55	28.8	7.31	10	2	Ti I	4742.80	2.24	0.21	31.2	4.82	31.4	4.70	233	10
Si I	5708.40	4.95	-1.47	72.1	7.59	60.1	7.33	10	2	Ti I	4758.12	2.25	0.51	42.9	4.81	45.1	4.74	233	10
Si I	5772.15	5.08	-1.62	51.1	7.51	40.7	7.27	17	7	Ti I	4759.28	2.25	0.59	46.3	4.81	44.9	4.65	233	10
Si I	5793.08	4.93	-1.86	43.2	7.47	30.1	7.16	9	7	Ti I	4820.41	1.50	-0.38	41.1	4.92	40.7	4.77	126	10
Si I	5948.54	5.08	-1.09	83.0	7.49	70.9	7.23	16	7	Ti I	4885.09	1.89	0.41	syn	4.93	syn	4.7	231	10
Si I	6125.03	5.61	-1.53	30.6	7.50	23.1	7.30	30	7	Ti I	4913.62	1.87	0.22	49.3	4.86	50.9	4.77	157	10
Si I	6142.49	5.62	-1.48	33.6	7.51	23.8	7.27	30	7	Ti I	4926.15	0.81	-2.17	6.6	4.92	–	–	39	2
Si I	6145.02	5.61	-1.39	37.0	7.48	27.8	7.26	29	7	Ti I	4981.74	0.85	0.57	112.8	4.81	–	–	38	10
Si I	6237.34	5.59	-0.98	58.7	7.41	46.1	7.16	28	3	Ti I	4999.51	0.83	0.32	103.4	4.90	–	–	38	10
Si I	6244.48	5.61	-1.29	44.3	7.51	30.9	7.23	28	7	Ti I	5009.65	0.02	-2.2	syn	4.87	syn	4.63	5	10
Si I	6721.84	5.86	-0.94	42.2	7.32	–	–	–	2	Ti I	5016.17	0.85	-0.48	64.7	4.92	67.2	4.81	38	10
Si I	7003.58	5.94	-0.59	58.1	7.48	46.8	7.27	60	2	Ti I	5020.03	0.83	-0.33	77.5	5.05	76.6	4.84	38	10
Si I	7005.84	5.96	-0.59	72.8	7.48	67.4	7.35	60	2	Ti I	5022.87	0.83	-0.33	71.3	4.90	72.4	4.75	38	10
Si I	7034.96	5.85	-0.88	63.8	7.59	51.0	7.35	50	3	Ti I	5039.96	0.02	-1.08	76.2	4.97	77.8	4.82	5	10
Si I	7416.00	5.59	-0.75	87.1	7.45	–	–	22	3	Ti I	5064.65	0.05	-0.94	85.3	5.08	80.9	4.78	294	10
Si I	7918.38	5.93	-0.61	79.7	7.58	–	–	57	6	Ti I	5145.47	1.46	-0.54	36.9	4.92	35.7	4.74	109	10
Si I	9393.40	6.10	-1.53	13.3	7.35	–	–	72	3	Ti I	5147.48	0.00	-1.94	37.1	4.87	38.5	4.71	4	10
Si I	9768.27	4.93	-2.68	27.0	7.78	–	–	7	3	Ti I	5152.19	0.02	-1.95	36.5	4.88	35.8	4.68	4	10
P I	9525.78	6.98	-0.12	syn	5.56	syn	–	–	2	Ti I	5192.98	0.02	-0.95	83.9	5.00	–	–	4	10
P I	9750.73	6.92	-0.20	syn	syn	–	–	2	2	Ti I	5210.39	0.05	-0.82	90.0	5.02	–	–	4	10
P I	9796.79	6.99	0.19	syn	5.51	syn	–	–	2	Ti I	5219.71	0.02	-2.22	28.1	4.95	–	–	4	10
S I	8693.98	7.84	-1.38	syn	7.15	–	–	6	2	Ti I	5490.16	1.46	-0.84	22.6	4.84	23.5	4.71	107	10
S I	8694.70	7.84	0.05	syn	7.15	–	–	6	2	Ti I	5866.46	1.07	-0.79	47.9	4.98	–	–	72	10
Ca I	4512.27	2.52	-1.90	23.6	6.29	–	–	24	3	Ti I	5918.55	1.06	-1.47	12.2	4.71	–	–	71	2
Ca I	4526.94	2.70	-0.42	85.6	6.14	83.4	5.93	36	2	Ti I	5922.11	1.04	-1.47	20.1	4.96	22.6	4.86	72	2
Ca I	4578.56	2.52	-0.70	82.8	6.27	–	–	23	8	Ti I	5978.54	1.87	-0.50	23.9	4.92	24.0	4.78	154	2
Ca I	5260.39	2.52	-1.72	32.7	6.30	25.7	6.03	22	8	Ti I	6126.22	1.07	-1.42	21.6	4.97	24.4	4.88	69	10
Ca I	5261.71	2.52	-0.58	98.6	6.47	90.7	6.18	22	8	Ti I	6258.11	1.44	-0.39	50.3	4.96	49.3	4.79	104	10
Ca I	5512.99	2.93	-0.46	86.2	6.38	81.4	6.15	48	8	Ti I	6261.11	1.43	-0.53	46.5	5.01	46.1	4.85	104	10
Ca I	5581.98	2.52	-0.56	92.9	6.34	–	–	21	8	Ti I	6336.11	1.44	-1.69	5.3	4.88	–	–	103	10
Ca I	5590.13	2.52	-0.57	92.0	6.34	–	–	21	8	Ti I	6743.13	0.90	-1.63	18.4	4.88	–	–	32	10
Ca I	6166.44	2.52	-1.14	70.3	6.33	68.2	6.13	20	8	Ti I	7216.20	1.44	-1.20	18.3	4.97	–	–	98	10
Ca I	6169.04	2.52	-0.80	91.9	6.30	88.5	6.06	20	8	Ti I	7251.74	1.42	-0.76	33.7	4.89	31.7	4.69	99	10
Ca I	6169.56	2.52	-0.48	108.7	6.19	109.5	5.97	20	8	Ti I	7357.74	1.44	-1.02	22.6	4.90	–	–	97	10
Ca I	6439.07	2.51	0.39	160.0	6.07	157.1	5.80	18	2	Ti I	8024.84	1.87	-1.08	10.6	4.94	–	–	151	10
Ca I	6455.60	2.52	-1.34	55.4	6.34	48.2	6.10	19	8	Ti I	8364.24	0.83	-1.71	22.1	4.90	26.5	4.85	33	3
Ca I	6471.67	2.52	-0.69	90.5	6.36	88.2	6.17	18	8	Ti I	8396.93	0.81	-1.63	25.2	4.88	27.0	4.76	33	3
Ca I	6493.79	2.52	-0.11	122.7	6.22	124.3	6.03	18	8	Ti I	8412.36	0.81	-1.39	39.7	4.96	36.6	4.74	33	2
Ca I	6499.65	2.52	-0.82	86.1	6.41	80.8	6.18	18	8	Ti I	8426.50	0.82	-1.20	53.0	5.03	54.7	4.91	33	2
Ca I	6572.79	0	-4.32	syn	6.32	syn	6.15	1	8	Ti I	8434.98	0.84	-0.83	71.2	5.07	77.6	5.08	33	2
Ca I	7148.15	2.70	0.11	135.6	6.20	137.4	5.99	30	8	Ti I	8435.68	0.83	-1.02	61.7	5.06	66.0	5.02	33	2
Ca I	7202.19	2.70	-0.26	108.2	6.26	–	–	29	3	Ti I	9027.32	1.73	-1.36	7.8	4.87	–	–	138	3
Ca I	7326.15	2.92	-0.21	108.2	6.38	104.4	6.15	20	3	Ti I	9675.55	0.83	-0.80	78.6	5.04	70.7	4.76	32	3
Ca I	9663.58	4.71	-0.69	6.5	6.22	–	–	55	3	Ti I	9718.96	1.50	-1.18	16.4	4.79	–	–	124	3
Sc I	4023.69	0.02	0.38	syn	3.13	–	–	7	9	Ti I	9728.36	0.81	-1.21	47.2	4.82	–	–	32	3
Sc II	4246.84	0.31	0.24	157.0	3.17	–	–	7	9	Ti I	9770.28	0.84	-1.58	26.7	4.80	–	–	32	3
Sc II	5239.82	1.45	-0.76	syn	3.15	syn	2.82	26	9	Ti I	9787.67	0.82	-1.44	40.3	4.92	–	–	32	3

Table A4. The abundances were obtained for a model with $T_{\rm eff}$ = 5770 K, $\log g$ = 4.40 cgs, and ξ = 0.66 km s^{-1} for the solar spectrum. $T_{\rm eff}$ = 5600 K, $\log g$ = 4.50 cgs, and ξ = 0.44 km s^{-1} for the HD 218209 spectrum.

				Sun		HD 218209								Sun		HD 218209			
Spec.	λ	LEP	$\log(gf)$	EW	$\log\epsilon$(X)	EW	$\log\epsilon$(X)	RMT	Ref.	Spec.	λ	LEP	$\log(gf)$	EW	$\log\epsilon$(X)	EW	$\log\epsilon$(X)	RMT	Ref.
	(Å)	(eV)	(dex)	(mÅ)	(dex)	(mÅ)	(dex)				(Å)	(eV)	(dex)	(mÅ)	(dex)	(mÅ)	(dex)		
Ti II	4443.81	1.08	-0.71	146.1	5.09	126.4	4.73	19	10	Ni I	4606.23	3.60	-1.02	syn	6.36	syn	5.89	100	2
Ti II	4468.50	1.13	-0.63	syn	5.21	syn	4.85	31	10	Ni I	4731.80	3.83	-0.85	42.7	6.28	31.3	5.92	163	2
Ti II	4493.53	1.08	-2.78	34.7	4.91	–	–	18	10	Ni I	4732.47	4.10	-0.55	42.2	6.24	–	–	235	2
Ti II	4568.33	1.22	-2.65	29.7	4.78	–	–	60	10	Ni I	4752.43	3.66	-0.69	syn	6.33	syn	5.8	132	2
Ti II	4583.41	1.16	-2.84	31.3	4.95	–	–	39	10	Ni I	4756.52	3.48	-0.34	syn	6.23	syn	5.74	98	2
Ti II	4708.67	1.24	-2.35	50.7	5.01	46.2	4.87	49	10	Ni I	4806.99	3.68	-0.64	59.4	6.30	47.9	5.93	163	2
Ti II	4874.01	3.09	-0.86	syn	4.95	syn	4.68	114	10	Ni I	4829.03	3.54	-0.33	77.1	6.17	67.4	5.83	131	2
Ti II	4911.20	3.12	-0.64	51.2	5.10	46.1	5.00	114	10	Ni I	4852.56	3.54	-1.07	syn	6.29	syn	5.92	130	2
Ti II	5005.17	1.57	-2.73	23.8	5.01	19.5	4.85	71	10	Ni I	4904.42	3.54	-0.17	84.9	6.14	74.7	5.79	129	2
Ti II	5336.79	1.58	-1.60	72.0	5.08	–	–	69	10	Ni I	4913.98	3.74	-0.62	53.9	6.20	41.5	5.82	132	2
Ti I	5418.77	1.58	-2.13	48.5	5.02	43.8	4.88	69	10	Ni I	4935.83	3.94	-0.36	58.5	6.20	48.9	5.89	177	2
V I	4437.84	0.29	-0.71	syn	3.89	syn	–	21	11	Ni I	4946.03	3.80	-1.29	25.9	6.29	15.2	5.87	148	2
V I	5727.06	1.08	-0.02	syn	3.89	–	–	35	11	Ni I	4953.21	3.74	-0.66	54.8	6.26	44.4	5.92	111	2
V I	6090.18	1.08	-0.07	syn	3.93	syn	3.52	34	2	Ni I	4998.23	3.61	-0.78	54.8	6.26	–	–	111	2
V I	6119.53	1.06	-0.36	syn	3.94	syn	3.6	34	11	Ni I	5010.94	3.63	-0.87	48.0	6.21	34.2	5.80	144	2
V I	6243.11	0.30	-0.94	syn	3.88	syn	3.52	19	11	Ni I	5032.73	3.90	-1.27	24.1	6.31	–	–	207	2
Cr I	4545.96	0.94	-1.38	83.5	5.70	75.5	5.33	10	2	Ni I	5035.37	3.63	0.29	97.6	5.91	89.5	5.60	143	2
Cr I	4616.13	0.98	-1.18	87.7	5.64	79.4	5.27	21	2	Ni I	5042.19	3.64	-0.57	59.0	6.15	51.0	5.85	131	2
Cr I	4626.18	0.97	-1.32	81.5	5.62	75.7	5.31	21	2	Ni I	5048.85	3.85	-0.37	syn	6.26	syn	5.86	195	2
Cr I	4646.17	1.03	-0.71	syn	5.71	syn	5.16	21	2	Ni I	5082.35	3.66	-0.54	63.6	6.23	–	–	130	2
Cr I	4651.29	0.98	-1.46	78.3	5.69	72.9	5.40	21	2	Ni I	5084.10	3.68	0.03	89.1	6.10	–	–	162	2
Cr I	4652.17	1.00	-1.03	99.7	5.72	90.5	5.34	21	2	Ni I	5088.54	3.85	-0.91	32.1	6.12	–	–	190	2
Cr I	4708.02	3.17	0.11	58.0	5.58	44.0	5.16	186	2	Ni I	5102.97	1.68	-2.62	47.3	6.12	–	–	49	2
Cr I	4718.42	3.19	0.10	65.8	5.75	55.0	5.40	186	2	Ni I	5115.40	3.83	-0.11	74.8	6.17	60.6	5.76	177	2
Cr I	4730.72	3.08	-0.19	48.5	5.65	37.1	5.28	145	2	Ni I	5155.13	3.90	-0.66	49.0	6.27	35.2	5.86	206	2
Cr I	4737.35	3.07	-0.10	55.5	5.65	42.7	5.25	145	2	Ni I	5435.87	1.99	-2.60	50.9	6.47	40.7	6.10	70	2
Cr I	4756.12	3.10	0.09	63.2	5.76	54.2	5.44	145	2	Ni I	5587.87	1.93	-2.14	syn	6.23	syn	5.69	70	2
Cr I	4936.34	3.11	-0.34	44.8	5.73	31.8	5.31	166	2	Ni I	5593.75	3.90	-0.84	42.0	6.27	–	–	206	2
Cr I	4964.93	0.94	-2.53	38.6	5.65	27.3	5.21	9	2	Ni I	5625.33	4.09	-0.70	39.0	6.25	24.5	5.82	221	2
Cr I	5247.57	0.96	-1.63	83.4	5.79	72.6	5.38	18	2	Ni I	5637.12	4.09	-0.80	33.8	6.23	21.4	5.83	218	2
Cr I	5296.70	0.98	-1.41	93.5	5.77	79.7	5.31	18	2	Ni I	5641.89	4.10	-1.08	23.5	6.27	–	–	234	2
Cr I	5300.75	0.98	-2.13	58.4	5.72	45.4	5.26	18	2	Ni I	5682.21	4.10	-0.47	51.5	6.29	37.7	5.90	232	2
Cr I	5345.81	1.00	-0.98	114.5	5.68	–	–	18	2	Ni I	5748.36	1.68	-3.26	29.1	6.26	–	–	45	2
Cr I	5348.33	1.00	-1.29	99.8	5.77	–	–	18	2	Ni I	5805.23	4.17	-0.64	40.4	6.29	24.6	5.83	234	2
Cr I	5787.93	3.32	-0.08	45.2	5.60	31.8	5.19	188	2	Ni I	6007.32	1.68	-3.34	24.9	6.21	17.6	5.85	42	2
Cr I	6925.24	3.43	-0.33	37.9	5.75	–	–	222	2	Ni I	6086.29	4.26	-0.51	42.3	6.27	29.4	5.89	249	2
Cr I	6926.04	3.43	-0.62	20.5	5.61	–	–	222	3	Ni I	6108.12	1.68	-2.44	65.2	6.27	55.1	5.91	45	2
Cr I	6979.82	3.45	-0.41	34.7	5.74	–	–	222	2	Ni I	6128.98	1.68	-3.32	25.3	6.20	17.0	5.81	42	2
Cr I	7400.23	2.89	-0.11	75.4	5.58	–	–	93	2	Ni I	6130.14	4.26	-0.96	21.1	6.22	14.6	5.93	248	2
Cr I	8348.28	2.70	-1.87	13.1	5.83	–	–	56	3	Ni I	6175.37	4.09	-0.54	47.4	6.24	33.7	5.85	217	2
Cr I	8947.20	3.09	-0.75	28.1	5.49	–	–	142	3	Ni I	6176.82	4.09	-0.53	63.1	6.53	–	–	228	2
Cr I	8976.88	3.07	-1.03	18.5	5.50	–	–	142	3	Ni I	6204.61	4.09	-1.14	20.9	6.23	–	–	226	2
Cr I	9290.44	2.53	-0.88	58.6	5.69	–	–	29	3	Ni I	6322.17	4.15	-1.17	17.4	6.20	10.3	5.84	249	2
Cr I	9730.32	3.54	-0.77	12.9	5.45	–	–	226	3	Ni I	6327.60	1.68	-3.15	41.5	6.40	27.2	5.92	44	2
Cr I	9900.87	2.97	-2.14	5.2	5.81	–	–	80	3	Ni I	6378.26	4.15	-0.90	31.7	6.31	–	–	247	2
Cr II	4588.20	4.07	-0.65	70.9	5.67	–	–	44	12	Ni I	6414.59	4.15	-1.21	17.2	6.24	–	–	244	2
Cr II	4616.64	4.05	-1.29	45.2	5.65	31.7	5.33	44	2	Ni I	6482.81	1.93	-2.63	41.1	6.11	27.9	5.67	66	2
Cr II	5237.32	4.07	-1.17	53.2	5.76	35.3	5.33	43	12	Ni I	6598.61	4.23	-0.98	24.3	6.28	15.2	5.92	249	2
Cr II	5305.87	3.83	-1.91	25.2	5.50	14.4	5.17	24	12	Ni I	6635.14	4.42	-0.83	24.6	6.32	17.6	6.04	264	2
Mn I	4055.55	2.14	-0.08	syn	5.47	syn	4.92	5	13	Ni I	6767.78	1.83	-2.17	77.9	6.41	–	–	57	2
Mn I	4082.94	2.18	-0.36	syn	5.55	syn	4.84	5	13	Ni I	6772.32	3.66	-0.99	48.5	6.26	–	–	127	4
Mn I	4451.59	2.89	0.28	syn	5.47	syn	4.83	22	13	Ni I	6914.56	1.94	-2.27	77.9	6.56	–	–	62	2
Mn I	4470.14	2.94	-0.44	syn	5.49	syn	4.92	22	13	Ni I	7030.06	3.53	-1.83	19.8	6.33	–	–	126	3
Mn I	4502.22	2.92	-0.34	syn	5.34	syn	4.74	22	13	Ni I	7110.91	1.93	-2.97	36.2	6.30	24.5	5.88	64	2
Mn I	4709.72	2.89	-0.49	syn	5.36	syn	4.75	21	13	Ni I	7385.24	2.73	-1.96	45.2	6.28	33.5	5.91	84	2
Mn I	4739.11	2.94	-0.61	syn	5.39	syn	4.73	21	13	Ni I	7422.30	3.62	-0.13	90.5	5.99	–	–	139	2
Mn I	4765.86	2.94	-0.09	syn	5.45	syn	4.75	21	13	Ni I	7522.78	3.64	-0.47	73.9	6.29	66.6	6.04	126	3
Mn I	4766.42	2.92	0.10	syn	5.41	syn	4.83	21	13	Ni I	7525.14	3.62	-0.43	69.0	6.14	57.7	5.81	139	3
Mn I	4783.42	2.30	0.03	syn	5.60	syn	4.84	16	13	Ni I	7555.60	3.83	0.05	90.3	6.23	77.6	5.88	187	3
Mn I	5117.94	3.13	-1.20	syn	5.45	–	–	32	13	Ni I	7574.08	3.82	-0.45	63.5	6.23	49.5	5.84	156	3
Mn I	5432.55	0.00	-3.79		5.33	syn	4.73	1	13	Ni I	7727.66	3.66	-0.17	87.2	6.23	70.5	5.82	156	3
Mn I	6013.50	3.06	-0.25	syn	5.46	syn	4.8	27	2	Ni I	7748.93	3.69	-0.18	84.5	6.22	75.8	5.94	156	3
Mn I	6021.80	3.07	-0.05	syn	5.56	syn	4.94	27	13	Ni I	7797.62	3.88	-0.18	75.1	6.22	63.8	5.90	201	3
Co I	4121.33	0.92	-0.33	syn	5.05	–	–	28	14	Ni I	8965.94	4.09	-0.89	39.4	6.30	–	–	225	3
Co I	4792.86	3.24	0.00	syn	4.89	syn	4.54	158	3	Cu I	5105.54	1.38	-1.50	syn	4.25	syn	3.8	2	2
Co I	4813.48	3.21	0.12	syn	5.04	syn	4.59	158	14	Cu I	5218.20	3.80	0.26	syn	4.11	syn	3.56	3.57	2
Co I	5352.05	3.58	0.06	syn	4.89	syn	4.40	172	14	Cu I	7933.13	3.77	-0.37	syn	4.21	–	–	6	3
Co I	5483.36	1.71	-1.50	syn	4.94	syn	4.54	39	14	Cu I	8092.63	3.80	-0.04	syn	4.23	syn	3.72	6	3
Co I	5647.23	2.27	-1.56	syn	4.94	syn	4.46	112	2	Zn I	4722.16	4.03	-0.39	syn	4.64	syn	4.49	2	15
Co I	6093.15	1.74	-2.40	syn	4.94	–	–	37	14	Zn I	4810.54	4.08	-0.17	syn	4.63	syn	4.42	2	15
Co I	8093.93	4.00	0.29	syn	4.94	syn	4.38	189	2	Sr I	4607.34	0.00	0.28	syn	2.84	syn	2.29	2	16
Ni I	4410.52	3.31	-1.08	55.6	6.33	–	–	88	2	Y II	4883.69	1.08	0.07	syn	2.3	syn	1.8	22	17
Ni I	4470.48	3.40	-0.40	80.5	6.24	71.5	5.90	86	2	Y II	5087.43	1.08	-0.17	syn	2.27	syn	1.74	20	17

Table A5. The abundances were obtained for a model with $T_{\rm eff}$ = 5770 K, $\log g$ = 4.40 cgs, and ξ = 0.66 km s^{-1} for the solar spectrum. $T_{\rm eff}$ = 5600 K, $\log g$ = 4.50 cgs, and ξ = 0.44 km s^{-1} for the HD 218209 spectrum.

				Sun		HD 218209								Sun		HD 218209			
Spec.	λ	LEP	$\log(gf)$	EW	$\log\epsilon$(X)	EW	$\log\epsilon$(X)	RMT	Ref.	Spec.	λ	LEP	$\log(gf)$	EW	$\log\epsilon$(X)	EW	$\log\epsilon$(X)	RMT	Ref.
	(Å)	(eV)	(dex)	(mÅ)	(dex)	(mÅ)	(dex)				(Å)	(eV)	(dex)	(mÅ)	(dex)	(mÅ)	(dex)		
Zr I	4772.32	0.62	0.04	syn	2.53	–	–	43	3	Ce II	4042.14	0.50	0.00	syn	1.60	–	–	252	2
Zr II	4208.98	0.71	-0.46	syn	2.6	–	–	41	18	Ce II	4562.37	0.48	0.21	syn	1.63	syn	1.49	1	20
Zr II	4050.32	0.71	-1.06	syn	2.62	syn	2.29	43	3	Ce II	4628.16	0.52	0.14	syn	1.56	–	–	1	20
Ba II	4554.04	0.00	0.14	syn	2.3	syn	1.99	1	19	Nd II	4021.33	0.32	-0.10	syn	1.38	–	–	36	3
Ba II	5853.69	0.60	-0.91	syn	2.33	syn	1.98	2	19	Nd II	4446.40	0.20	-0.35	syn	1.33	syn	1.07	49	3
La II	4086.72	0.00	-0.07	syn	1.2	syn	0.76	10	2	Nd II	4567.61	0.20	-1.31	syn	1.37	–	–	49	3
La II	4662.51	0.00	-1.25	syn	1.13	–	–	8	2	Sm II	4519.63	0.54	-0.35	syn	0.94	syn	0.72	49	21
La II	4748.73	0.92	-0.54	syn	1.1	syn	0.83	65	2	Sm II	4577.69	0.25	-0.65	syn	0.96	–	–	23	21

References for the adopted gf-values: (1) Fuhr & Wiese (2006), (2) NIST Atomic Spectra Database (http://physics.nist.gov/PhysRefData/ASD), (3) VALD, (4) Takeda et al. (2003), (5) Pehlivan Rhodin et al. (2017), (6)Kelleher & Podobedova (2008), (7) Shi et al. (2011), (8) Den Hartog et al. (2021), (9) Lawler et al. (2019), (10) Lawler et al. (2013), (11) Lawler et al. (2017), (12) Lawler et al. (2017), (13) Den Hartog et al. (2011), (14) Lawler et al. (2015), (15) Biemont & Godefroid (1980), (16) Hansen et al. (2013), (17) Hannaford et al. (1982), (18) Biemont et al. (1981), (19) Klose et al. (2002), (20) Lawler et al. (2009), (21) Lawler et al. (2006)

Table A6. Solar abundances from the literature. The abundances for species in bold type face are obtained via spectrum synthesis.

Species	$\log\epsilon_\odot$(X†) (dex)	n	$\log\epsilon_\odot$(X*)	n	ASP09/ASP21 (1),(2)	LOD (3)	GRE (4)	CAF (5-10)	HOL (11)	BIE (12)	LAM (13)
C I	**8.50±0.07**	**2**	-	-	8.43±0.05 / 8.46±0.04	8.39±0.04	8.39±0.05	8.50±0.06	8.592±0.108	8.60±0.10	8.67±0.10
O I	**8.85±0.04**	**3**	-	-	8.69±0.05 / 8.69±0.04	8.73±0.07	8.66±0.05	8.76±0.07	8.736±0.078	-	8.92±0.04
Na I	6.17±0.09	3	6.16±0.07	2	6.24±0.04 / 6.22±0.03	6.30±0.03	6.17±0.04	-	-	-	-
Mg I	**7.64±0.06**	**5**	7.60±0.08	2	7.60±0.04 / 7.55±0.03	7.54±0.06	7.53±0.09	-	7.538±0.060	-	-
Mg II	**7.67±0.00**	**1**	-	-	7.60±0.04/ 7.55±0.03	7.54±0.06	7.53±0.09	-	-	-	-
Al I	**6.45±0.02**	**8**	-	-	6.45±0.03 / 6.43±0.03	6.47±0.07	6.37±0.06	-	-	-	-
Si I	7.50 ±0.09	21	7.50±0.07	12	7.51±0.03 / 7.51±0.03	7.52±0.06	7.51±0.04	-	7.536±0.049	-	-
P I	**5.44±0.00**	**1**	-	-	5.41±0.03 / 5.41±0.03	5.46±0.04	5.36±0.04	5.46±0.04	-	-	-
S I	**7.15±0.00**	**2**	-	-	7.12±0.03 / 7.12±0.03	7.14±0.01	7.14±0.05	7.16±0.05	-	-	-
Ca I	6.29±0.10	20	6.34±0.08	18	6.34±0.04 / 6.30±0.03	6.33±0.07	6.31±0.04	-	-	-	-
Sc I	3.13±0.00	1	3.12±0.00	1	3.15±0.04 / 3.14±0.04	3.10±0.10	3.17±0.10	-	-	-	-
Sc II	3.18±0.11	10	3.23±0.08	7	3.15±0.04 / 3.14±0.04	3.10±0.10	3.17±0.10	-	-	-	-
Ti I	4.92±0.09	56	4.96±0.09	43	4.95±0.05 / 4.97±0.05	4.90±0.06	4.90±0.06	-	-	-	-
Ti II	4.99±0.10	9	4.99±0.08	12	4.95±0.05 / 4.97±0.05	4.90±0.06	4.90±0.0	-	-	-	-
V I	**3.92±0.02**	**5**	3.99±0.05	5	3.93± 0.08 / 3.90±0.08	4.00±0.02	4.00±0.02	-	-	-	-
Cr I	5.67±0.10	28	5.71±0.07	19	5.64±0.04 / 5.62±0.04	5.64±0.01	5.64±0.10	-	-	-	-
Cr II	5.64±0.11	4	5.64±0.14	3	5.64±0.04 / 5.62±0.04	5.64±0.01	5.64±0.10	-	-	-	-
Mn I	5.61±0.16	11	5.62±0.13	13	5.43±0.05 / 5.42±0.06	5.37±0.05	5.39±0.03	-	-	-	-
Fe I	7.49±0.11	252	7.54±0.09	132	7.50±0.04 / 7.46±0.04	7.45±0.08	7.45±0.05	7.52±0.12	7.448±0.082	7.54±0.03	7.48±0.09
Fe II	7.49±0.09	28	7.51±0.04	17	7.50±0.04 / 7.46±0.04	7.45±0.08	7.45±0.05	7.52±0.06	-	7.51±0.01	-
Co I	**4.96±0.06**	**8**	-	-	4.99±0.07 / 4.94±0.05	4.92±0.08	4.99±0.07	-	-	4.92±0.08	4.92±0.08
Ni I	6.24±0.10	60	6 .28±0.09	54	6.22±0.04 / 6.20±0.04	6.23±0.04	6.23±0.04	-	-	-	-
Cu I	**4.19±0.06**	**4**	-	-	4.19±0.02 / 4.18±0.05	4.21±0.04	4.21±0.04	-	-	-	-
Zn I	**4.63±0.00**	**2**	4.68±0.03	2	4.56±0.05 / 4.56±0.05	4.62±0.15	4.60±0.03	-	-	4.60±0.03	4.60±0.08
Sr I	**2.89±0.00**	**1**	2.91±0.00	1	2.87±0.07 / 2.83±0.06	2.92±0.05	2.92±0.05	-	-	-	-
Y II	**2.28±0.01**	**2**	2.29±0.05	2	2.21±0.05 / 2.21±0.05	2.21±0.02	2.21±0.02	-	-	-	-
Zr II	**2.59±0.08**	**2**	2.68±0.00	1	2.58±0.04 / 2.59±0.04	2.58±0.02	2.58±0.02	-	-	2.56±0.05	-
Ba II	**2.29±0.06**	**2**	2.24±0.06	4	2.18±0.09 / 2.27±0.05	2.17±0.07	2.17±0.07	-	-	-	-
La II	**1.11±0.06**	**3**	-	-	1.10±0.04 / 1.11±0.04	1.14±0.03	1.13±0.05	-	-	-	-
Ce II	**1.59±0.04**	**3**	1.64±0.02	2	1.58±0.04 / 1.58±0.04	1.61±0.06	1.70±0.10	-	-	1.70±0.04	-
Nd II	**1.37±0.01**	**3**	1.42±0.05	3	1.42±0.04 / 1.42±0.04	1.45±0.05	1.45±0.05	-	-	-	-
Sm II	**0.96±0.02**	**2**	0.96±0.00	1	0.96±0.04 / 0.95±0.04	1.00±0.05	1.00±0.03	-	-	-	-

X†: This study (TS), X*: Şahin et al. (2023), (1) Asplund et al. (2009), (2) Asplund et al. (2021), (3) Lodders et al. (2009), (4) Grevesse et al. (2007), (5) Caffau et al. (2007), (6) Caffau et al. (2008), (7) Caffau et al. (2009), (8) Caffau et al. (2010), (9) Caffau et al. (2011), (10) Caffau et al. (2019), (11) Holweger (2001), (12) Biemont et al. (1993), (13) Lambert (1978).

Table A7. The elemental abundances of HD 218209 from the literature for respective elements.

Species	TS24 (1)	TA23 (2)	RI20 (3)	LU17 (4)	DA15 (5)	MI11/13 (6)	TA07 (7)	VA05 (8)	MI04 (9)	GE04 (10) (LTE/NLTE)	AB88 (11)
C I	0.14	-0.08	0.18		-0.01						
O I	0.28	0.08	0.42			0.22					
Na I	-0.03		0.03	0.06		-0.02		0.10		0.23/0.16	
Mg I	0.24		0.17	0.29	0.18	0.19			0.19	0.41/0.43	
Al I	0.13		0.21	0.26		0.26				0.27/0.47	0.45
Si I	0.13		0.17	0.15	0.15	0.18	0.26	0.20	0.18		0.18
Ca I	0.15		0.12	0.19	0.13	-0.35					0.26
Sc II	0.06			0.15							
Ti I	0.21		0.24	0.21	0.20		0.03	0.23			
V I	-0.02		0.17	0.16	0.13		0.03				
Cr I	-0.02		-0.07	0.03							
Cr II	0.01										
Mn I	-0.27		-0.27	-0.14	-0.16						
Co I	-0.10			0.08			0.13				
Ni I	-0.02		0.01	-0.01		0.04	0.00	0.01	0.04		0.19
Cu I	-0.13			-0.03	-0.07	-0.02					
Zn I	0.20			0.12		0.14					
Sr I	-0.18			0.10							
Y II	-0.14		0.02	0.08		-0.04					
Zr II	0.05			0.26		0.01					
Ba II	0.04			0.04		-0.01					
La II	0.03			0.63		0.09					
Ce II	0.26			0.28		-0.02					
Nd I	0.08			0.32		0.15					
Sm II	0.14			0.26		0.13					

(1) This Study, (2) Takeda (2023, TA23), (3) Rice & Brewer (2020, RI20), (4) Luck (2017, LU17), (5) da Silva et al. (2015, DA15), (6) Mishenina et al. (2011, MI11), (6) Mishenina et al. (2013, MI13), (7) Takeda et al. (2007, TA07), (8) Valenti & Fischer (2005, VA05), (9) Mishenina et al. (2004, MI04), (10) Gehren et al. (2004, GE04), (11) Abia et al. (1988, AB88).

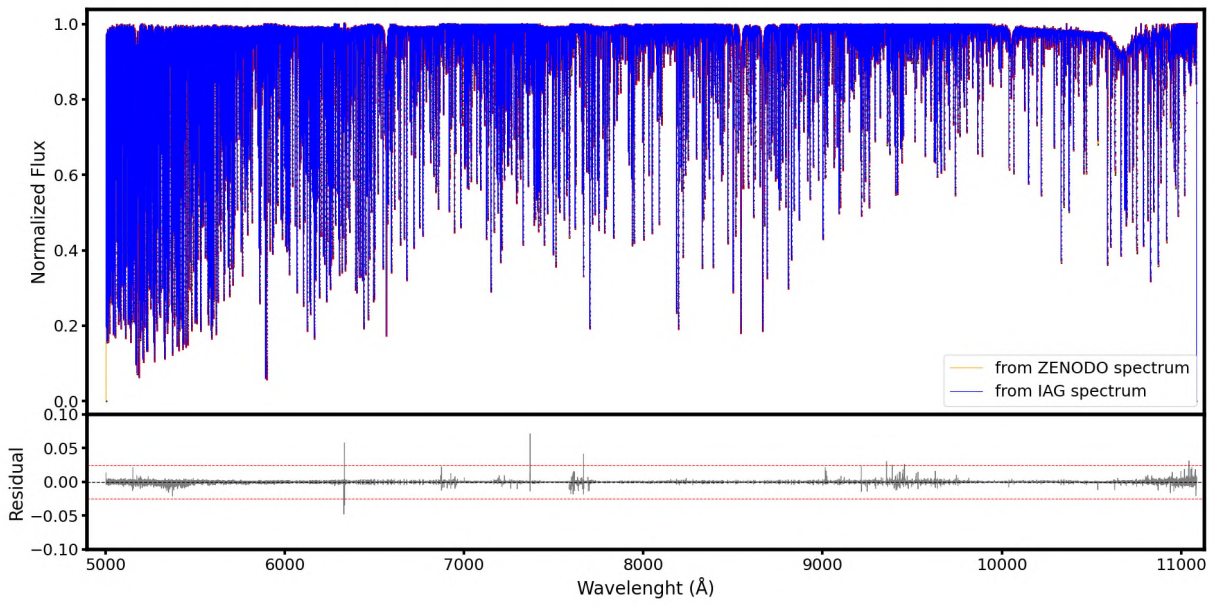

Figure A1. The normalized blue colour spectrum is the IAG spectrum, and the red colour spectrum is the ZENODO spectrum.

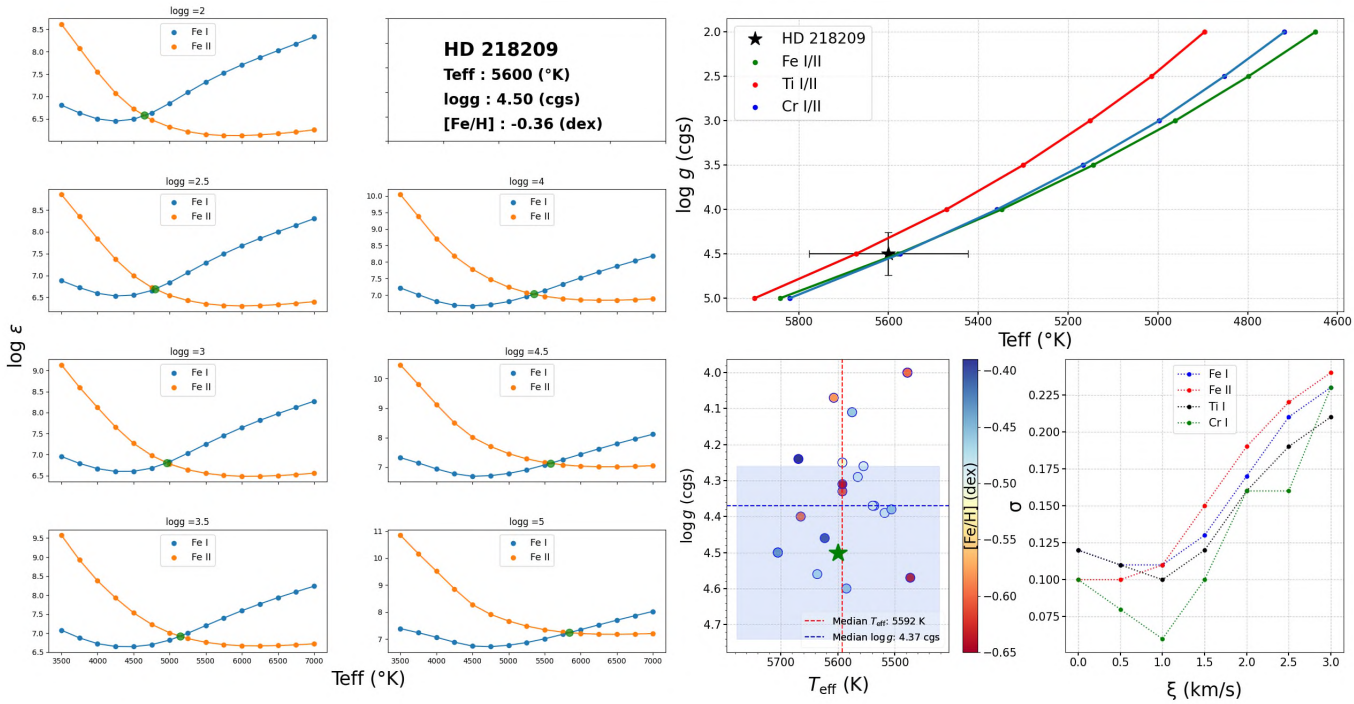

Figure A2. The dispersion test for Ti, Cr, and Fe. The standard deviations of Ti, Cr, and Fe abundances for a suite of the Ti I, Cr I, Fe I, and Fe II lines as a function of ξ were provided. The stellar parameters reported in the literature for the star exhibit large variations (the middle panel). The faint blue area in the image represents errors in the model parameters.

İSTANBUL UNIVERSITY PRESS

Physics and Astronomy Reports
PAR 2024, 2 (2), 83–87
DOI: 10.26650/PAR.2024.00008

RESEARCH ARTICLE

A Case Study on Statistical Analysis of Geomagnetic Storm 3-5 August 2010

Z. Can[1*], and H. Ş. Erdağ[2]

[1]Yıldız Technical University, Faculty of Art and Sciences, Department of Physics, Davutpasa, 34220, İstanbul, Türkiye
[2]Gebze Technical University, Faculty of Science, Department of Physics, 41400, Gebze, Kocaeli, Türkiye

ABSTRACT

The solar flare that occurred on August 1, 2010, was a powerful event that led to the interaction of two coronal mass ejections (CMEs), resulting in a significant CME-CME eruption. This eruption struck Earth on August 3, causing a major geomagnetic storm that had widespread impacts on Earth's magnetic environment. Detecting geomagnetic storms is essential for safeguarding space missions, satellite operations, and communications systems. Failure to accurately predict these storms can disrupt critical infrastructure. The CME-CME interaction in August 2010 differs from ordinary CMEs in terms of particle velocity and density, which were observed to reach unprecedented levels during this event.In this study, a statistical model using the multiple linear regression method was developed to examine the effects of CME-CME interaction on Earth's magnetic field by utilizing characteristics such as particle velocity (v) and density (Np). The study evaluated the effects of solar parameters during G3 and G2-level geomagnetic storms. It was found that particle density significantly increases the intensity and duration of geomagnetic storms, whereas particle velocity notably reduces these effects, exhibiting an opposing influence.

Keywords: Geomagnetic storm; coronal mass ejection; CME-CME interaction; regression; statistical analysis; space weather.

1. INTRODUCTION

Space weather has gained traction as an important area of study in recent years, continuing a long tradition of scientific research to understand processes occurring in the Earth's near-space environment. Space weather refers to the collective results and effects of a series of physical phenomena originating from the Sun and propagating through the interplanetary environment. Magnetic field disruptions on the Sun give rise to sunspots - dark regions on the Sun's surface (photosphere) that are cooler than their surroundings. These spots are caused by twisted magnetic fields. They create active regions that can produce solar flares. Active regions can also eject magnetized plasma at high speeds. This plasma can travels through interplanetary space. This plasma ejection into the interplanetary region is called a Coronal Mass Ejection (CME). If CMEs are released consecutively and the trailing CME catches up with the preceding one, the event is referred to as a CME-CME interaction or cannibalistic CME (Chattopadhyay & Khondekar 2023). The merging of these large-scale magnetic structures, carrying ionized plasma, leads to a buildup at the front of the CME. The interaction between the two magnetized plasma systems further complicates the structure (Gopalswamy 2001). Moreover, energy stored in twisted magnetic fields above sunspots can be abruptly released, causing solar flares-phenomena that often occur alongside various solar events (gsfc.nasa.gov).

On August 1, 2010, sunspot 1092 produced a C3-class solar flare, accompanied by the eruption of a massive magnetic filament across the Sun's northern hemisphere. These events, likely connected by long-range magnetic fields, merged to form a CME-CME interaction, recorded by NASA's Solar Dynamics Observatory. Figure 1 is a visual representation of the Sun during this event, highlighting sunspot 1092 and resulting flare. This event struck Earth in the evening hours of August 3 and caused a significant disturbance in Earth's magnetic field (magnetosphere), resulting in a geomagnetic storm. The detection and understanding of geomagnetic storms are crucial due to their impact on modern processes such as space missions, satellite safety, atmospheric processes, and communication. If a second CME, ejected from a region near the first, moves faster than the initial CME, it will overtake and engulf it. Thus, this formation, which is formed by the interaction of two CMEs and is called a cannibal CME, has a more complex structure than typical CMEs. Since these cannibal CMEs are the combination of two different coronal mass ejections, they are larger and more complex than typical CMEs in terms of speed and intensity. The August 2010 storm exemplifies a cannibalistic CME, exhibiting the distinctive characteristics. Parameters such as the velocity, pressure, and density of particles from the Sun, as well as the direction of the interplanetary magnetic field, play a significant role in the formation of geomagnetic storms. In this

Corresponding Author: Z. Can **E-mail:** zehcan@yildiz.edu.tr
Submitted: 07.10.2024 • **Revision Requested:** 07.11.2024 • **Last Revision Received:** 16.12.2024 • **Accepted:** 18.12.2024

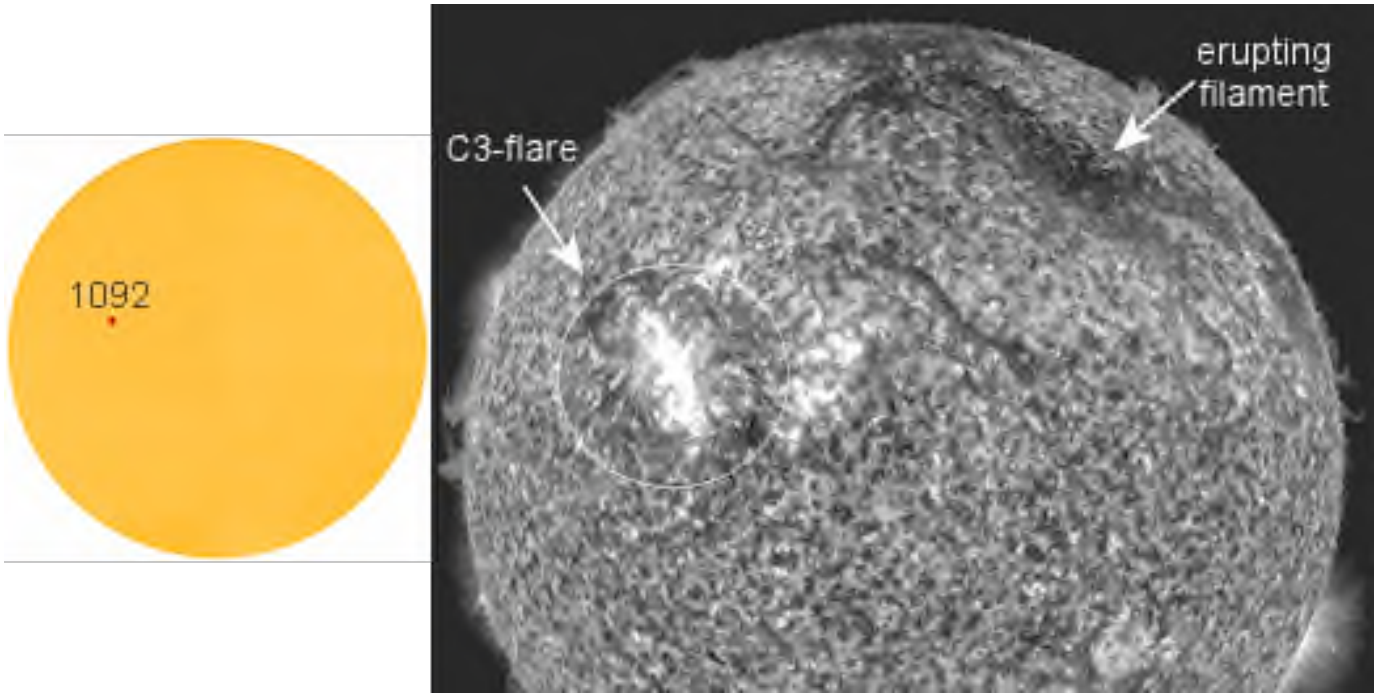

Figure 1. *S*unspot number 1092 and the resulting flare (Space Weather 2024).

study, we utilized particle velocity (v) and density (Np)—the two distinguishing features of the cannibalistic CME compared to other ejections and solar winds. To reveal the effects of solar parameters on Earth's magnetic field during the consecutive G3 (strong geomagnetic storms with a Kp index between 7 and 8 and a Dst index between -100 nT and -250 nT) and G2 (moderate geomagnetic storms with a Kp index between 6 and 7 and a Dst index between -50 nT and -100 nT) level geomagnetic storms, we developed a statistical model.

Table 1. G, Kp, and Dst index ranges corresponding to various storm levels.

Geomagnetic Storm	G Index	Kp Range	Dst Range
Quite Day	G0	Kp< 5	−30 < Dst
Weak	G1	5 ≤Kp< 6	−50 < Dst ≤ −30
Moderate	G2	6 ≤Kp< 7	−100 < Dst ≤ −50
Strong	G3	7 ≤Kp< 8	−250 < Dst ≤ −100
Severe	G4	8 ≤Kp< 9	−500 < Dst ≤ −250
Extreme	G5	Kp≥ 9	Dst ≤-500

2. DATA

The Dst index is the most widely used measure for classifying geomagnetic storms. If the Dst peak value is between -30 and -50 nT, the storm is classified as weak; if the Dst peak value is between -50 and -100 nT, it is considered a moderate storm; and if the Dst peak value falls below -100 nT, it is categorised as an intense storm (Prestes et al. 2017; Gonzalez et al. 1994). Geomagnetic storms are also classified based on the planetary K index (Kp), which defines the intensity of the disturbance. The Kp index ranges from 0 (very quiet) to 9 (very disturbed) and is related to 28 different values: 0, 0+, 1-, 1, 1+, ..., 9-, 9 (Bartels 1949). When the Kp value is five or higher, it is represented by the geomagnetic storm index G. The classification of geomagnetic activity according to G, Kp, and Dst ranges, as defined by the National Oceanic and Atmospheric Administration (NOAA) Space Weather Prediction Center (SWPC), is shown in Table 1 (Chakraborty & Morley 2020).

Particle velocity data from the Sun were obtained using the *WIND* satellite. Velocity and density data were collected hourly during the three-day storm. The independent variables represent the magnitude of particle velocity (v) and the proton density of the ejection (Np). In this way, matching hourly datasets for both v and Np were created. The Dst index was selected as the dependent variable to observe the variability in Earth's magnetic field. The primary reason for choosing the Dst index is its availability as hourly data, which aligns with the other variables. We obtained the Dst index data from the World Data Center for Geomagnetism, Kyoto (Kyoto University 2024). This database provides hourly Dst index values derived from geomagnetic observations collected by a global network of observatories. A disturbance in Earth's magnetic field is classified as a geomagnetic storm if the CME value exceeds -30 nT. Once this threshold is crossed, the day is no longer considered quiet but instead marked as the onset of a geomagnetic storm.

We used a multiple linear regression model to analyze the August 2010 ejection that caused the geomagnetic storm. The independent variables in the model were the particle velocity and particle density of the CME-CME interaction, while the dependent variable was the Dst index, which indicates the

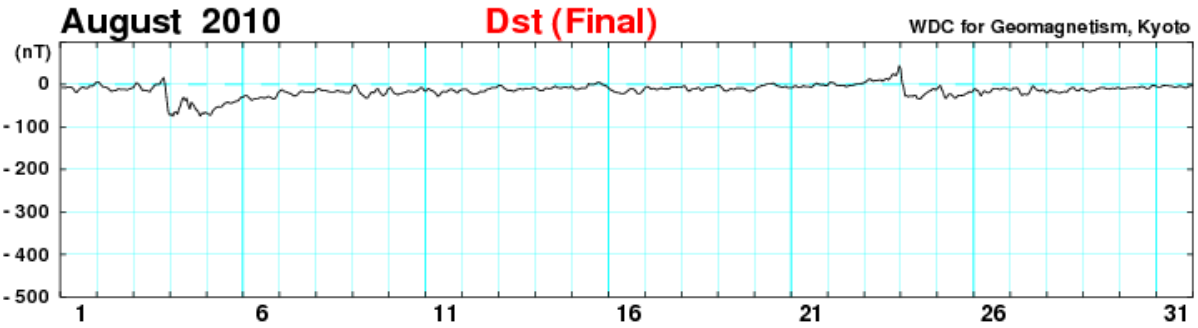

Figure 2. Dst index variation during August 2010.

disturbance in Earth's magnetic field. In the model, the quiet hours of the 3-5 August storm were identified, and a dummy variable was included for the hours when the storm occurred. In this way, the anomalous behavior in the magnetosphere was introduced into the model through the dummy variable.

Linear relationships between Earth's magnetic field and solar parameters were examined. Independent variables with no high correlation between them were selected. Multiple linear regression model tests were applied in the SPSS software for the independent variables (v, Np) and the dependent variable Dst. The significance of the model was evaluated through the model's result tables. The F-test was used to check if at least one variable in the model was significant (Table 2). Subsequently, it was confirmed that the significance values for each statistically significant independent variable fell within the confidence interval. To assess how were the changes in the dependent variable were explained, the R and R^2 values were obtained. The multiple linear regression model, using 70 data points for each variable, was constructed in the following equation form.

$$Y = \beta_0 + \beta_1 X_1 + \beta_2 X_2 + \beta_3 D_1 \quad (1)$$

where Y represents the dependent variable, Dst, while X values represent v and Np, respectively, and D represents the dummy variable. Here, the β values are the constant coefficients that will be obtained from the model for each variable.

3. RESULTS

Several (five) coronal mass ejections (CMEs) occurred from regions on the Earth-facing surface of the Sun. Two of the CMEs, ejected from the widespread and highly complex sunspot AR1092 on August 1, 2010, interacted and merged with each other, forming a magnetic structure known as a cannibalistic CME (or CME-CME, Temmer et al. 2012; Vrsnak 1992; Vršnak & Gopalswamy 2002). Additionally, a solar flare, a solar tsunami, the ejection of numerous magnetic filaments from the Sun's surface, large-scale oscillations of the solar corona, and radio bursts were detected. Upon ejections from the Sun, the CME interacts with the interplanetary medium, transferring energy and momentum through magnetohydrodynamic (MHD) waves (Jacques 1977). Figure 2 shows the Dst index variation for the month of August.

The CMEs ejected into interplanetary space by this complex eruption impacted Earth's magnetic field on August 3 and 4, which causing geomagnetic storms. The storm triggered by the CME-CME interaction caused the Dst index to drop to a value of -74 nT. Based on the Kp index calculated from Potsdam (located in Germany and home to the GFZ German Research Centre for Geosciences), we classified the August 3 storm as G3 and the August 4 storm as G2.

Figure 3 shows the variations in solar wind parameters from August 2-6, 2010, covering the period before, during, and after the geomagnetic storm. We used data from the *WIND* satellite, which is designed to provide information on the characteristics of the interplanetary magnetic field. The data obtained from the *WIND* satellite, listed from top to bottom, include the solar wind magnetic field strength (B), the z-component of the magnetic field (Bz), the magnitude of the solar wind speed (v), proton number density (Np), the solar wind ram pressure calculated from field and plasma parameters (Psw), and Akasofu's epsilon parameter (ε; 10^{11} W), which measures the energy transferred to Earth's magnetosphere. The data were obtained from the *WIND* satellite in the Geocentric Solar Magnetospheric (GSM) coordinate system and at high resolution (with 1-minute intervals) for detailed analysis.

As seen in Figure 3, the z-component of the magnetic field exhibited fluctuations within a range of approximately 30 nT. Before the storm, the solar wind speed was around 400 km s^{-1}, but with the onset of the storm, the speed increased by approximately 200 km s^{-1}, reaching 600 km s^{-1}. The particle number density rose to about 25 particles per cubic centimeter. The solar wind pressure also increased, reaching a value of approximately 18 nPa. During the storm, the ε parameter, measuring energy transfer from the solar wind to the environment, reached 20×10^{11} W.

The statistical model developed using the regression method was applied to the geomagnetic storm that occurred on August 3-5, 2010. In the model, where the confidence interval was set at 95%, the F-test resulted in a value less than 0.05 (Table 2). The model's outputs show that the R value, indicating the correlation between the dependent and independent variables, was

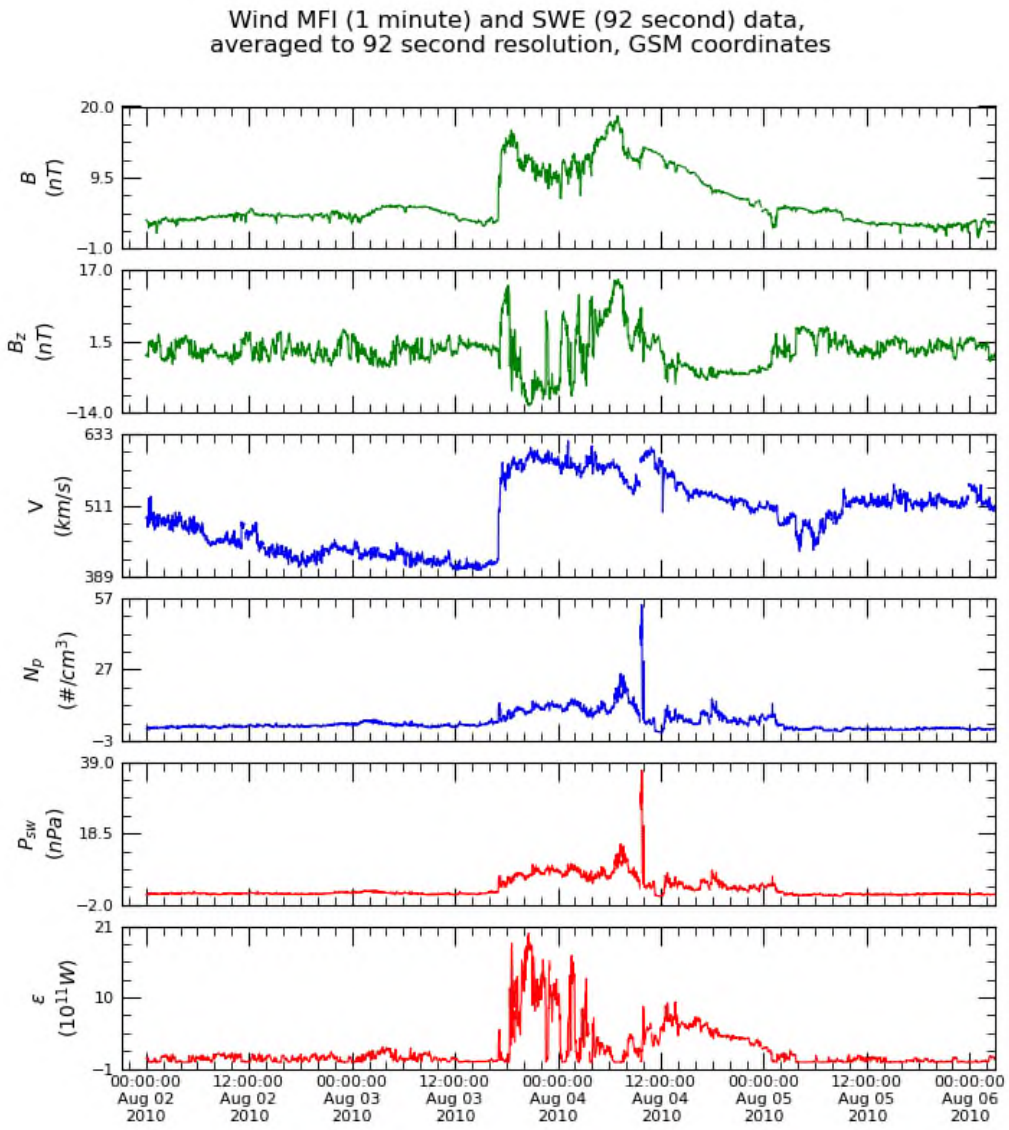

Figure 3. *V*ariations in solar wind parameters from the *WIND* satellite between August 2-6, 2010: B (magnetic field), Bz (component), v (magnitude of solar wind speed), Np (particle number density), and ε (Akasofu's epsilon parameter).

91.5%. Similarly, the R-squared value was found to be 83.7%, which is quite high. This R-squared value demonstrates that 83.7% of the variation in the dependent variable is explained by the independent variables. The coefficients obtained during the storm period indicate the effect of the velocity and density of the cannibalistic CME on the dependent variable, the Dst value. The beta coefficients are 0.156 for the CME-CME ejection velocity and -2.516 for the particle density. The significance values for the independent variables were found to be below 0.05.

4. CONCLUSION AND DISCUSSION

A statistically significant model was obtained for the August 3-5 geomagnetic storm using the developed statistical model.

Table 2. Statistical model results of the regression analysis applied to the geomagnetic storm of August 3-5, 2010.

F Test	R	R^2	β for v	β for Np	Sig. for v	Sig. for Np
<0.001	0.915	0.837	0.156	-2.516	<0.001	<0.001

The F-test of the model resulted in a value well below 0.05, as expected, demonstrating that at least one of the independent variables significantly explains the variation in the dependent variable. However, the key point is to observe the significant effect of both independent variables on the dependent variable. For this, the significance values of each independent variable in the model must be below 0.05. The significance values for each independent variable used in the geomagnetic storm model meet the required condition, allowing for the interpretation of

other model values. The high R value of 91.5% indicates that the selected independent variables are the most ideal for explaining the dependent variable. For the model to be successful, the independent variables must explain the variability in the dependent variable as much as possible. Here, the R-squared value of 83.7% shows that the independent variables in the model successfully explain the variability in the dependent variable. These results highlight the significant role of particle velocity and density among the ejection parameters as the primary sources of the geomagnetic storms and disturbances in Earth's magnetic field.

The statistical model developed in this study underscores that the velocity and density of the CME-CME ejection responsible for the August storm are key factors driving the storm. Based on the beta coefficients in the model, the following can be stated for each parameter: as the density of the CME-CME ejection increases, the Dst values of the resulting geomagnetic storm tend to shift towards more negative values. This plays a crucial role in increasing the strength (class) and duration of the geomagnetic storm, extending both the main phase and the recovery phase of the storm. However, the opposite is observed for particle velocity. As the unit velocity increases during the storm, the Dst value moves toward more positive values. Consequently, the storm's intensity decreases, and the storm duration shortens, allowing a quicker transition to a quiet day. An average unit change in density decreases the Dst value by -2.516 nT, while an average unit change in velocity increases the Dst by 0.156 nT. As seen in Figure 3 (speed and density graph numbers), specifically in the 3rd and 4th graphs from the bottom to the top, the significant variations in speed and density indicate that the coefficients of these variables have a substantial impact on the geomagnetic storm class and, consequently, on Earth's magnetic field.

These magnetic field disturbances in Earth's magnetic field can also affect the Earth's ionosphere, which is known as a natural plasma laboratory. This complex storm has been investigated by Valladares et al. (2017). They observed that during the storm, the Total Electron 157 Content (TEC) significantly increased at mid-latitudes. During the storm, the Kp index was 2 on August 2, 7- on August 3, 6+ on August 4, 4 on August 5, and 2+ on August 6. Accordingly, a G3 (strong) level storm occurred on August 3, and a G2 (moderate) level storm occurred on August 4. By August 5, conditions had returned to a quiet day. During the G3 (strong) level storm, voltage corrections may be required, surface charging of satellite components may occur, drag on low-Earth orbit satellites may increase, and attitude correction may be necessary. Additionally, satellite navigation and low-frequency radio navigation issues may arise.In conclusion, in order to minimize the serious effects of the disturbances in the Earth's magnetic field caused by geomagnetic storms on satellite operations, navigation systems and communication infrastructures, the dynamics of geomagnetic storms should be examined in more detail and comprehensively.

Peer Review: Externally peer-reviewed.
Author Contribution: Conception/Design of study - Z.C., H.Ş.E; Data Acquisition - H.Ş.E; Data Analysis/Interpretation - Z.C., H.Ş.E; Drafting Manuscript - H.Ş.E; Critical Revision of Manuscript - Z.C., H.Ş.E.; Final Approval and Accountability - Z.C., H.Ş.E., Supervision - Z.C.
Conflict of Interest: Authors declared no conflict of interest.
Financial Disclosure: Authors declared no financial support.

LIST OF AUTHOR ORCIDS

Z. Can https://orcid.org/0000-0002-3039-7454
H. Ş. Erdağ https://orcid.org/0000-0003-4584-8497

REFERENCES

Bartels J., 1949, IATME Bulletin, 12b, 97

Chakraborty S., Morley S. K., 2020, Journal of Space Weather and Space Climate, 10, 36

Chattopadhyay A., Khondekar M., 2023, Astronomy and Computing, 43, 100695

Gonzalez W. D., Joselyn J. A., Kamide Y., Kroehl H. W., Rostoker G., Tsurutani B. T., Vasyliunas V. M., 1994, Journal of Geophysical Research: Space Physics, 99, 5771

Gopalswamy 2001, The Astrophysical Journal, 548, l91

Jacques S. A., 1977, The Astrophysical Journal, 215, 942

Kyoto University 2024, World Data Center for Geomagnetism, Kyoto. Kyoto University, https://wdc.kugi.kyoto-u.ac.jp/dstdir/

Prestes A., Klausner V., González A. O., Serra S. L., 2017, Advances in Space Research, 60, 1850

Space Weather 2024, Space Weather: News and Information about the Sun-Earth Environment, https://www.spaceweather.com/

Temmer M., et al., 2012, The Astrophysical Journal, 749, 57

Valladares C. E., Eccles J. V., Basu S., Schunk R. W., Sheehan R., Pradipta R., Ruohoniemi J. M., 2017, Journal of Geophysical Research: Space Physics, 122, 3487

Vrsnak B., 1992, Annales Geophysicae, 10, 344

Vršnak B., Gopalswamy N., 2002, Journal of Geophysical Research: Space Physics, 107, SSH 2

İSTANBUL UNIVERSITY PRESS

Physics and Astronomy Reports
PAR 2024, 2 (2), 88–93
DOI: 10.26650/PAR.2024.00009

RESEARCH ARTICLE

Investigation of Transitions to the Atomic Ground State in Fourier Transform Spectra of Holmium

S. Kröger [1*], Gö. Başar [2], I. K. Öztürk [2], S. K. Barka [3,4], L. Windholz[5] and R. Ferber[6]

[1]Hochschule für Technik und Wirtschaft Berlin, Fachbereich 1, Wilhelminenhofstr. 75A, D-12459 Berlin, Germany
[2]İstanbul University, Faculty of Science, Department of Physics, TR-34134 Vezneciler, İstanbul, Türkiye
[3] İstanbul Technical University, Graduate School, Physics Engineering Program, TR-34469 Maslak, İstanbul, Türkiye
[4] Acıbadem Mehmet Ali Aydinlar University, Vocational School of Health Services, Opticianry Program, TR-34752 Ataşehir, İstanbul, Türkiye
[5]Institut für Experimentalphysik, Technische Universität Graz, Petersgasse 16, Graz A-8010, Austria
[6]Laser Centre, Faculty of Physics, Mathematics and Optometry, University of Latvia, LV-1586 Riga, Latvia

ABSTRACT

The aim of this study was to investigate in more detail some previously published atomic holmium energy levels, which were previously only published with very imprecise values for the level energy E and without total angular momentum quantum number J. By analysing Fourier Transform (FT) spectra in the 317 nm-1750 nm wavelength range using hyperfine structure as a diagnostic tool, we sought to enhance the precision of energy measurements and determine the unknown J values. All levels investigated were initially identified through their transitions to the ground state. We have investigated this transition and, if possible, other additional spectral lines that were classified as transitions to the investigated levels. A total of 13 lines from the FT spectra were analysed leading to results for six energy levels. For these six levels a more precise determination of the energy values could be achieved. With the investigation of the hyperfine structure knowledge on their previously unknown J values could be achieved. Furthermore, hyperfine structure constants of the investigated energy levels were determined for the first time.

Keywords: laser spectroscopy; fine structure; hyperfine structure; holmium

1. INTRODUCTION

The rare earth element holmium (Ho), which has an atomic number of 67 and a single stable isotope, ^{165}Ho, holds significant importance in astrophysics. For example, it is crucial in the study of nucleosynthesis, the process responsible for the formation of heavy elements in stars, and in determining the age of star clusters (see Sneden et al. 2009, and references therein). The nuclear spin of the isotope ^{165}Ho is $I = 7/2$. Its large nuclear magnetic dipole moment of $\mu_I = 4.17(3)\,\mu_N$ and its electric quadrupole moment $Q = 2.7\,\mathrm{b} - 3.6\,\mathrm{b}$ (Stone 2005) result in a widely splitting hyperfine structure (hfs) for most spectral lines. This hfs serves as a good fingerprint when searching for new fine structure energy levels.

This study is a continuation of years of extensive research into the atomic structure of Ho conducted by our research group (Kröger et al. 1997; Al-Labady et al. 2017; Başar et al. 2017; Özdalgiç et al. 2019a,b,c; Başar et al. 2020; Bingol et al. 2023; Barka et al. 2024; Zengin et al. 2024; Windholz et al. 2024). Other research groups have also carried out studies on fine structure, hyperfine structure and the discovery of new experimental fine structure energy levels of holmium in the last decade: (Furmann et al. 2018; Stefanska & Furmann 2018; Stefanska et al. 2018a,b; Furmann et al. 2019a,b; Chomski et al. 2021, 2022, 2023; Furmann et al. 2024). Despite these efforts, significant gaps remain in the experimental knowledge of energetically high-lying energy levels of Ho.

The present work is concerned with some energy levels which are mentioned in a paper by Smirnov (2013). In this reference, it is written: “Asterisks indicate the energies of five levels presented in [7] but not observed in other studies.”, where the reference [7] refers to a work by Gorshkov & Komarovskii (1979)[1].We found no mention of these levels in any other literature. This study aims to investigate these levels in greater detail. We have set our task of investigating these levels more closely. The aim was to determine the energy levels more precisely, to find out the J-values and to determine the hyperfine constants of these levels. For this purpose, we have checked our spectra for lines that include these levels.

[1] The work by Gorshkov & Komarovskii (1979) is published in the journal *Optika i spektroskopija* and is written in Russian language

Corresponding Author: S. Kröger **E-mail:** sophie.kroeger@htw-berlin.de
Submitted: 16.10.2024 • **Revision Requested:** 07.11.2024 • **Last Revision Received:** 24.11.2024 • **Accepted:** 26.11.2024

2. EXPERIMENT

The experimental spectra used in this study are the same as those analysed in several of our previous studies (Al-Labady et al. 2017; Başar et al. 2017; Özdalgiç et al. 2019a,b,c; Zengin et al. 2024). Thus, only a brief overview of the experimental setup is provided here.

The Ho samples used in our experiment had a purity of 99.9%. The free and excited Ho atoms were generated in a hollow cathode gas discharge running at approximately 60 mA current. Two Ho spectra were recorded with different buffer gases: one with argon (Ar) and the other with neon (Ne). Both spectra were obtained at buffer gas pressure of a few mbar. To minimize Doppler broadening, the hollow cathode was cooled using with liquid nitrogen.

The available spectra cover a range from 317 nm to 1750 nm. The accuracy of the calibrated wavenumber is 0.005 cm^{-1}. Further details can be found in Al-Labady et al. (2017); Başar et al. (2017); Zengin et al. (2024).

3. SELECTION AND ANALYSIS OF SPECTRAL LINES

In the paper of Gorshkov & Komarovskii (1979) 29 spectral lines of Ho I in the wavelength range from 315 nm to 610 nm are given, which are classified as transition to the ground state. For 20 of these 29 lines, the upper levels have been known before. The upper levels for the remaining nine lines have been published for the first time by Gorshkov & Komarovskii (1979) – as far as we know. The energy values in (Gorshkov & Komarovskii 1979) are given without decimal places (in cm^{-1}) and no J-values or information on electron configuration are given. The data from Gorshkov & Komarovskii (1979) for these nine lines are listed in Table 1. In addition, Table 1 shows the corresponding wavelengths from our spectra and the resulting energy values for the levels under investigation. In the last column the signal to noise ratio (SNR) from our spectra recorded with Ar as buffer gas is listed. One of the nine lines, which lies relatively far at the edge of our spectrum, is not visible in our spectra. The line may be likely weak, and the detector's reduced sensitivity in this range results in an insufficient SNR for detection. Two further lines lie below 317 nm and are therefore outside our wavelength range.

Table 1. Lines classified in Gorshkov & Komarovskii (1979) as transitions to the ground state and have an upper level with an unknown J value.

λ (nm)	E_{up} (cm^{-1})	λ (nm)	E_{up} (cm^{-1})	SNR
from reference		from our FT spectra		
357.912	27932	357.914	27 931.68	710
357.044	27999	357.035	28 000.44	190
354.141	28229	354.135	28 229.74	210
345.123	28966	345.121	28 967.07	190
320.617	31181	not seen in our spectra		
320.100	31231	320.099	31 231.24	4
318.637	31375	318.641	31 374.23	22
315.735	31663	not in our wavelength range		
315.382	31698	not in our wavelength range		

The initial step involved calculating all theoretically possible transitions to these six levels within the wavelength range of our FT spectra using the energy values given in Table 1 and trying all allowed J values for a transition to the ground level (with J=15/2), i.e. J = 13/2, 15/2 or 17/2. For this task, the computer program ELEMENTS was used (Windholz & Guthöhrlein 2003; Windholz 2016). When a line was found in the FT spectra, a 2 cm^{-1} wide section containing the line was extracted from the full spectrum.

In total, 13 lines were analysed, as listed in Table 2. This table also contains the six lines from Table 1, which are observed in our spectra. Level energies and J quantum numbers of the combining levels are given according to the NIST Atomic Spectra Database (Kramida et al. 2024). The SNR from our FT spectrum, measured with Ar as buffer gas is listed in the seventh column.

As the number of investigated lines is small, we show all observed hfs patterns in Figures 1-6.

For the determination of the level energy of the levels under investigation, only one transition is used in each case, and this is the transition to the ground state having $E = 0$ per definition. The ground state does not contribute to the uncertainty and therefore the uncertainty in determining the level energy of the upper levels results only from the wavenumber of the transition between the two levels. This uncertainty is estimated to be 0.01 cm^{-1}, which is composed of 0.005 cm^{-1} reading accuracy when determining the centre of gravity of the line and 0.005 cm^{-1} accuracy of the calibration. For the other lines the difference $\Delta\sigma = \sigma - (E_u - E_l)$ between the experimental wavenumber σ and the calculated difference between the level energies of the upper and lower levels E_u and E_l, respectively, is listed in the eighth column.

In order to determine the J-values, the J-values of the combining levels as well as the hyperfine structure (hfs) of the lines were taken into account. The possibilities for the J values of the investigated levels are restricted by the transition rules for electric dipole radiation and limited to $\Delta J = \pm 1$. This results in three possible J values for the levels under investigation when using a transition to the ground state. If other lines were available for a level under investigation, the J-choice may have been further restricted. The hfs was fitted for all possible J values and checked to see which J fit best. For the investigation of the hfs, the FITTER program (Zeiser et al. 2022) was used. This program iteratively fits a calculated hfs line profile to the experimental intensity distribution using a least-square method. For all lines, the hfs constants A and B of the respective other level are known from the literature. These values were fixed during the fitting procedure. Additionally, the hfs line profile parameters were fixed, and intensity ratios of the individual hfs components were constrained using theoretical intensity ra-

Table 2. Ho I lines measured by means of Fourier transform spectroscopy and analysed in order to determine hyperfine structure constants, sorted by levels of even parity; E_e, J_e, E_o, J_o: Energy and J-value for levels of even and odd parity, respectively.

E_e (cm^{-1})	J_e	E_o (cm^{-1})	J_o	λ_{air} (nm)	σ (cm^{-1})	SNR	$\Delta\sigma$ (cm^{-1})	A_e (MHz)	B_e (MHz)	com.
27 931.68	13/2	0.00	15/2	357 .914	27 931 .67	710	0 .00	657 (2)	-500 (50)	
		5 419.70	13/2	444 .084	22 511 .94	2	0 .03	only simulated		a
28 000.44	13/2	0.00	15/2	357 .035	28 000 .44	190	0 .00	544 (1)	690 (10)	
28 229.74	13/2	0.00	15/2	354 .135	28 229 .74	210	0 .00	992 (4)	1580 (390)	b
		5 419.70	13/2	438 .281	22 810 .00	17	0 .04	993 (12)	2060 (850)	
		18 572.28	15/2	1 035 .188	9 657 .44	4	0 .02	only simulated		c
		19 276.94	15/2	1 116 .649	8 952 .91	3	-0 .11	only simulated		d
28 967.07	13/2	0.00	15/2	345 .121	28 967 .07	190	0 .00	801 (12)	850 (510)	
		5 419.70	13/2	424 .557	23 547 .34	14	0 .03	only simulated		e
31 231.24	13/2	0.00	15/2	320 .099	31 231 .24	4	0 .00	only simulated		f
		5 419.70	13/2	387 .314	25 811 .51	24	0 .03	596 (3)	1430 (150)	
		8 605.16	11/2	441 .844	22 626 .07	32	0 .01	601 (4)	1270 (340)	
31 374.23	17/2	0.00	15/2	318 .641	31 374 .23	22	0 .00	792 (4)	670 (500)	g

a) very weak, simulation fits reasonably well (in the noise), b) blend, fit with two transitions, c) unresolved, weak, but structure fits well, d) very weak, good resolved, structure fits, e) fits well, f) very weak and g) unresolved

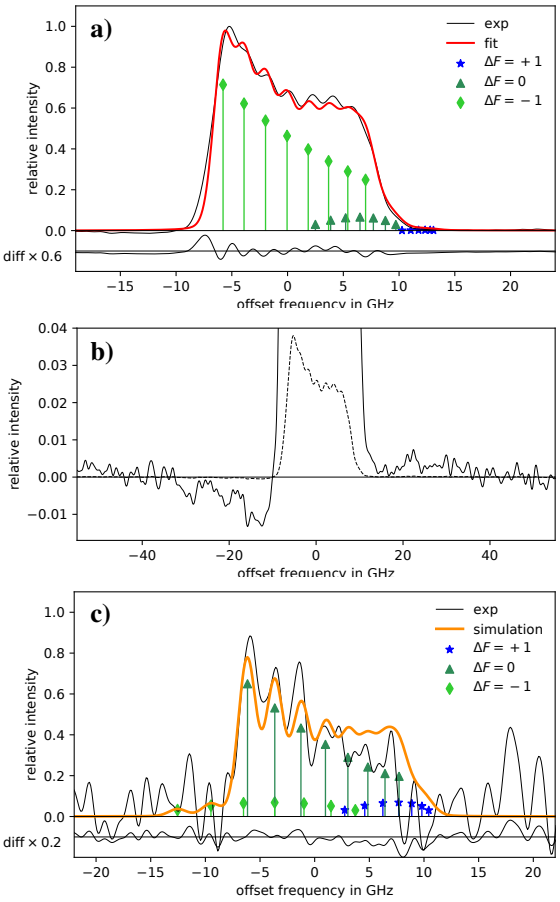

Figure 1. Lines including the even-parity energy level E = 27 931.68 cm^{-1}, J = 13/2; a) fit of FT-line at σ = 27 931.68 cm^{-1}; b) section of the experimental curve of figure (a) with the y-axis zoomed in to illustrate the asymmetry; c) simulation of FT-line at σ = 22 511.94 cm^{-1}.

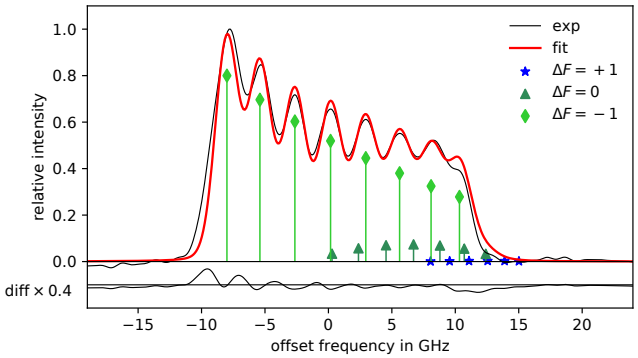

Figure 2. Line including the even-parity energy level E = 28 000.44 cm^{-1}, J = 13/2; fit of FT-line at σ = 28 000.44 cm^{-1}.

tios. In previous work (Özdalgiç et al. 2019c) we have already gained a lot of experience in fitting lines from these FT spectra. We used the same profile function as Özdalgiç et al. (2019c) – a Voigt profile – which fits the single hfs components more accurately than Gaussian or Lorentzian profiles. In this reference the full width at half maximum (FWHM) of the Voigt profile is investigated and as a result the FWHM for the Lorentzian and the Gaussian parts are given as a function of the line wavenumber. These results were used to fix the FWHM during the hfs fitting in the current study.

In all cases, the appropriate J-value for fitting the hfs could be determined with certainty. Of course the hfs parameters and J-values of the upper investigated level must fit to all transitions involving this level.

Our spectra exhibit a slight asymmetry in the spectral lines, which is already discussed in detail in Özdalgiç et al. (2019c). To illustrate this, a section of the experimental curve from Figure 1a is shown in Figure 1b, in which the x- and y-axes are scaled differently. To aid understanding, the curve from

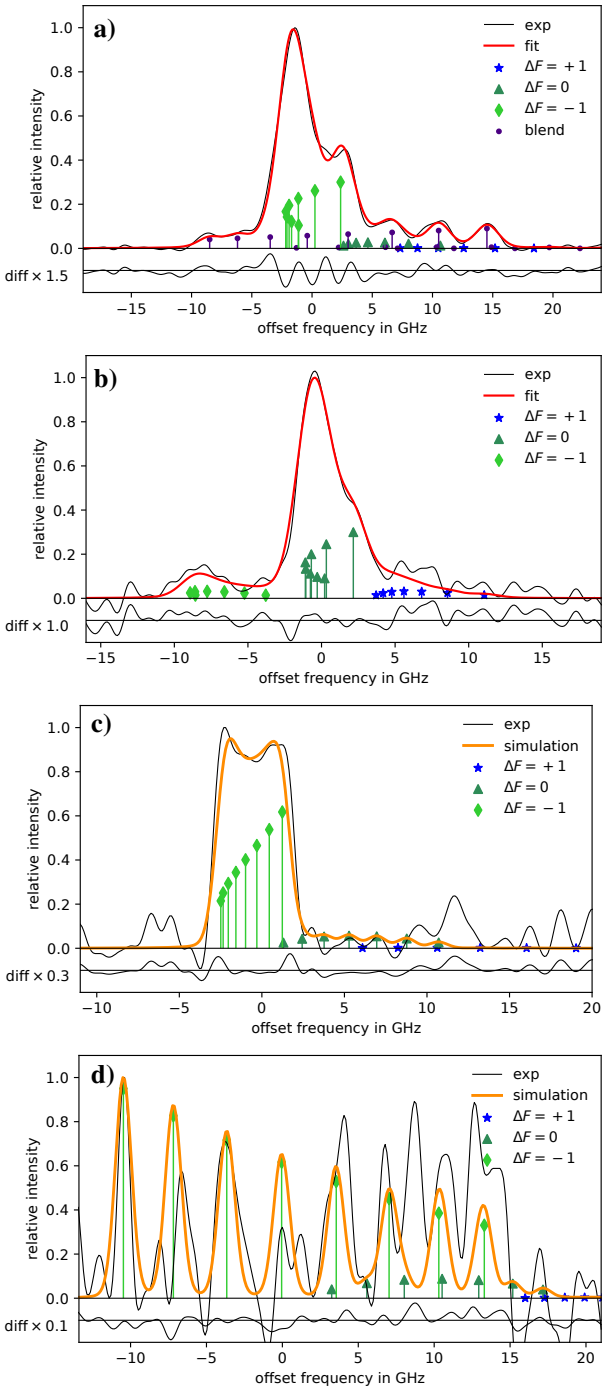

Figure 3. Lines including the even-parity energy level E = 28 229.74 cm^{-1}, J = 13/2; a) fit of FT-line at σ = 28 229.74 cm^{-1}, fitted together with another blending known line (transition at λ = 354.134 nm from E = 37 971.48 cm^{-1}, odd, J=17/2 to E=9 741.50 cm^{-1}, even, J=19/2); b) fit of FT-line at σ = 22 810.00 cm^{-1} ; c) simulation of FT-line at σ = 9 657.44 cm^{-1} ; d) simulation of FT-line at σ = 8 952.91 cm^{-1}.

Figure 1a is reproduced with new scaling. The asymmetry is especially significant for strong lines, leading to notable differences between the fitted and experimental curves, particularly for narrowly split lines. Nevertheless, the J value can be clearly

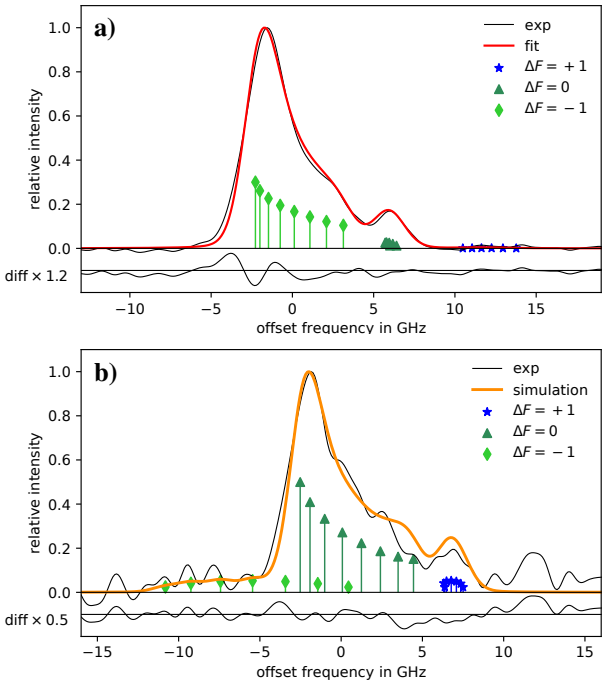

Figure 4. Lines including the even-parity energy level E = 28967.07 cm^{-1}, J = 13/2; a) fit of FT-line at σ = 28967.07 cm^{-1}; b) simulation of FT-line at σ = 23547.34 cm^{-1}.

determined and the A and B factors can also be reliably determined within the specified limits.

Two of the six levels yielded excellent results with more than two lines. For one level we could investigate three and for another one four transitions. For two other levels, exactly two lines were analysed, one of which was only fitted in each case; the other line is only simulated. Even so, the results can also be considered to be reliable here. For the remaining two levels, only one line was identified with no second line to confirm their existence. However, if the levels do exist, then the assignment of the J value is fairly clear.

4. CONCLUSION

We analysed 13 lines from FT spectra in order to investigate the six levels of atomic Ho, previously noted in the literature with only approximate energy values and without a J-value. We were able to determine the J values, provide more precise information on the energy value and specify hfs constants for all six levels. Hfs constants of all six levels could be determined and are published here for the first time.

Five of the six levels have a J-value of 13/2, all of which lie between 27 900 and 31 250 cm^{-1}, increasing the number of even levels with this J-value in this energy range considerably. In the theoretical investigation of the fine- and hyperfine structure of the even-parity configurations of Holmium done by Stefanska et al. (2018a), there are theoretical predictions which can now be filled with our experimental equivalence. An exact

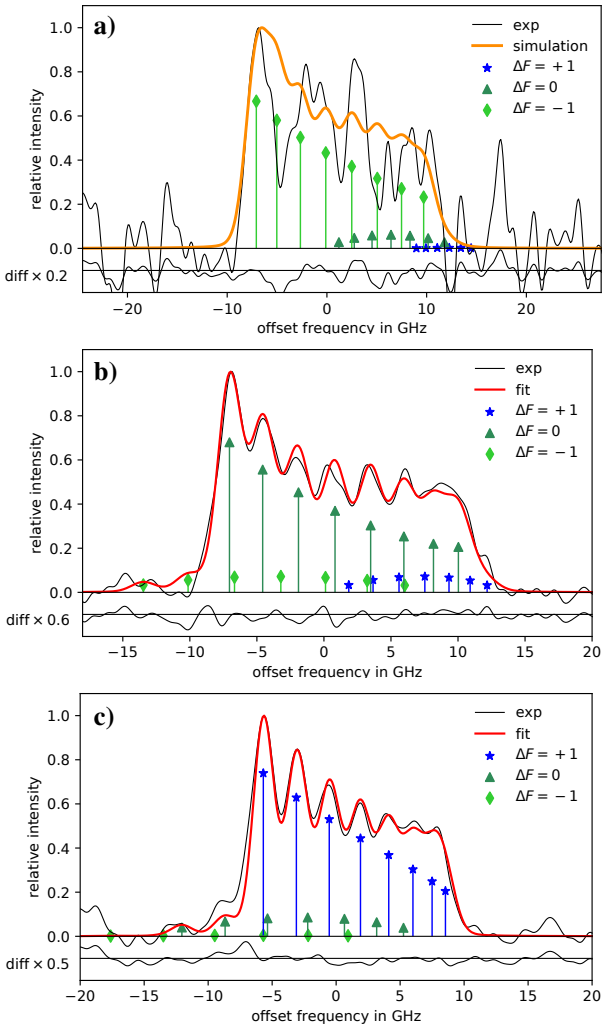

Figure 5. Lines including the even-parity energy level E = 31231.24 cm^{-1}, J = 13/2; a) simulation of FT-line at σ = 31231.24 cm^{-1}; b) fit of FT-line at σ = 25811.51 cm^{-1}; c) fit of FT-line at σ = 22626.07 cm^{-1}.

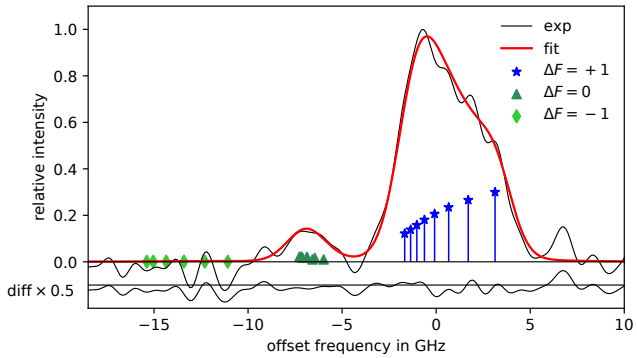

Figure 6. Line including the even-parity energy level E = 31374.23 cm^{-1}, J = 17/2; fit of FT-line at σ = 31374.23 cm^{-1}.

allocation of the experimental levels to the theoretical energies still needs to be clarified. It would be interesting to carry out the semi-empirical analysis of the even-parity configurations again, including the levels that we have newly provided with J-values and hfs constants.

Peer Review: Externally peer-reviewed.

Author Contribution: Conception/Design of study - S.K., Gö.B.; Data Acquisition - Gö.B., S.K., R.F.; Data Analysis/Interpretation - Gö.B., I.K.Ö, S.K.B., L.W.; Drafting Manuscript - S.K., Gö.B., S.K.B.; Critical Revision of Manuscript - I.K.Ö, L.W., R.F.; Final Approval and Accountability - S.K., Gö.B.; Technical or Material Support - R.F.

Conflict of Interest: Authors declared no conflict of interest.

Financial Disclosure: Authors declared no financial support.

LIST OF AUTHOR ORCIDS

S. Kröger https://orcid.org/0000-0003-4991-9176
Gö. Başar https://orcid.org/0000-0002-2428-8163
I. K. Öztürk https://orcid.org/0000-0002-3664-3388
S. K. Barka https://orcid.org/0000-0001-5789-1738
L. Windholz https://orcid.org/0000-0001-6078-6154
R. Ferber https://orcid.org/0000-0002-6313-5768

REFERENCES

Al-Labady N., et al., 2017, ApJS, 228, 16

Başar G., et al., 2017, ApJS, 228, 17

Başar G., Başar G., Özdalgiç B., Öztürk I. K., Güzelçimen F., Bingöl D., Kröger S., 2020, J. Quant. Spectrosc. Radiative Transfer, 243, 106809

Barka S. K., Başar G., Kröger S., Başar G., 2024, Spectrochimica Acta - Part B: Atomic Spectroscopy, 216, 106946

Bingol D., Basar G., Basar G., Kanat Ozturk I., Guzelcimen F., Kın Barka S., Kroger S., 2023, Physics and Astronomy Reports, 1, 85

Chomski M., Furmann B., Ruczkowski J., Suski M., Stefańska D., 2021, J. Quant. Spectrosc. Radiative Transfer, 274, 107865

Chomski M., Suski M., Wilman S., Furmann B., Ruczkowski J., Stefańska D., 2022, J. Quant. Spectrosc. Radiative Transfer, 279, 108045

Chomski M., Furmann B., Suski M., Głowacki P., Stefańska D., Mieloch S., 2023, J. Quant. Spectrosc. Radiative Transfer, 297, 108480

Furmann B., Stefanska D., Suski M., Wilman S., 2018, J. Quant. Spectrosc. Radiative Transfer, 219, 117

Furmann B., Stefańska D., Suski M., Wilman S., Chomski M., 2019a, J. Quant. Spectrosc. Radiative Transfer, 234, 115

Furmann B., Stefańska D., Wilman S., Chomski M., Suski M., 2019b, J. Quant. Spectrosc. Radiative Transfer, 235, 70

Furmann B., Klempka M., Mieloch S., Stefańska D., 2024, J. Quant. Spectrosc. Radiative Transfer, 316, 108903

Gorshkov V. N., Komarovskii V. A., 1979, Optics and Spectroscopy, 47, 350

Kramida A., Ralchenko Y., Reader J., NIST A. T., 2024, NIST Atomic Spectra Database (ver. 5.11), https://physics.nist.gov/asd

Kröger S., Wyart J. F., Luc P., 1997, Phys. Scr., 55, 579

Özdalgiç B., GüzelçİmenF., Öztürk I. K., Kröger S., Kruzins A., Tamanis M., Ferber R., Başar G., 2019a, ApJS, 240, 27

Özdalgiç B., et al., 2019b, ApJS, 240, 28

Özdalgiç B., Başar G., Kröger S., 2019c, ApJS, 244, 41

Smirnov Y. M., 2013, Optics and Spectroscopy, 114, 485

Sneden C., Lawler J. E., Cowan J. J., Ivans I. I., Den Hartog E. A., 2009, ApJS, 182, 80

Stefanska D., Furmann B., 2018, J. Quant. Spectrosc. Radiative Transfer, 206, 286

Stefanska D., Ruczkowski J., Elantkowska M., Furmann B., 2018a, J. Quant. Spectrosc. Radiative Transfer, 209, 180

Stefanska D., Furmann B., Głowacki P., 2018b, J. Quant. Spectrosc. Radiative Transfer, 213, 159

Stone N. J., 2005, Atomic Data and Nuclear Data Tables, 90, 75

Windholz L., 2016, Phys. Scr., 91, 114003

Windholz L., Guthöhrlein G. H., 2003, Physica Scripta Volume T, 105, 55

Windholz L., Başar G., Kröger S., Başar G., 2024, Spectrochimica Acta - Part B: Atomic Spectroscopy, 214, 106900

Zeiser A., Kröger S., Pooyan-Weis L., Windholz L., Guthöhrlein G., 2022, J. Quant. Spectrosc. Radiative Transfer, 290, 108294

Zengin M., Barka S. K., Öztürk İ. K., Klincare I., Kröger S., Başar G., 2024, Spectrochimica Acta - Part B: Atomic Spectroscopy, 217, 106950

İSTANBUL UNIVERSITY PRESS

Physics and Astronomy Reports
PAR 2024, 2 (2), 94–99
DOI: 10.26650/PAR.2024.00010

RESEARCH ARTICLE

Transfer Matrix Formalism for Two-Dimensional (2D) Superconducting Material

Şevval Taşdemir[1*]

[1]Kocaeli University, Faculty of Arts and Sciences, Department of Physics, 41380, Kocaeli, Türkiye

ABSTRACT

This study introduces a fundamental transfer matrix formalism for superconductors. The transfer matrix is constructed by solving Maxwell's equations under the TM (Transfer Magnetic) mode configuration and including boundary conditions at the interface of the superconductors. This matrix enables an investigation of the scattering properties of electromagnetic wave interacting with superconducting surfaces. Then, reflection coefficient (R) and transmission coefficient (T) are derived from elements of the transfer matrix. This formalism provides a basis for understanding the interaction of electromagnetic waves with the surface of superconductors for advanced studies such as coherent perfect absorption (CPA), spectral singularities, and PT symmetry. The results highlight the influence of the London penetration depth on the reflection coefficient (R), the transmission coefficient (T) and transfer matrix. Additionally, surface currents resulting from TM mode configuration and Meissner effect, are also expressed in terms of the London penetration depth. In this context, we establish a foundation for studying the potential applications of superconductors.

Keywords: Transfer matrix; Superconductors; London penetration depth; TM mode configuration

1. INTRODUCTION

Superconductors are a significant class of materials that conduct an electric current without resistance and energy loss at a certain critical temperature T_c (Tinkham 1974). In conventional conductors, electric current is carried by individual electrons, whereas in superconductors, the current is carried by pairs of electrons known as Cooper pairs. Above the critical temperature, Cooper pairing breaks down, and superconductivity disappears. Furthermore, superconductors exclude magnetic fields below the critical temperature; this phenomenon is known as the Meissner effect (Tinkham & Lobb 1989). Examining the intriguing magnetic and electrical properties and analyzing interaction with the electromagnetic waves of superconductors play a crucial role in developing innovative technologies in various fields. The London equations, presented in London (1964), describe the phenomenon of superconductivity within a classical framework.

$$\frac{d\vec{J}_s}{dt} = \frac{n_s e^2}{m}\vec{E}, \tag{1}$$

$$\nabla \times \vec{J}_s = -\frac{n_s e^2}{m}\vec{B}. \tag{2}$$

Here, $\vec{J}_s$ is the super liquid component of current density, n_s is the liquid charge density, and m is the charge mass (The London equations are explained in detail in the Supplementary Materials section). Equations (1) and (2) give relationships of current density with electric and magnetic fields, respectively. Typically, the current has two components: normal and superfluid. The normal component of current is neglected in the case of superconductivity. In this regime, the superconducting state predominates, and the electric current is carried by the supercurrent, which is composed of cooper pairs. However, during phase transitions, as mentinoned in Schmidt (2013), the normal current must be considered. The normal current corresponds to the conventional flow of charge carriers, which experiences resistance as a result of scattering mechanisms. In contrast, the supercurrent is characterized by the movement of Cooper pairs that flow without resistance.

$$\vec{J} = \vec{J}_s + \vec{J}_n. \tag{3}$$

London equations are important to understand the electromagnetic behaviour of superconductors at low temperatures. These equations combine Maxwell's equations with the hydrodynamic model of superconductors, explaining properties such as supercurrents and the Meissner effect through the electromagnetic behaviour of the superconducting state. The application of these equations often depends on the choice of the electromagnetic mode configurations, such as the TM and TE modes, which provide different insights into the interaction of electromagnetic waves with superconducting materials. The

Corresponding Author: Ş Taşdemir **E-mail:** sevval.tasdemir@kocaeli.edu.tr
Submitted: 30.10.2024 • **Revision Requested:** 25.11.2024 • **Last Revision Received:** 10.12.2024 • **Accepted:** 17.12.2024

TM mode configuration is particularly crucial for analyzing the magnetic field penetration and current distributions within the superconductor, as it directly couples to the magnetic field component perpendicular to the surface. In contrast, the TE mode configuration primarily addresses the behaviour of the electric fields and provides information on phenomena such as surface impedance and electromagnetic wave propagation.

This study focuses on the TM mode configuration because it directly engages with the magnetic field component perpendicular to the surface, facilitating an application of the London equations. Moreover, TM modes are particularly advantageous for examining the role of the London penetration depth and boundary conditions which are essential to understanding the electromagnetic response of superconductors.

The transfer matrix method is highly effective for investigating surface interactions with electromagnetic waves. As demonstrated in several studies (Sarısaman & Taş 2018, 2019b,a; Oktay et al. 2020; Sarısaman et al. 2024), this method is widely used to explore material properties such as coherent perfect absorbers (CPA), spectral singularity points, and PT-symmetric. This paper aims to establish a fundamental framework for the investigation of these properties in superconductors by using the transfer matrix method.

Firstly, Maxwell equations are solved using the London equations under the TM mode configuration and obtained boundary conditions on the surface of the superconductor slab (SC). The transfer matrix is formed by considering boundary conditions and R and T coefficients are formulated. Finally, surface currents are obtained in the direction of the electric field components as a result of electromagnetic wave interaction with the surface of SC slab under the TM mode configuration. We predict that our results will significantly contribute to the understanding of surface behaviour in superconductors.

2. SOLUTIONS OF MAXWELL EQUATIONS

Maxwell's equations play an important role in analyzing the interaction of electromagnetic waves with SC slab system. As shown in Figure 1, the solutions of Maxwell equations must be obtained for regions I, II, and III. Then, by incorporating the London penetration depth into these solutions, we can derive the boundary conditions for the surface of SC slab. We consider a linear and homogeneous SC slab with thickness L positioned in the xz-plane as shown in Figure 1. The electromagnetic wave is sent with incident angle θ to the SC slab. Here, θ denotes the angle between the incident light and the surface normal. The Maxwell's equations are expressed as,

$$\vec{\nabla}\cdot\vec{D} = \rho(z), \tag{4}$$

$$\vec{\nabla}\cdot\vec{B} = 0, \tag{5}$$

$$\vec{\nabla}\times\vec{E} = -\partial_t\vec{B}, \tag{6}$$

$$\vec{\nabla}\times\vec{H} = \vec{J}(z) + \partial_t\vec{D}. \tag{7}$$

Here, magnetic field $\vec{B}$, electric field $\vec{E}$ and current density $\vec{J}$ depend on position and time. We use the notations $c = 1/\sqrt{\mu_0\varepsilon_0}$ for speed of light in vacuum, $k = \omega/c$ for wave vector. Also notice that, $\vec{H} = \vec{B}/\mu$ and $\vec{D} = \varepsilon\vec{E}$, μ and ε are magnetic and electric permittivity, respectively. Assuming that $\mu \approx \mu_0$ due to the Meissner effect inside of superconductor slab and $\varepsilon = n^2\varepsilon_0$, where n is the refractive index. μ_0 and ε_0 are magnetic and electric permittivity in vacuum, respectively. Using the time-harmonic oscillation approximation, fields can be separated into time and position components as $\phi(\vec{r},t) = e^{-i\omega t}\phi(\vec{r})$ where ϕ parameter indicate $\vec{E},\vec{B},\vec{J},\vec{D},\vec{H}$ fields. Then, the time-independent Maxwell equations are obtained as follows,

$$\vec{\nabla}\times\vec{E} = i\omega B(\vec{r}), \tag{8}$$

$$\vec{\nabla}\times\vec{B} = \mu_0\vec{J} - ik\frac{n^2}{c}E(\vec{r}). \tag{9}$$

In the TM mode configuration, the components of $\vec{E}$ are in x and z-direction, the component of $\vec{B}$ field is only in y-direction as follows,

$$E(\vec{r}) = E_x(x,z)\vec{i} + E_z(x,z)\vec{k}, \tag{10}$$

$$B(\vec{r}) = B(x,z)\vec{j}. \tag{11}$$

$E_x(x,z)$ and $B(x,z)$ denote spatial plane waves that propagate in the x-direction.

$$B_y(x,z) = B_y(z)e^{ikx}, \tag{12}$$

$$E_x(x,z) = E_x(z)e^{ikx}, \tag{13}$$

$$E_z(x,z) = E_z(z)e^{ikx}. \tag{14}$$

Considering that the current density $\vec{J}$ is zero outside a superconductor, we take the curl of Equation (9) which is written

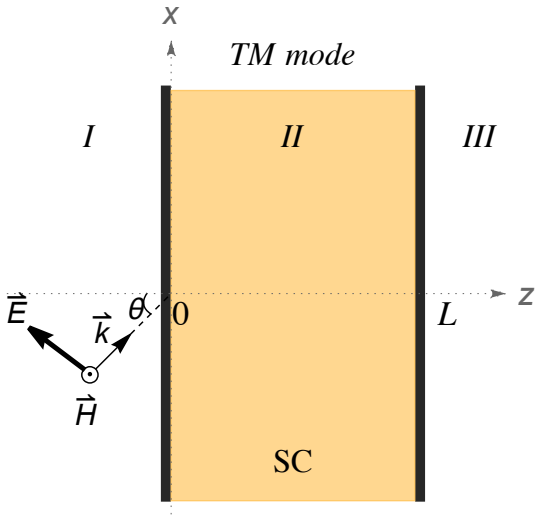

Figure 1. The figure represents an electromagnetic wave model which is sent by θ angle to the surface normal with the SC slab under the TM mode configuration. Electromagnetic wave propagate in x-direction and SC Slab which has L thickness is positioned along the z-axis.

as,

$$\vec{\nabla} \times \vec{\nabla} \times \vec{B}(\vec{r}) = -ik\frac{n^2}{c}\vec{\nabla} \times \vec{E}(r). \tag{15}$$

The components of the electric field in Equation (10) and the magnetic field the Equation (11) are placed in Equation (15). Thus, the 1-dimensional Helmholtz equation, which describes the motion of the waves due to the magnetic field, is obtained.

$$\nabla^2 B_y(z) = -k^2 n^2 B_y(z). \tag{16}$$

The Equation (16) depends on the refractive index, the wave number and the magnetic field. The solution to 1-dimensional Helmholtz equation is given by $B_y(z) = B_1 e^{iknz} + B_2 e^{-iknz}$.

2.1. Meissner Effect

Below the critical temperature T_c, the superconductors do not allow the electric and magnetic fields to exist their inside. As a result, surface currents are generated due to the exclusion of the magnetic field within the material. The electric field is zero ($\vec{E} = 0$) in SC slab system. This situation is named the Meissner effect and is expressed by the following equation:

$$\nabla \times \vec{B} = \mu_0 \vec{J}. \tag{17}$$

Taking the curl of the Equation (17) yields the wave equation for the interior of the SC slab.

$$\vec{\nabla} \times \vec{\nabla} \times \vec{B} = \mu_0(\vec{\nabla} \times \vec{J}). \tag{18}$$

The London Equation (2) is replaced in Equation (18) and it gives the 1-dimensional Helmholtz equation for region II.

$$\nabla^2 B_y(z) = \mu_0 \left(\frac{n_s e^2}{m}\right) B_y(z). \tag{19}$$

This expression $\lambda = \sqrt{m/\mu_0 n_s e^2}$ is London penetration depth that characterizes the extent the magnetic field can penetrate into a superconductor. It varies depending on the critical temperature T_c and the intrinsic properties of the material. Substituting λ into Equation (19), the Helmholtz equation becomes:

$$\nabla^2 B_y(z) - \frac{1}{\lambda^2} B_y(z) = 0. \tag{20}$$

The solution of the Equation (20) is given by $B_y(z) = A_1 e^{\frac{z}{\lambda}} + A_2 e^{-\frac{z}{\lambda}}$ and depends on London penetration depth in z-direction As a result, the wave modes both inside and outside of the SC slab are as follows:

$$B_y(z) = \begin{cases} A_1 e^{iknz} + A_2 e^{-iknz}, & z < 0, \\ B_1 e^{\frac{z}{\lambda}} + B_2 e^{-\frac{z}{\lambda}} & 0 < z < L, \\ C_1 e^{iknz} + C_2 e^{-iknz} & z > L. \end{cases} \tag{21}$$

Here, A_i, B_i, and C_i represent the amplitudes of the waves in regions I, II, and III, respectively.

2.2. Super Currents

The TM mode configuration leads to the emergency of surface currents in superconductors as a result of the Meissner effect. These currents occur as a result of the exclusion of the magnetic field inside the superconductors. The Equation (17) gives rise to the surface currents that are related to the magnetic field.

$$\partial_x B_y(x,z) = \mu_0 J_z, \tag{22}$$

$$-\partial_z B_y(x,z) = \mu_0 J_x. \tag{23}$$

The current density has two components in x and z- direction. We obtain these components by taking the partial derivatives of the Equation (12) according to x and z.

$$J_x = -\frac{1}{\mu_0} B'_y(z) e^{ikx}, \tag{24}$$

$$J_z = \frac{ik}{\mu_0} B_y(z) e^{ikx}. \tag{25}$$

J_x is real and J_z is the imaginary part of the current density that is described as,

$$\vec{J} = J_x \vec{i} + J_z \vec{k}. \tag{26}$$

$B'_y(z)$ is obtained by taking the derivative of Equation (21) as follows:

$$B'_y(z) = ikn \begin{cases} A_1 e^{iknz} - A_2 e^{-iknz} & z < 0 \\ -\frac{i}{\lambda kn} B_1 e^{\frac{z}{\lambda}} + \frac{i}{\lambda kn} B_2 e^{-\frac{z}{\lambda}} & 0 < z < L \\ C_1 e^{iknz} - C_2 e^{-iknz} & z > L. \end{cases} \tag{27}$$

The electric field and the surface currents are proportional to each other ($\vec{E} \propto \vec{J}$), and the components of $\vec{E}$ and $\vec{J}$ are in the same directions. Firstly, London Equation (1) express the electric field in terms of the current density.

$$\vec{E}(\vec{r},t) = \left(\frac{m}{n_s e^2}\right) \frac{d}{dt} \vec{J}(\vec{r},t). \tag{28}$$

The current density is given by $\vec{J}(\vec{r},t) = e^{-i\omega t}\vec{J}(\vec{r})$ and depends on time and position. By replacing the current density $\vec{J}(\vec{r},t)$ into the Equation (28), the time-independent version of the electric field $\vec{E}$ is obtained.

$$\vec{E}(\vec{r}) = \left(\frac{i\omega m}{n_s e^2}\right) \vec{J}(\vec{r}). \tag{29}$$

Taking into account the components of the current density J_x and J_z, the components of the electric fields are determined in terms of the London penetration depth λ.

$$E_x \vec{i} + E_z \vec{k} = \left(\frac{i\omega m}{n_s e^2}\right) (J_x \vec{i} + J_z \vec{k}). \tag{30}$$

E_x and E_z are imaginary and real parts of the electric field, respectively.

$$E_x = -\left(\frac{i\omega m}{n_s e^2}\right) J_x = i\lambda^2 \omega B'_y(z) e^{ikx}, \tag{31}$$

$$E_z = -\left(\frac{i\omega m}{n_s e^2}\right) J_z = \lambda^2 \omega k B_y(z) e^{ikx}. \tag{32}$$

Table 1. The components of $\vec{E}$, $\vec{D}$ and $\vec{J}$ fields inside and outside of SC slab are demonstrated in TM mode configuration in the table. $B_y(z)$ and $B'_y(z)$ are defined in Equations (21) and (27), respectively.

E	D	J
$E_x = i\lambda^2\omega B'_y(z)e^{ikx}$	$D_x = i\lambda^2\omega\varepsilon_0 n^2 B'_y(z)e^{ikx}$	$J_x = -\frac{B'_y(z)}{\mu_0}e^{ikx}$
$E_y = 0$	$D_y = 0$	$J_y = 0$
$E_z = \lambda^2\omega k B_y(z)e^{ikx}$	$D_z = \lambda^2\omega k\varepsilon_0 n^2 B_y(z)e^{ikx}$	$J_z = ik\frac{B_y(z)}{\mu_0}e^{ikx}$

Table 2. This table shows the components of the H and B filed, where $B_y(z)$ is defined in Equation (21).

B	H
$B_x = 0$	$H_x = 0$
$B_y = B_y(z)e^{ikx}$	$H_y = \frac{B_y(z)}{\mu_0}e^{ikx}$
$B_z = 0$	$H_z = 0$

Using these field components in Table 1 and Table 2, boundary conditions can be calculated. Table 3 presents these boundary conditions, which are crucial for obtaining the transfer matrix. The transfer matrix gives the relationship with each other incoming and outgoing waves interacting with the SC slab. As shown in Table 3, applying boundary conditions (1) and (3), and performing term by-term addition and subtraction, the following set of equations is obtained:

$$B_1 = \frac{1}{2}\left[(1+\sigma)A_1 + (1-i\sigma)A_2\right], \tag{33}$$

$$B_2 = \frac{1}{2}\left[(1-i\sigma)A_1 + (1+i\sigma A_2\right]. \tag{34}$$

Notice that, $\sigma = i\lambda kn$. Similarly, by applying the same operations of the term by-term addition and subtraction to boundary conditions (2) and (4), we obtained the new set of equations which provide B_1 and B_2 as follows:

$$B_1 = \frac{1}{2}\left[(1+i\sigma)C_1 e^{iknL} + (1-i\sigma)C_2 e^{-iknL}\right]e^{\frac{-L}{\lambda}}, \tag{35}$$

$$B_2 = \frac{1}{2}\left[(1-i\sigma)C_1 e^{iknL} + (1+i\sigma)C_2 e^{-iknL}\right]e^{\frac{L}{\lambda}}. \tag{36}$$

Equations (33) and (35) are equal to Equations (34) and (36), respectively.

$$aA_1 + bA_2 = [aC_1 e^{iknL} + bC_2 e^{-iknL}]e^{\frac{-L}{\lambda}}, \tag{37}$$

$$bA_1 + aA_2 = [bC_1 e^{iknL} + aC_2 e^{-iknL}]e^{\frac{L}{\lambda}}. \tag{38}$$

It should be noted that, $a = 1 + i\sigma$ and $b = 1 - i\sigma$. Finally, Equations (37) and (38) are added and subtract term by term:

$$C_1 = \frac{1}{a^2 - b^2}\left[(a^2 e^{\frac{L}{\lambda}} - b^2 e^{\frac{-L}{\lambda}})A_1 + ab(e^{\frac{L}{\lambda}} - e^{\frac{-L}{\lambda}})A_2\right]e^{-iknL}, \tag{39}$$

$$C_2 = \frac{1}{a^2 - b^2}\left[ab(e^{\frac{-L}{\lambda}} - e^{\frac{L}{\lambda}})A_1 + (a^2 e^{\frac{-L}{\lambda}} - b^2 e^{\frac{L}{\lambda}})A_2\right]e^{iknL}. \tag{40}$$

These equations form the elements of the transfer matrix. As

Table 3. Boundary conditions for SC slab are shown in the table. We define the quantity $\sigma = i\lambda kn$.

Boundary conditions
1) $A_1 + A_2 = B_1 + B_2$
2) $B_1 e^{\frac{L}{\lambda}} + B_2 e^{-\frac{L}{\lambda}} = C_1 e^{iknL} + C_2 e^{-iknL}$
3) $\sigma(A_1 - A_2) = B_1 - B_2$
4) $B_1 e^{\frac{L}{\lambda}} - B_2 e^{-\frac{L}{\lambda}} = \sigma(C_1 e^{iknL} - C_2 e^{-iknL})$

a result of this, the relationship between the incoming and outgoing on the SC slab in Figure 2, is determined with a transfer matrix.

$$\begin{pmatrix} C_1 \\ C_2 \end{pmatrix} = \mathbf{M}\begin{pmatrix} A_1 \\ A_2 \end{pmatrix} \tag{41}$$

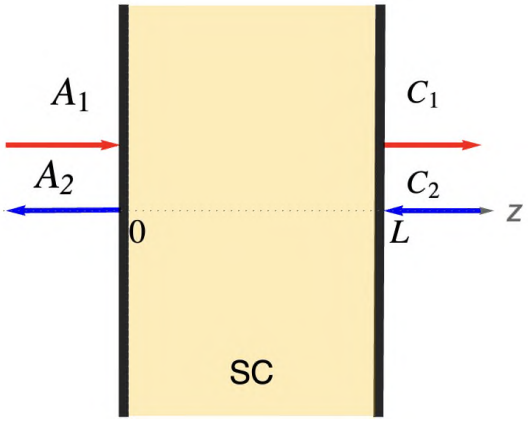

Figure 2. Figure shows the amplitudes of left and right waves in regions I and III, respectively.

3. TRANSFER MATRIX

The transfer matrix is a crucial tool used to determine the transmitted and reflected waves at the surface boundary of the materials. It plays an important role to analyses superconducting behavior on the surface of the material. Using the Equations (39) and (40), transfer matrix is constructed as follows:

$$\mathbf{M} = \begin{pmatrix} M_{11} & M_{12} \\ M_{21} & M_{22} \end{pmatrix} \tag{42}$$

The transfer matrix (42) contains all the information about the transmitted and reflected waves on the SC slab. The elements of the transfer matrix is defined as follows,

$$M_{11} = [e^{-iknL}(a^2 e^{L/\lambda} - b^2 e^{-L/\lambda})]\gamma, \tag{43}$$

$$M_{12} = ab[e^{-iknL}(e^{L/\lambda} - e^{-L/\lambda})]\gamma, \tag{44}$$

$$M_{21} = ab[e^{iknL}(e^{-L/\lambda} - e^{L/\lambda})]\gamma, \tag{45}$$

$$M_{22} = [e^{iknL}(a^2 e^{-L/\lambda} - b^2 e^{L/\lambda})]\gamma. \tag{46}$$

Here, $\gamma = \frac{1}{a^2-b^2}$ and coefficients A_1 and A_2 represent the right and left wave amplitudes in the I-region, while coefficients C_1 and C_2 represent the right and left wave amplitudes in the III-region in Figure 2. Notice that, $\det|\mathbf{M}| = 1$ and $T^l = T^r$. The left and right transmission coefficients $T^{l,r}$ and reflection $R^{l,r}$ coefficients are given by Mostafazadeh (2009).

$$T^l = T^r = T = \frac{1}{M_{22}}, \qquad R^r = \frac{M_{12}}{M_{22}}, \qquad R^l = -\frac{M_{21}}{M_{22}}. \quad (47)$$

We can define R and T coefficients for SC slab by using the Equation (47) as follows:

$$T = \frac{4i\sigma}{\chi} e^{-iknL}, \quad (48)$$

$$R^l = \frac{(1+\sigma^2)\psi}{\chi}, \qquad R^r = \frac{(1+\sigma^2)\psi}{\chi} e^{-2iknL}. \quad (49)$$

We denote that, $\psi = e^{L/\lambda} - e^{-L/\lambda}$, $\gamma = 1/4i\sigma$ and $\chi = a^2 e^{-L/\lambda} - b^2 e^{L/\lambda}$. Equation (48) is a general formalism for analysing the surface of SC slab in terms of R and T coefficients. This formalisation provides a foundation for investigating applications such as PT-symmetry, CPA, and spectral singularity for superconductors, as seen in works Sarısaman et al. (2024), Mostafazadeh (2009), and Mostafazadeh & Sarısaman (2015).

4. CONCLUSION

In this study, to understand the electromagnetic interaction with superconductors, we solved the Maxwell equations and determined these fields $\vec{E}, \vec{D}, \vec{B}$ and $\vec{H}$ both inside and outside the material. By using these fields, we derived the boundary conditions for the interface of the SC slab. In this way, we constructed a general transfer matrix from boundary conditions for superconductors in the TM mode configuration. This matrix allows for the analysis of the interactions between the superconducting surface and the electromagnetic wave. In this context, the reflection coefficient (R) and transmission coefficient (T) are formulated by London penetration depth λ. Furthermore, the obtained transfer matrix forms a crucial basis for advanced studies such as CPA, PT-symmetry and spectral singularity. On the other hand, by considering the Meissner effect, we solved Maxwell's fourth Equation (7) and observed the emergence of the surface currents related to the magnetic field. The components of the current generated on the surface (xz- plane) are perpendicular to the magnetic field. Also, the surface current $\vec{J}$ is expressed in terms of the London penetration depth λ. Consequently, this study provides a foundation for research on the interactions of superconductors with electromagnetic waves.

Peer Review: Externally peer-reviewed.
Author Contribution: Conception/Design of study - Ş.T.; Data Acquisition - Ş.T.; Data Analysis/Interpretation - Ş.T.; Drafting Manuscript - Ş.T.; Critical Revision of Manuscript - Ş.T.; Final Approval and Accountability - Ş.T.; Technical or Material Support - Ş.T.; Supervision - Ş.T.
Conflict of Interest: Author declared no conflict of interest.
Financial Disclosure: Author declared no financial support.
Acknowledgements: Thanks to Ass. Prof. Dr. Oktay Cebecioğlu and Research Assistant Ozan Çobanoğlu from Kocaeli University for their insightful discussions and technical guidance.

SUPPLEMENTARY

London Equations

To obtain the London equations, we determine the current density as seen in this study Saif (1992),

$$\vec{j}_n = \sigma \vec{E}. \quad (50)$$

Here, σ is the electrical conductivity, and $\vec{E}$ is the electrical fields. Also, the current $\vec{j}_n$ is proportional to the electric field $\vec{E}$. The force acting on the electrons is defined by the Coulomb force.

$$\vec{F} = m\vec{a}, \quad (51)$$

$$\vec{F} = e\vec{E}, \quad (52)$$

$$e\vec{E} = m\frac{\partial \vec{v}}{\partial t}. \quad (53)$$

Equation (50) is written for superconductors as follows,

$$\vec{j}_s = evn_s. \quad (54)$$

Here, n_s is the density of superconducting electrons. Taking the time derivative of Equation (54) gives first London Equation (1), as seen in Saif (1992).

$$\frac{\partial \vec{j}_s}{\partial t} = e\frac{\partial v}{\partial t} n_s = e\left(\frac{e\vec{E}}{m}\right) n_s = \frac{e^2 n_s}{m}\vec{E}. \quad (55)$$

Taking the curl of Equation (55),

$$\frac{\partial}{\partial t}(\vec{\nabla} \times \vec{j}_s) = \left(\frac{e^2 n_s}{m}\right)(\vec{\nabla} \times \vec{E}). \quad (56)$$

The curl of the electric field is as follows:

$$\vec{\nabla} \times \vec{E} = \left(\frac{m}{e^2 n_s}\right)\frac{\partial}{\partial t}(\vec{\nabla} \times \vec{j}_s). \quad (57)$$

This expression gives the relationship of super current density with electric field. Replacing third equation of Maxwell Equation (6) into Equation (57):

$$\left(\frac{m}{e^2 n_s}\right)\frac{\partial}{\partial t}(\vec{\nabla} \times \vec{j}_s) = -\frac{\partial}{\partial t}\vec{B}. \quad (58)$$

Equation (58) gives the relationship the super current with magnetic field and second London Equation (2).

$$\frac{\partial}{\partial t}\left(\vec{\nabla} \times \vec{j}_s + \left(\frac{e^2 n_s}{m}\right)\vec{B}\right) = 0. \quad (59)$$

$$\vec{\nabla} \times \vec{j}_s = -\left(\frac{e^2 n_s}{m}\right) \vec{B}. \tag{60}$$

LIST OF AUTHOR ORCIDS

Şevval Taşdemir https://orcid.org/0000-0002-4106-7872

REFERENCES

London F., 1964, Superfluids. No. 2. c. in Structure of Matter Series, Dover Publications, https://books.google.com.tr/books?id=fK4PAQAAMAAJ

Mostafazadeh A., 2009, Phys. Rev. A, 80, 032711

Mostafazadeh A., Sarısaman M., 2015, Phys. Rev. A, 91, 043804

Oktay G., Sarısaman M., Tas M., 2020, Scientific Reports, 10, 3127

Saif A. G., 1992, Physica Status Solidi B Basic Research, 171, 199

Sarısaman M., Taş M., 2018, Journal of the Optical Society of America B Optical Physics, 35, 2423

Sarısaman M., Taş M., 2019a, Journal of Applied Physics, 126, 163102

Sarısaman M., Taş M., 2019b, Annals of Physics, 401, 139

Sarısaman M., Taşdemir S., Rostamzadeh S., 2024, Journal of Physics Condensed Matter, 36, 405603

Schmidt V. V., 2013, The Physics of Superconductors: Introduction to Fundamentals and Applications. Springer Science & Business Media

Tinkham M., 1974, Reviews of Modern Physics, 46, 587

Tinkham M., Lobb C., 1989, in , Vol. 42, Solid state physics. Elsevier, pp 91–134